VILNIUS UNIVERSITY

CENTER FOR PHYSICAL SCIENCES AND TECHNOLOGY

VYTAUTAS ABRAMAVIČIUS

Theory of Energy and Charge Transport in Organic Molecular Systems

Doctoral dissertation

Physical sciences, Physics (02P)

Vilnius, 2017

Dissertation was prepared at Vilnius university in 2013–2017.

Scientific supervisor –

prof. Darius Abramavičius (Vilnius university, Physical sciences, Physics – 02P).

VILNIAUS UNIVERSITETAS

FIZINIŲ IR TECHNOLOGIJOS MOKSLŲ CENTRAS

VYTAUTAS ABRAMAVIČIUS

Energijos ir krūvio pernašos teorija organinėse molekulinėse sistemose

Daktaro disertacija

Fiziniai mokslai, Fizika (02P)

Vilnius, 2017

Disertacija rengta 2013–2017 metais Vilniaus universitete.

Mokslinis vadovas –

prof. Darius Abramavičius (Vilniaus universitetas, fiziniai mokslai, fizika – 02P).

Contents

List of abbreviations

SSE stochastic Schrödinger equation

HSSE hierarchical stochastic Schrödinger equation

HEOM Hierarchical Equations of Motion

FGR Fermi Golden Rule

FMO Fenna–Matthews–Olson

OSC organic solar cell

BHJ bulk heterojunction

CT charge transfer

MC Monte-Carlo

Introduction

Transport phenomena occupies a special and very important place in physics. In a huge variety of physical processes we can observe either energy or matter being transferred from one place to another, e. g., wave phenomena (energy transport) or an ink droplet mixing with water (particle transport). Essentially, transport of any kind is synonymous to motion. Thus describing energy or particle transfer in different systems we, first of all, need to investigate the collective motion of many, possibly interacting, constituents of the system. Although many interesting and significant transport phenomena (diffusion in gases and liquids, electromagnetic energy transfer) can be studied by applying models and methods from classical physics, a wide range of processes that emerged with the advent of quantum mechanics (charge motion in semiconductors and superconductors, photoelectric effect in metals) requires non-classical treatment. Quantum mechanical description is also unavoidable when studying energy and charge transfer effects in organic molecular compounds.

Molecular aggregates are usually modeled as open quantum systems containing relatively few observable degrees of freedom interacting with their environment. The environment can consist of any degrees of freedom which are not included in the open system under consideration: phonons, external electromagnetic fields or other molecular electronic or vibrational levels. Due to a large variety of relevant quantum states and coupling strengths between them, the excitation or charge dynamics in molecular compounds reveals a rich collection of phenomena occurring on different timescales. Theoretical description of the evolution on different timescales usually requires separate methods which are better suited in the particular parameter range. Thus, the most difficult systems for modeling are those which exhibit dynamics falling in between two distinct timescales or regimes. Most theoretical calculations either brake down in such intermediate cases or the computational effort required to handle them is too large, hence unpractical. Thus, the development of theoretical approaches must constantly be in progress in order to utilize the latest achievements in computational technologies and be able to catch up with new experimental techniques and results revealing the extensive variety of phenomena in organic molecular systems.

Studying energy and charge transport is especially important in one of the most

intriguing areas of research – the science behind the photosynthesis in plants and bacteria. The process of photosynthesis used by these organisms to convert the energy of the sunlight to chemical energy suggests that artificial photosynthesis technology, if mastered, could revolutionize the way mankind satisfies its energy needs [1–4]. One big advantage of artificial photosynthesis is the ability to convert the solar energy to chemical energy by splitting water molecules and obtaining hydrogen which could be more easily stored than electric energy. The by-products of this process are not harmful for the environment. However, current technologies have not yet reached high enough energy conversion efficiency [5–7] and the organic materials used in such devices degrade over time due to exposure to oxygen [2, 3]. Thus, it is necessary to investigate natural photosynthetic systems to reveal how the evolution tailored them to become effective sources of energy for many organisms on Earth.

Another approach to harness the power of the Sun is to use the photoelectric effect in inorganic semiconductors. Current silicon-based solar cells are already widely used and commercially viable [8–11] but they are still quite expensive and lack flexibility which restricts mounting possibilities. An alternative to inorganic solar cells are elements based on organic molecular materials. Such devices only recently achieved energy conversion efficiency still lower but allowing them to compete with silicon-based solar cells. However organic molecular technology is much cheaper in production and it offers the advantage of being so flexible that layers of sunlight absorbing material can be integrated in an endless variety of household products and locations. In order to improve the efficiency and the service time of organic solar cells it is necessary to thoroughly understand the fundamental processes of energy and charge transport occurring in these devices, from light absorption to charge extraction. A particularly important step in light to electrical energy conversion is the dissociation mechanism of the initial molecular excitation and subsequent charge separation.

The main goal of this thesis is to develop a consistent approach for describing open quantum system dynamics in a wide range of timescales and system parameters and apply this method to study energy transport in photosynthetic Fenna–Matthews–Olson complex and the characteristics of charge separation process in organic solar cells. This goal was achieved in the following steps:

- Deriving the general, formally exact stochastic Schrödinger equation and its equivalent form – the hierarchical stochastic Schrödinger equation for calculations with linear system–bath coupling of arbitrary strength.

- Obtaining the weak system–bath approximation form of the stochastic Schrödin-

ger equation and comparing its performance against other open quantum systems propagation methods for a simple toy system.

- Applying the stochastic Schrödinger equation to calculate the energy transfer dynamics in the photosynthetic Fenna–Matthews–Olson system.

- Using the stochastic Schrödinger equation to simulate the initial charge separation dynamics in the bulk heterojunction organic solar cells on the several picosecond timescale and comparing the results with experimental data to reveal the stages of coherent to incoherent transition of charge motion.

Relevance and novelty of the results

The ability to accurately describe the dynamics of an open quantum system is usually the cornerstone on which the machinery for the investigation of the specific transport problem is based. Many methods for characterizing the evolution of an open quantum system are approximating in some way either the dynamics of the heat bath (classical mechanics description, Markovian fluctuations), the system–bath interaction (Born approximation), the model of coupling between the constituents of the system or combining all of these simplifications. This is done in order to efficiently investigate the dynamics of the system in some particular parameter range. Due to such limitations it is generally difficult to tackle problems which lie on the boundaries between two or more different regimes of the processes observed in the given system, e. g., the transition between coherent and incoherent motion of the electron in the organic solar cell. In this thesis we suggest the weak-coupling stochastic Schrödinger equation (Section 2.2) obtained from its full formally exact form (Chapter 2) which is derived using the path integral formalism. The weak-coupling stochastic Schrödinger equation is shown to describe very well the dynamics of the spin–boson model system linearly coupled to the harmonic oscillator bath in a wide range of parameter values and temperatures in comparison to the Redfield theory and taking the Hierarchical Equations of Motion result as the benchmark. However, the full form of the stochastic Schrödinger equation is very difficult to solve directly, hence we derive a hierarchical system of coupled stochastic equations, the hierarchical stochastic Schrödinger equations, in Section 2.3 which is completely equivalent to the formally exact original equation but more easily calculated numerically to an arbitrary accuracy. Compared to the density operator propagating methods, the stochastic nature of the stochastic Schrödinger equation has a remarkable advantage when studying transport processes, namely a stochastic realization of this equation can be interpreted as describing the fluctuating trajectory of a single particle/excitation in a real-life experiment. Thus, we suggest a

straightforward method to obtain distributions of a relevant observables by aggregating the random values that we get from performing a quantum measurement on the wave vector of a single stochastic Schrödinger equation realization (Section 3.2). We use this procedure to calculate energy excitation transfer time distributions in the photosynthetic Fenna–Matthews–Olson complex and investigate the obtained excitation transfer pathways (Chapter (3)).

The versatility of the stochastic Schrödinger equation is elucidated investigating charge separation in organic solar cells. Photon absorption in these devices primarily creates neutral molecular excitations, while their conversion to electron–hole pairs occurs at the heterojunction between electron donating (polymers or small molecules) and electron accepting (fullerenes or their derivatives) materials. Electron–hole pairs split into free charge carriers on a femtosecond time scale and the efficiency of this process is approaching 100% despite the strong mutual Coulomb attraction between charges. There is an ongoing debate about the exact mechanism responsible for such efficient charge separation at organic heterojunctions. Although several often conflicting models have been proposed, neither of them can address consistently the dynamics of charge pairs from the shortest timescales to the longer ones. Several explanations were suggested for the initial dissociation stage, e. g., charge carrier delocalization over several polymer segments and/or fullerene molecules, hot interfacial charge-transfer (CT) states with delocalized wave functions, or, alternatively, with electron and/or hole wavefunctions localized on molecules situated at large distances from the interface. Recently, a partially coherent model, assuming electron delocalization over the entire aggregated fullerene domain, and a hybrid model of a 1D polymer/fullerene lattice with semi-classical dynamics at short time scales and Redfield relaxation theory at long time scales, have been proposed. Thus, we can see that charge separation on an ultrafast timescale is usually considered to be predominantly coherent. However, carrier delocalization and coherent propagation, their extent and temporal evolution have only been qualitatively postulated. The characterization of the gradual transition of the initial dynamics to later evolution of charge separation, successfully described by incoherent hopping, was still absent. Thus, we used the stochastic Schrödinger equation to fill this gap and model the electron–hole pair separation consistently across sever the overlapping timescales from femtoseconds to several picoseconds. These results are presented in Section 4.2. Here we reveal the importance of the electron delocalization and the role of coherence in efficient charge pair separation. We also explore the interplay between charge localization and delocalization at different times and illustrate the motion of the electron wavepacket graphically.

In Section 4.3 further investigation of charge separation is conduced on the timescale of tens to hundreds of picoseconds. On this timescale the charge separation

process is still ongoing and one of the main questions is whether diffusion or drift is responsible for pulling the electron-hole pair further apart. After several picoseconds from the start of the initial exciton dissociation quantum effects die out and the dynamics of the electron's motion in the organic solar cell can be adequately described by the incoherent charge hopping implemented using computationally cheap Monte-Carlo simulations. Comparing theoretical calculations with experimental results we find that the drift becomes noticeable only in the sub-nanosecond timescale and stronger external electric fields whereas the diffusion is the main cause of charge separation starting from tens of picoseconds. The motion of electron-hole pairs is strongly dependent on the morphology of the organic materials inside the organic solar cell. In Section 4.3 we investigate how the charge mobility and electron–hole pair separation length depends on the size of donor and acceptor domains and show that larger domains facilitate longer separation distances in sub- and nanosecond timescales.

Statements of the thesis

1. The derived stochastic Schrödinger equation is a versatile tool for modeling the dynamics of open quantum systems linearly coupled to environment applicable in a wide range of parameter values. Its hierarchical form can be used to solve the formally exact stochastic Schrödinger equation to an arbitrary accuracy and approach the formally exact result.

2. Excitation transfer times distributions calculated with stochastic Schrödinger equation reveal the excitation transport pathways in the Fenna–Matthews–Olson complex which are not sensitive to high-frequency modes of the bath.

3. Charge separation in bulk heterojunction organic solar cells, as revealed by the stochastic Schrödinger equation, occurs in three stages: coherent motion phase of the exciton dissociation, the transient phase of partially delocalized charges and the incoherent hopping phase of separated charges. The initial coherent spreading of the electron wavefunction greatly facilitates further electron–hole pair separation.

4. Diffusion is the main driving force behind the charge separation at long times. Cell morphology greatly influences the charge pair motion as smaller donor and acceptor material domains limit the range of charge separation distance.

List of publications

P1. V. Abramavicius and D. Abramavicius, *Nonclassical energy transfer in photo-*

synthetic FMO complex, EPJ Web of Conferences **41**, 08014 (2013).

P2. D. A. Vithanage, A. Devižis, V. Abramavičius, Y. Infahsaeng, D. Abramavičius, R. C. I. MacKenzie, P. E. Keivanidis, A. Yartsev, D. Hertel, J. Nelson, V. Sundström and V. Gulbinas, *Visualizing charge separation in bulk heterojunction organic solar cells*, Nat. Comm. **4**, 2334 (2013).

P3. V. Abramavicius and D. Abramavicius, *Excitation transfer pathways in excitonic aggregates revealed by the stochastic Schrödinger equation*, J. Chem. Phys. **140**, 065103 (2014).

P4. V. Abramavičius, D. A. Vithanage, A. Devižis, Y. Infahsaeng, A. Bruno, S. Foster, P. E. Keivanidis, D. Abramavičius, J. Nelson, A. Yartsev, V. Sundström and V. Gulbinas, *Carrier motion in as-spun and annealed P3HT:PCBM blends revealed by ultrafast optical electric field probing and Monte Carlo simulations*, Phys. Chem. Chem. Phys. **16**, 2686-2692 (2014).

P5. V. Abramavicius, V. Pranculis, A. Melianas, O. Inganäs, V. Gulbinas and D. Abramavicius, *Role of coherence and delocalization in photo-induced electron transfer at organic interfaces*, Sci. Rep. **6**, 32914 (2016).

P6. V. Abramavicius and D. Abramavicius, *Exact form of the stochastic Schrödinger equation for an arbitrary spectral density*, Phys. Rev. E (2017), under review.

The author of this thesis performed the major part of the theoretical calculations in all publications and was substantially involved in writing of the text. For publications P1, P3, P5 and P6 the author derived all theoretical expressions, performed the simulations and wrote the major part of the article. For publications P2 and P4 the author performed the bulk of simulations and wrote the corresponding theory part of the article. All the credit for the experimental measurements goes to other co-authors of these publications.

Publications with results not used in this thesis:

1. R. Augulis, M. Franckevičius, V. Abramavičius, D. Abramavičius, S. M. Zakeeruddin, M. Grätzel, V. Gulbinas, *Multistep Photoluminescence Decay Reveals Dissociation of Geminate Charge Pairs in Organolead Trihalide Perovskites*, Adv. Energy Mat., 1700405 (2017).

List of conferences

1. V. Abramavicius, D. Abramavicius, *Modeling of excitation transfer dynamics in the photosynthetic FMO complex using the stochastic Schrodinger equation*, 11th Nordic Femtochemistry conference (Vilnius, Lithuania, 2014).

2. V. Abramavicius, D. Abramavicius, V. Gulbinas, *Modeling of charge separation dynamics in polymer–fullerene blends using the stochastic Schrödinger equation*, Quantum Effects in Biological Systems conference (Florence, Italy, 2015).

3. V. Abramavicius, D. Abramavicius, V. Gulbinas, *Charge separation modeling at the organic donor–acceptor material interface using the stochastic Schrödinger equation*, Lietuvos nacionalinė fizikos konferencija (Vilnius, Lithuania, 2015).

4. V. Abramavicius, D. Abramavicius, V. Gulbinas, *Modeling charge separation dynamics at the interface of donor and acceptor materials using the stochastic Schrödinger equation*, Functional Materials and Nanotechnologies conference (Vilnius, Lithuania, 2015).

Chapter 1

Dynamics of open quantum systems

1.1 Reduced density matrix formalism

In quantum mechanics the wavefunction is the most general way of describing the state of any system consisting of an arbitrary number of particles and/or fields. The whole structure of such system is encoded in its Hamiltonian and the time evolution is governed by the Schrödinger equation. However, in many cases, when the number of constituents of the system is very large, the majority of them do not present any interest on their own. For instance, we generally do not care about the motion of each water molecule surrounding some protein aggregate and we do not track the exact configuration of the quantized electromagnetic field interacting with an atom. In both cases the state of only a small part (the aggregate or the atom) of the huge system is relevant to us, and the rest of it acts as an influence-inducing background. In more formal terms, it means that the global system Hamiltonian $\widehat{H}$ can be partitioned into the relevant system part $\widehat{H}_{\mathrm{S}}$, the environmental (bath) part $\widehat{H}_{\mathrm{B}}$ and the term characterizing the interaction between the two subsets – $\widehat{H}_{\mathrm{I}}$. Thus, the Schrödinger equation describing the evolution of the whole composite system reads

$$\frac{\mathrm{d}}{\mathrm{d}t}\big|\Psi\left(t\right)\big\rangle = -\mathrm{i}\left(\widehat{H}_{\mathrm{S}} + \widehat{H}_{\mathrm{B}} + \widehat{H}_{\mathrm{I}}\right)\big|\Psi\left(t\right)\big\rangle. \tag{1.1}$$

Here the wave vector $\big|\Psi\left(t\right)\big\rangle$ encodes the evolution of every degree of freedom in the global system. We also set $\hbar = 1$ in this equation and use this convention throughout this thesis. Thus, to extract the relevant information about the small system we could solve Eq. (1.1) and then simply pick out the corresponding components of the global wave vector $\big|\Psi\left(t\right)\big\rangle$. However, in most practical cases the relevant system is microscopic (has few degrees of freedom) and it interacts with some kind of macroscopic environment having a nearly infinite number of degrees of freedom, hence, solving the full Schrödinger equation is quite literally impossible.

At first glance a way out of this situation would seem only to calculate the evolution of the relevant system wave vector $\left|\psi\left(t\right)\right\rangle$ with some kind of an effective Schrödinger equation

$$\frac{\mathrm{d}}{\mathrm{d}t}\left|\psi\left(t\right)\right\rangle = -\mathrm{i}\left(\widehat{H}_{\mathrm{S}} + \widehat{F}_{\mathrm{E}}\left(t\right)\right)\left|\psi\left(t\right)\right\rangle \tag{1.2}$$

which incorporates the effect of the environment via operator $\widehat{F}_{\mathrm{E}}\left(t\right)$. For this kind of equation to be feasible in the first place, we have to be sure that a wave vector $\left|\psi\left(t\right)\right\rangle$ describing the small system alone can be found. This requirement implies that the global system wave vector $\left|\Psi\left(t\right)\right\rangle = \left|\psi\left(t\right)\right\rangle \otimes \left|\chi\left(t\right)\right\rangle$ should be a tensor product of the small system wave vector $\left|\psi\left(t\right)\right\rangle$ and the wave vector $\left|\chi\left(t\right)\right\rangle$ describing the remaining part of the complex system. Furthermore, wave vectors $\left|\psi\left(t\right)\right\rangle$ and $\left|\chi\left(t\right)\right\rangle$ must be pure states at all moments in time. However, strictly speaking such situation can only be realized when the relevant system does not interact with its environment and we essentially have two separate closed systems. In this case Eq. (1.2) becomes the ordinary Schrödinger equation for the wave vector $\left|\psi\left(t\right)\right\rangle$ because the environmental term $\widehat{F}_{\mathrm{E}}\left(t\right)$ is zero. The reason why the tensor product structure cannot be maintained in the interacting system is that during the time evolution all degrees of freedom in the global system become entangled and it becomes impossible to assign separate wave vectors (pure states [12]) to different sub-units of the big system [12, 13]. Thus, we see that an expression of the form (1.2) cannot be a formally exact evolution equation for the state of a sub-unit of a big system.

We have seen that the wave vector as in Eq. (1.2) is not adequate for describing the evolution of the open quantum system and a different approach is needed. Quantum states can also be characterized by density operators [12, 13]. For a system in some pure state $\left|\Psi\left(t\right)\right\rangle$ the density operator $\widehat{W}\left(t\right) = \left|\Psi\left(t\right)\right\rangle\left\langle\Psi\left(t\right)\right|$ is given by the outer product of the ket and bra. The density operator can describe more general mixed states [12] $\widehat{W}\left(t\right) = \sum\limits_{n} p_n \left|\Psi_n\left(t\right)\right\rangle\left\langle\Psi_n\left(t\right)\right|$ as well, which can be interpreted as a sum of pure states $\left|\Psi_n\left(t\right)\right\rangle\left\langle\Psi_n\left(t\right)\right|$ weighted by coefficients p_n. The evolution of the density operator of a system with the Hamiltonian $\widehat{H}$ is governed by the Liouville equation:

$$\frac{\mathrm{d}}{\mathrm{d}t}\widehat{W}\left(t\right) = -\mathrm{i}\left[\widehat{H}, \widehat{W}\left(t\right)\right]. \tag{1.3}$$

Eq. (1.3) is completely analogous to the Schrödinger equation (1.1) and the density operator $\widehat{W}\left(t\right)$ contains the same amount of information as the wave vector $\left|\Psi\left(t\right)\right\rangle$. However, the density operator has an advantage of allowing to get rid of the unnecessary DOF by averaging over them using the partial trace operation [12, 13]. Thus, we can define the reduced density operator

$$\widehat{\rho}_{\mathrm{red}}(t) = \mathrm{Tr}_{\mathrm{B}}\left[\widehat{W}(t)\right] \tag{1.4}$$

describing only the dynamics of the relevant part (reduced system) of the global system by tracing out the bath DOF. The partial trace operation on a pure entangled state results in a mixed state described by $\widehat{\rho}_{\mathrm{red}}(t)$ which can be interpreted as a statistical ensemble (not unique) of all possible pure states available to the small system if it were isolated from the environment. Consequently, we see again that a single pure state is not sufficient for the description of the reduced system dynamics because there is no such thing as a "reduced wave vector".

In the next section we will present several methods to deal with the explicit calculation of the reduced density operator $\widehat{\rho}_{\mathrm{red}}(t)$ and explore their strengths and weaknesses.

1.2 Methods for propagating the reduced density matrix

One of the most popular theoretical models used for describing open quantum systems in general and organic molecular compounds in particular is the spin-boson model linearly coupled to the bath of harmonic oscillators. Popular methods working well in the weak system–bath coupling regime are Redfield [12, 14, 15], Förster [12,15,16] and modified Redfield [12,15,17] approaches. The original Redfield method is obtained from the general second-order quantum master equation [12, 18] for the system+bath density operator by applying the Born approximation and tracing out the bath degrees of freedom, thus obtaining the equation of motion for the reduced density operator. This equation is simplified further invoking the Markov approximation leading to the time-local Redfield equation which is second-order in system–bath coupling strength. Redfield equation is very useful when modeling the dynamics of the photosynthetic aggregates consisting of strongly coupled electronic levels, weakly interacting with their environment [19–21]. However, frequently the system–bath interaction is much stronger than the inter-molecular couplings in the aggregate. The evolution in such case can be adequately described by the Förster theory. When the chromophores in the photosynthetic aggregate are coupled weakly the dynamics of the system is incoherent – excitations are almost fully localized and move by hopping between different chromophores. Such evolution is theoretically described by Fermi golden rule-like rate equation where the so called Förster rates are obtained from molecular absorption and emission lineshapes. It has to be noted that the Förster theory does not take into account any coherences between different chromophores and the rates are calculated solely based on the probabilities of excitation transfer from one molecule to another. Both Redfield and Förster methods can be

obtained as limits of the modified Redfield approach [12]. This method modifies the original Redfield equation by treating the diagonal fluctuations non-perturbatively and including correlations between diagonal and off-diagonal fluctuations.

When the inter-chromophore and system–bath couplings are large the perturbative methods often are not accurate enough or even completely fail to describe the evolution of the system [22]. For such cases there exist a number of approaches treating the dynamics of the open quantum system exactly within the chosen model. Such system can be exactly solved using methods based on the path integral representation of the underlying problem. It can be shown that the reduced density matrix of an arbitrary system linearly coupled to harmonic bath can be expressed via the Feynman-Vernon influence functional [23] which in the general case is very difficult to solve. All the exact methods for propagating the reduced density matrix in some way try to calculate this functional. The Hierarchical Equations of Motion (HEOM) method incorporates the effect of the influence functional through a set of coupled differential equations for auxiliary density matrices [24, 25]. HEOM can work only with an exponential correlation function of the bath fluctuations and it is generally computationally expensive, especially at low temperatures and strong couplings with the bath. A more direct approach for estimating the influence functional is taken by QUasi-Adiabatic propagator Path-Integral (QUAPI) which discretizes the paths of the system's evolution and sums over them [26]. One drawback of such scheme is that it converges easily only when the correlation function of the bath fluctuations is not very broad which implies small memory time and nearly Markovian bath dynamics. In other cases the numerical effort increases significantly and often becomes unpractical. However, compared to HEOM the QUAPI method in principle allows a bath with an arbitrary spectral density.

A completely different, although also exact, method for calculating the dynamics of the open system is the time-dependent Density Matrix Renormalization Group (tDMRG) approach [27–29]. It is based on the mapping of the system linearly interacting with the bath to a chain of sites with nearest neighbor interactions only. Then such system is solved with traditional DMRG methods by reducing the dimensionality of the system's Hilbert space [27]. The advantages of tDMRG include the ability to perform calculations of the system's evolution with arbitrary spectral densities and coupling strengths. However, this method in is quite demanding numerically in strong coupling cases due to increased number of required basis states [30].

Since the number of degrees of freedom scale exponentially with the number of bath modes, approximate accurate approaches are always welcome to treat relatively large systems. The time-dependent variational approach (TDVP) postulates the functional form of the wavefunction of the whole system+bath complex [31, 32]. As the complete wavefunction is unknown, the guessed form of the wavefunction reduces

the Hilbert space of solutions to a particular section, while the wavefunction in this section is optimized with respect to the Hamiltonian. Hence, the approximation enters not in the equations of motion, but into the boundary conditions of the solution. One popular choice is using the Davydov D_2 Ansatz and use the variational principle to find the wavefunction with the least deviation from the exact one. Here the bath modes are treated explicitly, thus no reduced density matrix formalism is needed. The TDVP method includes polaronic effects in molecular aggregates, hence it goes beyond the perturbative results, where the bath degrees of freedom essentially do not evolve. However, the accuracy cannot be easily controlled: it solely depends on the functional form of the Ansatz.

Chapter 2

Stochastic Schrödinger equation for energy and charge transport

In this chapter we rigorously derive and thoroughly explore the features of the main calculational tool used in this thesis – the stochastic Schrödinger equation. In Section 2.1 we derive the most general form of the stochastic Schrödinger equation using the path integral and coherent states formalisms. For a brief introduction to both of them see Appendices B and A respectively. In Section 2.2 we present the weak system–bath coupling approximation of the general stochastic Schrödinger equation making it applicable to a wide range of transport problems. After that, in Section 2.3 we further develop the general stochastic Schrödinger equation and derive its hierarchical form thus obtaining the hierarchical stochastic Schrödinger equation. Further, in Section 2.4 we describe the practical aspects of performing calculations with the stochastic Schrödinger equation and compare its performance against other theoretical methods.

2.1 Derivation of the stochastic Schrödinger equation [P1, P3, P6]

Let us study a bosonic system coupled to a heat bath consisting of an infinite number of harmonic oscillators. The Hamiltonian of such complex system is composed of the small system part $\widehat{H}_{\mathrm{S}}$, the heat bath part $\widehat{H}_{\mathrm{B}}$ and the interaction part $\widehat{H}_{\mathrm{I}}$. Explicitly it reads

$$\widehat{H} = \sum_{n} \epsilon_n \widehat{a}_n^\dagger \widehat{a}_n + \sum_{n \neq m} J_{nm} \widehat{a}_n^\dagger \widehat{a}_m + \sum_{k} \omega_k \widehat{b}_k^\dagger \widehat{b}_k + \kappa \sum_{nk} \widehat{a}_n^\dagger \widehat{a}_n \left(g_{nk} \widehat{b}_k^\dagger + g_{nk}^* \widehat{b}_k \right). \tag{2.1}$$

Here $\widehat{a}_n^\dagger(\widehat{a}_n)$ is the creation (annihilation) operator of the n-th boson of the system, ϵ_n is its excitation energy and J_{nm} is the coupling between n-th and m-th bosons. Similarly, $\widehat{b}_k^\dagger(\widehat{b}_k)$ is the creation (annihilation) operator of the k-th harmonic oscillator mode of the bath, ω_k is its frequency and $g_{nk}$is the coupling between the n-th boson and k-th oscillator mode. κ parametrizes the overall interaction strength between the system and the environment.

The big system+environment can be described using the wave vector $\big|\Psi(t)\big\rangle$ or equivalently the density operator $\widehat{W}(t) = \big|\Psi(t)\big\rangle\big\langle\Psi(t)\big|$. The evolution of the operator $\widehat{W}(t)$ is given by the Liouville equation (1.3). Setting the initial time $t_0 = 0$ its solution can be written as $\widehat{W}(t) = \widehat{U}(t)\,\widehat{W}_0\widehat{U}^\dagger(t)$ using the evolution operator $\widehat{U}(t) = \exp\left[-\mathrm{i}\widehat{H}t\right]$. Here $\widehat{W}_0$ is the initial density operator of the whole complex system. We are usually interested only in the evolution of the small bosonic system, thus, we limit ourselves with the study of the reduced density operator $\widehat{\rho}_{\mathrm{red}}(t)$ defined in Eq. (1.4).

Our immediate goal now is to obtain the coherent state path integral expression of the Eq. (1.4). Firstly, we write Eq. (1.4) in the coherent state basis (see Appendix A for details):

$$\begin{aligned}\widehat{\rho}_{\mathrm{red}}(t) &= \int_{-\infty}^{\infty}\mathrm{d}^2\boldsymbol{\alpha}_f\int_{-\infty}^{\infty}\mathrm{d}^2\boldsymbol{\alpha}'_f\mathrm{e}^{-\boldsymbol{\alpha}_f^*\boldsymbol{\alpha}_f-\boldsymbol{\alpha}_f^{*\prime}\boldsymbol{\alpha}'_f}\big\langle\boldsymbol{\alpha}_f\big|\widehat{\rho}_{\mathrm{red}}(t)\,\big|\boldsymbol{\alpha}'_f\big\rangle\big|\boldsymbol{\alpha}_f\big\rangle\big\langle\boldsymbol{\alpha}'_f\big| \\ &= \int_{-\infty}^{\infty}\mathrm{d}^2\boldsymbol{\alpha}_f\int_{-\infty}^{\infty}\mathrm{d}^2\boldsymbol{\alpha}'_f\int_{-\infty}^{\infty}\mathrm{d}^2\boldsymbol{\beta}_f\mathrm{e}^{-\boldsymbol{\alpha}_f^*\boldsymbol{\alpha}_f-\boldsymbol{\alpha}_f^{*\prime}\boldsymbol{\alpha}'_f-\boldsymbol{\beta}_f^*\boldsymbol{\beta}_f} \\ &\times\big\langle\boldsymbol{\alpha}_f\big|\big\langle\boldsymbol{\beta}_f\big|\widehat{U}(t)\,\widehat{W}_0\widehat{U}^\dagger(t)\,\big|\boldsymbol{\beta}_f\big\rangle\big|\boldsymbol{\alpha}'_f\big\rangle\big|\boldsymbol{\alpha}_f\big\rangle\big\langle\boldsymbol{\alpha}'_f\big|. \end{aligned} \tag{2.2}$$

Here we denote coherent states acting in the system's Hilbert space by $\boldsymbol{\alpha}_f$ and $\boldsymbol{\alpha}'_f$ while for bath coherent states we use $\boldsymbol{\beta}_f$. The corresponding integration measures have the form $\mathrm{d}^2x \equiv \frac{\mathrm{dRe}[x]\mathrm{dIm}[x]}{\pi}$. Note that we use the abbreviations $\big|\boldsymbol{\alpha}_f\big\rangle = \prod_n\big|\alpha_{f,n}\big\rangle$, $\boldsymbol{\alpha}_f^*\boldsymbol{\alpha}_f = \sum_n\alpha_{f,n}^*\alpha_{f,n}$ and $\big|\boldsymbol{\beta}_f\big\rangle = \prod_k\big|\beta_{f,k}\big\rangle$, $\boldsymbol{\beta}_f^*\boldsymbol{\beta}_f = \sum_k\beta_{f,k}^*\beta_{f,k}$. For the initial density operator $\widehat{W}_0$ we assume the uncorrelated tensor product structure $\widehat{W}_0 = \widehat{\rho}_0\otimes\widehat{\rho}_T$ where $\widehat{\rho}_0$ and $\widehat{\rho}_T$ describe the initial states of the system and the bath respectively. For simplicity we prepare the system in some initial coherent state $\widehat{\rho}_0 = \big|\boldsymbol{\alpha}_i\big\rangle\big\langle\boldsymbol{\alpha}'_i\big|$ - more general states can always be constructed with the superposition of coherent states. We also assume that the bath initially is in the thermal equilibrium, thus, in the coherent states basis $\widehat{\rho}_T$ reads [33]

$$\widehat{\rho}_T = \prod_k \int_{-\infty}^{\infty} \mathrm{d}^2\beta_{i,k} \frac{1}{\overline{n}_k} \mathrm{e}^{-\beta_{i,k}^* \beta_{i,k} \left(\overline{n}_k^{-1}+1\right)} \left|\beta_{i,k}\right\rangle \left\langle\beta_{i,k}\right|, \tag{2.3}$$

where $\overline{n}_k = \left(\mathrm{e}^{\beta_T \omega_k} - 1\right)^{-1}$ is the Bose-Einstein function and $\beta_T = \frac{1}{k_\mathrm{B} T}$.

Plugging Eq. (2.3) into Eq. (2.2) we obtain:

$$\begin{aligned}\rho_\mathrm{red}\left(\boldsymbol{\alpha}_f^*, \boldsymbol{\alpha}_f'; t\right) = \int_{-\infty}^{\infty} \mathrm{d}^2\boldsymbol{\beta}_f \int_{-\infty}^{\infty} \mathrm{d}^2\boldsymbol{\beta}_i \prod_k \frac{1}{\overline{n}_k} \mathrm{e}^{-\beta_{f,k}^* \beta_{f,k} - \beta_{i,k}^* \beta_{i,k} \left(\overline{n}_k^{-1}+1\right)} \\ \times K\left(\boldsymbol{\alpha}_f^* \boldsymbol{\beta}_f^*, \boldsymbol{\alpha}_i \boldsymbol{\beta}_i; t\right) K^*\left(\boldsymbol{\alpha}_i^{*\prime} \boldsymbol{\beta}_i^*, \boldsymbol{\alpha}_f' \boldsymbol{\beta}_f; t\right).\end{aligned} \tag{2.4}$$

Here by $\rho_\mathrm{red}\left(\boldsymbol{\alpha}_f^*, \boldsymbol{\alpha}_f'; t\right) = \left\langle \boldsymbol{\alpha}_f \right| \widehat{\rho}_\mathrm{red}\left(t\right) \left| \boldsymbol{\alpha}_f' \right\rangle$ we denoted the $\boldsymbol{\alpha}_f^* \boldsymbol{\alpha}_f'$ matrix element of the reduced density operator. We also introduce the forward propagator $K\left(\boldsymbol{\alpha}_f^* \boldsymbol{\beta}_f^*, \boldsymbol{\alpha}_i \boldsymbol{\beta}_i; t\right) = \left\langle \boldsymbol{\alpha}_f \boldsymbol{\beta}_f \right| \widehat{U}\left(t\right) \left| \boldsymbol{\beta}_i \boldsymbol{\alpha}_i \right\rangle$ evolving the system from the initial to the final state and the backward propagator $K^*\left(\boldsymbol{\alpha}_i^{*\prime} \boldsymbol{\beta}_i^*, \boldsymbol{\alpha}_f' \boldsymbol{\beta}_f; t\right) = \left\langle \boldsymbol{\alpha}_i' \boldsymbol{\beta}_i \right| \widehat{U}^\dagger\left(t\right) \left| \boldsymbol{\beta}_f \boldsymbol{\alpha}_f' \right\rangle$ returning the system back to the initial state. In order to obtain the coherent state path integral representation of the reduced density matrix $\rho_\mathrm{red}\left(\boldsymbol{\alpha}_f^*, \boldsymbol{\alpha}_f'; t\right)$ we apply the usual time discretization procedure to the propagators $K\left(\boldsymbol{\alpha}_f^* \boldsymbol{\beta}_f^*, \boldsymbol{\alpha}_i \boldsymbol{\beta}_i; t\right)$ and $K^*\left(\boldsymbol{\alpha}_i^{*\prime} \boldsymbol{\beta}_i^*, \boldsymbol{\alpha}_f' \boldsymbol{\beta}_f; t\right)$ (see Appendix B). For the forward propagator we have

$$\begin{aligned}K\left(\boldsymbol{\alpha}_f^* \boldsymbol{\beta}_f^*, \boldsymbol{\alpha}_i \boldsymbol{\beta}_i; t\right) = \int_{\boldsymbol{\alpha}_i, \boldsymbol{\beta}_i}^{\boldsymbol{\alpha}_f^*, \boldsymbol{\beta}_f^*} \mathcal{D}\left[\boldsymbol{\alpha}^*\left(\tau\right), \boldsymbol{\alpha}\left(\tau\right)\right] \mathcal{D}\left[\boldsymbol{\beta}^*\left(\tau\right), \boldsymbol{\beta}\left(\tau\right)\right] \\ \times \mathrm{e}^{\mathrm{i}S_\mathrm{S}(\boldsymbol{\alpha}^*, \boldsymbol{\alpha}) + \mathrm{i}S_\mathrm{B}(\boldsymbol{\beta}^*, \boldsymbol{\beta}) + \mathrm{i}S_\mathrm{I}(\boldsymbol{\alpha}^*, \boldsymbol{\alpha}, \boldsymbol{\beta}^*, \boldsymbol{\beta})},\end{aligned} \tag{2.5}$$

where $\boldsymbol{\alpha}\left(0\right) = \boldsymbol{\alpha}_i$, $\boldsymbol{\beta}\left(0\right) = \boldsymbol{\beta}_i$ and $\boldsymbol{\alpha}^*\left(t\right) = \boldsymbol{\alpha}_f^*$, $\boldsymbol{\beta}^*\left(t\right) = \boldsymbol{\beta}_f^*$, $\mathcal{D}\left[\cdot\right]$ denotes the measure of the functional integral and components of the action $S\left(\boldsymbol{\alpha}^*, \boldsymbol{\alpha}, \boldsymbol{\beta}^*, \boldsymbol{\beta}\right) = S_\mathrm{S}\left(\boldsymbol{\alpha}^*, \boldsymbol{\alpha}\right) + S_\mathrm{B}\left(\boldsymbol{\beta}^*, \boldsymbol{\beta}\right) + S_\mathrm{I}\left(\boldsymbol{\alpha}^*, \boldsymbol{\alpha}, \boldsymbol{\beta}^*, \boldsymbol{\beta}\right)$ correspond to the appropriate parts of the Hamiltonian (2.1).

2.1.1 Schrödinger picture stochastic equation

Actions defined in Eq. (2.5) explicitly read:

$$S_{\mathrm{S}}\left(\boldsymbol{\alpha}^{*},\boldsymbol{\alpha}\right)=-\mathrm{i}\sum_{n}\alpha_{n}^{*}\left(t\right)\alpha_{n}\left(t\right)+\int_{0}^{t}\mathrm{d}\tau\sum_{n}\left(\mathrm{i}\alpha_{n}^{*}\left(\tau\right)\frac{\partial}{\partial\tau}\alpha_{n}\left(\tau\right)\right.$$
$$\left.-\epsilon_{n}\alpha_{n}^{*}\left(\tau\right)\alpha_{n}\left(\tau\right)-\sum_{m}J_{nm}\alpha_{n}^{*}\left(\tau\right)\alpha_{m}\left(\tau\right)\right), \tag{2.6a}$$
$$S_{\mathrm{B}}\left(\boldsymbol{\beta}^{*},\boldsymbol{\beta}\right)=-\mathrm{i}\sum_{k}\beta_{k}^{*}\left(t\right)\beta_{k}\left(t\right)$$
$$+\int_{0}^{t}\mathrm{d}\tau\sum_{k}\left(\mathrm{i}\beta_{k}^{*}\left(\tau\right)\frac{\partial}{\partial\tau}\beta_{k}\left(\tau\right)-\omega_{k}\beta_{k}^{*}\left(\tau\right)\beta_{k}\left(\tau\right)\right), \tag{2.6b}$$
$$S_{\mathrm{I}}\left(\boldsymbol{\alpha}^{*},\boldsymbol{\alpha},\boldsymbol{\beta}^{*},\boldsymbol{\beta}\right)=-\kappa\int_{0}^{t}\mathrm{d}\tau\sum_{nk}\alpha_{n}^{*}\left(\tau\right)\alpha_{n}\left(\tau\right)\left(g_{nk}\beta_{k}^{*}\left(\tau\right)+g_{nk}^{*}\beta_{k}\left(\tau\right)\right). \tag{2.6c}$$

The expressions for the backward propagator $K^{*}\left(\boldsymbol{\alpha}_{i}^{*\prime}\boldsymbol{\beta}_{i}^{*},\boldsymbol{\alpha}_{f}^{\prime}\boldsymbol{\beta}_{f};t\right)$ are similar to the ones in Eqs. (2.6a) - (2.6c) only complex conjugate and the path integral variables $\boldsymbol{\alpha}^{*\prime}\left(\tau\right),\boldsymbol{\alpha}^{\prime}\left(\tau\right),\boldsymbol{\beta}^{*\prime}\left(\tau\right),\boldsymbol{\beta}^{\prime}\left(\tau\right)$ are primed. In this case the following boundary conditions are imposed: $\boldsymbol{\alpha}^{*\prime}\left(t\right)=\boldsymbol{\alpha}_{i}^{*\prime}$, $\boldsymbol{\beta}^{*\prime}\left(t\right)=\boldsymbol{\beta}_{i}^{*}$ and $\boldsymbol{\alpha}^{\prime}\left(0\right)=\boldsymbol{\alpha}_{f}^{\prime}$, $\boldsymbol{\beta}^{\prime}\left(0\right)=\boldsymbol{\beta}_{f}$. Inserting everything back into Eq. (2.4) we obtain:

$$\rho_{\mathrm{red}}\left(\boldsymbol{\alpha}_{f}^{*},\boldsymbol{\alpha}_{f}^{\prime};t\right)=\int_{-\infty}^{\infty}\mathrm{d}^{2}\boldsymbol{\beta}_{f}\int_{-\infty}^{\infty}\mathrm{d}^{2}\boldsymbol{\beta}_{i}\prod_{k}\frac{1}{\overline{n}_{k}}\mathrm{e}^{-\beta_{f,k}^{*}\beta_{f,k}-\beta_{i,k}^{*}\beta_{i,k}\left(\overline{n}_{k}^{-1}+1\right)}$$
$$\times\int\mathcal{D}\left[\boldsymbol{\alpha}^{*}\left(\tau\right),\boldsymbol{\alpha}\left(\tau\right)\right]\mathcal{D}\left[\boldsymbol{\beta}^{*}\left(\tau\right),\boldsymbol{\beta}\left(\tau\right)\right]\mathrm{e}^{\mathrm{i}S\left(\boldsymbol{\alpha}^{*},\boldsymbol{\alpha},\boldsymbol{\beta}^{*},\boldsymbol{\beta}\right)}$$
$$\times\int\mathcal{D}\left[\boldsymbol{\alpha}^{*\prime}\left(\tau\right)\boldsymbol{\alpha}^{\prime}\left(\tau\right)\right]\mathcal{D}\left[\boldsymbol{\beta}^{*\prime}\left(\tau\right)\boldsymbol{\beta}^{\prime}\left(\tau\right)\right]\mathrm{e}^{-\mathrm{i}S^{*}\left(\boldsymbol{\alpha}^{*\prime},\boldsymbol{\alpha}^{\prime},\boldsymbol{\beta}^{*\prime},\boldsymbol{\beta}^{\prime}\right)}. \tag{2.7}$$

Further simplification of Eq. (2.7) can be achieved when we notice that the bath degrees of freedom can be integrated-out analytically. Exact calculation in this case is possible due to the Gaussian structure of the action [34]. Functional integrals of this kind can be integrated using the stationary phase method. First we obtain the equations of motion for the bath variables on the forward and backward time branches $\beta_{k}\left(\tau\right)$ and $\beta_{k}^{*\prime}\left(\tau\right)$ by calculating the functional derivatives of the action in Eq. (2.7) and its conjugate with respect to $\beta_{k}^{*}\left(\tau\right)$ and $\beta_{k}^{\prime}\left(\tau\right)$ then equating the

resulting expressions to 0. Thus, we get the equations for extremal paths of the action:

$$\mathrm{i}\frac{\partial}{\partial\tau}\beta_k(\tau) - \omega_k\beta_k(\tau) - \kappa\sum_n g_{nk}\alpha_n^*(\tau)\,\alpha_n(\tau) = 0, \tag{2.8a}$$

$$-\mathrm{i}\frac{\partial}{\partial\tau}\beta_k^{*\prime}(\tau) - \omega_k\beta_k^{*\prime}(\tau) - \kappa\sum_n g_{nk}^*\alpha_n^{*\prime}(\tau)\,\alpha_n'(\tau) = 0. \tag{2.8b}$$

Equations of motion for the variables $\beta_k^*(\tau)$ and $\beta_k'(\tau)$ can be obtained performing complex conjugation of Eqs. (2.8a) and (2.8b) respectively. Solutions to the linear differential equations (2.8a) and (2.8b) for forward and backward propagation variables are easily obtained and with the appropriate boundary conditions the extremal paths read:

$$\overset{\sim}{\beta}_k(\tau) = \beta_{i,k}\mathrm{e}^{-\mathrm{i}\omega_k\tau} - \mathrm{i}\kappa\sum_n g_{nk}\int_0^\tau \mathrm{d}\tau'\mathrm{e}^{-\mathrm{i}\omega_k(\tau-\tau')}\alpha_n^*(\tau')\,\alpha_n(\tau'), \tag{2.9a}$$

$$\overset{\sim}{\beta}_k^*(\tau) = \beta_{f,k}^*\mathrm{e}^{\mathrm{i}\omega_k(\tau-t)} - \mathrm{i}\kappa\sum_n g_{nk}^*\int_\tau^t \mathrm{d}\tau'\mathrm{e}^{\mathrm{i}\omega_k(\tau-\tau')}\alpha_n^*(\tau')\,\alpha_n(\tau'), \tag{2.9b}$$

$$\overset{\sim}{\beta}_k'(\tau) = \beta_{f,k}\mathrm{e}^{\mathrm{i}\omega_k(t-\tau)} + \mathrm{i}\kappa\sum_n g_{nk}\int_\tau^t \mathrm{d}\tau'\mathrm{e}^{-\mathrm{i}\omega_k(\tau-\tau')}\alpha_n^{*\prime}(\tau')\,\alpha_n'(\tau'), \tag{2.9c}$$

$$\overset{\sim}{\beta}_k^{*\prime}(\tau) = \beta_{i,k}^*\mathrm{e}^{\mathrm{i}\omega_k\tau} + \mathrm{i}\kappa\sum_n g_{nk}^*\int_0^\tau \mathrm{d}\tau'\mathrm{e}^{\mathrm{i}\omega_k(\tau-\tau')}\alpha_n^{*\prime}(\tau')\,\alpha_n'(\tau'). \tag{2.9d}$$

Using these extremal path solutions we can express the bath trajectories as

$$\boldsymbol{\beta}^*(\tau) = \overset{\sim}{\boldsymbol{\beta}}^*(\tau) + \boldsymbol{y}^*(\tau), \tag{2.10a}$$

$$\boldsymbol{\beta}(\tau) = \overset{\sim}{\boldsymbol{\beta}}(\tau) + \boldsymbol{y}(\tau). \tag{2.10b}$$

Here $\boldsymbol{y}^*(\tau)$ and $\boldsymbol{y}(\tau)$ are the deviations from the stationary path which are zero at the endpoints of the trajectory. Inserting Eqs. (2.10a) and (2.10b) into the expression (2.7) for the reduced density matrix, we can therefore factorize the path integral over the bath trajectories into integrals over the endpoints and the deviations

$$\rho_{\mathrm{red}}\left(\boldsymbol{\alpha}_f^*,\boldsymbol{\alpha}_f';t\right)=\int\mathcal{D}\left[\boldsymbol{\alpha}^*\left(\tau\right),\boldsymbol{\alpha}\left(\tau\right)\right]\mathcal{D}\left[\boldsymbol{\alpha}^{*\prime}\left(\tau\right),\boldsymbol{\alpha}'\left(\tau\right)\right]\mathrm{e}^{\mathrm{i}\left[S_S(\boldsymbol{\alpha}^*,\boldsymbol{\alpha})-S_S^*\left(\boldsymbol{\alpha}^{*\prime},\boldsymbol{\alpha}'\right)\right]}$$
$$\times\mathcal{I}\left(\boldsymbol{\alpha}^*,\boldsymbol{\alpha},\boldsymbol{\alpha}^{*\prime},\boldsymbol{\alpha}'\right)\int\mathcal{D}\left[\boldsymbol{y}^*\left(\tau\right),\boldsymbol{y}\left(\tau\right)\right]\mathcal{D}\left[\boldsymbol{y}^{*\prime}\left(\tau\right),\boldsymbol{y}'\left(\tau\right)\right]$$
$$\times\mathrm{e}^{\mathrm{i}\left[S_{\mathrm{dev}}(\boldsymbol{y}^*,\boldsymbol{y})-S_{\mathrm{dev}}^*\left(\boldsymbol{y}^{*\prime},\boldsymbol{y}'\right)\right]},\tag{2.11}$$

where $\mathcal{I}\left(\boldsymbol{\alpha}^*,\boldsymbol{\alpha},\boldsymbol{\alpha}^{*\prime},\boldsymbol{\alpha}'\right)=\mathrm{d}^2\boldsymbol{\beta}_f\mathrm{d}^2\boldsymbol{\beta}_i\mathcal{F}\left(\boldsymbol{\alpha}^*,\boldsymbol{\alpha},\boldsymbol{\alpha}^{*\prime},\boldsymbol{\alpha}',\boldsymbol{\beta}_f^*,\boldsymbol{\beta}_f,\boldsymbol{\beta}_i^*,\boldsymbol{\beta}_i\right)$ is the influence functional [23] which incorporates all effects of the bath and $S_{\mathrm{dev}}\left(\boldsymbol{y}^*,\boldsymbol{y}\right)$ is the path deviation action given by

$$S_{\mathrm{dev}}\left(\boldsymbol{y}^*,\boldsymbol{y}\right)=\sum_k\int_0^t\mathrm{d}\tau y_k^*\left(\mathrm{i}\frac{\partial}{\partial\tau}-\omega_k\right)y_k.\tag{2.12}$$

Path integral with action (2.12) can be integrated out exactly because it is essentially an infinite-dimensional Gaussian integral. Integration can be carried out easily in the discrete representation and its result is unity [34]. The influence functional $\mathcal{I}\left(\boldsymbol{\alpha}^*,\boldsymbol{\alpha},\boldsymbol{\alpha}^{*\prime},\boldsymbol{\alpha}'\right)$ can also be calculated exactly:

$$\mathcal{F}\left(\boldsymbol{\alpha}^*,\boldsymbol{\alpha},\boldsymbol{\alpha}^{*\prime},\boldsymbol{\alpha}',\boldsymbol{\beta}_f^*,\boldsymbol{\beta}_f,\boldsymbol{\beta}_i^*,\boldsymbol{\beta}_i\right)$$
$$=\prod_k\frac{1}{\overline{n}_k}\mathrm{e}^{-\beta_{f,k}^*\beta_{f,k}-\beta_{i,k}^*\beta_{i,k}\left(\overline{n}_k^{-1}+1\right)}$$
$$\times\mathrm{e}^{\beta_{f,k}^*\left(\beta_{i,k}\mathrm{e}^{-\mathrm{i}\omega_k t}-\mathrm{i}\kappa\sum\limits_n g_{nk}\int\limits_0^t\mathrm{d}\tau\mathrm{e}^{-\mathrm{i}\omega_k(t-\tau)}\alpha_n^*(\tau)\alpha_n(\tau)\right)}$$
$$\times\mathrm{e}^{\beta_{f,k}\left(\beta_{i,k}^*\mathrm{e}^{\mathrm{i}\omega_k t}+\mathrm{i}\kappa\sum\limits_n g_{nk}^*\int\limits_0^t\mathrm{d}\tau\mathrm{e}^{\mathrm{i}\omega_k(t-\tau)}\alpha_n^{*\prime}(\tau)\alpha_n'(\tau)\right)}$$
$$\times\mathrm{e}^{-\mathrm{i}\kappa\beta_{i,k}\sum\limits_n g_{nk}^*\int\limits_0^t\mathrm{d}\tau\mathrm{e}^{-\mathrm{i}\omega_k\tau}\alpha_n^*(\tau)\alpha_n(\tau)+\mathrm{i}\kappa\beta_{i,k}^*\sum\limits_n g_{nk}\int\limits_0^t\mathrm{d}\tau\mathrm{e}^{\mathrm{i}\omega_k\tau}\alpha_n^{*\prime}(\tau)\alpha_n'(\tau)}$$
$$\times\mathrm{e}^{-\kappa^2\sum\limits_{nm}g_{nk}^*g_{mk}\int\limits_0^t\mathrm{d}\tau\int\limits_0^\tau\mathrm{d}\tau'\mathrm{e}^{-\mathrm{i}\omega_k(\tau-\tau')}\alpha_n^*(\tau)\alpha_n(\tau)\alpha_n^*\left(\tau'\right)\alpha_n\left(\tau'\right)}$$
$$\times\mathrm{e}^{-\kappa^2\sum\limits_{nm}g_{nk}^*g_{mk}\int\limits_0^t\mathrm{d}\tau\int\limits_0^\tau\mathrm{d}\tau'\mathrm{e}^{\mathrm{i}\omega_k(\tau-\tau')}\alpha_n^{*\prime}(\tau)\alpha_n'(\tau)\alpha_n^{*\prime}\left(\tau'\right)\alpha_n'\left(\tau'\right)},\tag{2.13}$$

since the integrand $\mathcal{F}\left(\boldsymbol{\alpha}^*,\boldsymbol{\alpha},\boldsymbol{\alpha}^{*\prime},\boldsymbol{\alpha}',\boldsymbol{\beta}_f^*,\boldsymbol{\beta}_f,\boldsymbol{\beta}_i^*,\boldsymbol{\beta}_i\right)$ has Gaussian structure in bath variables. Thus, we easily obtain the influence functional depending only on system's degrees of freedom:

$$\begin{aligned}\mathcal{I}\left(\boldsymbol{\alpha}^*,\boldsymbol{\alpha},\boldsymbol{\alpha}^{*\prime},\boldsymbol{\alpha}^{\prime}\right) &= \mathrm{e}^{\kappa^2\sum\limits_{nm}\int\limits_0^t \mathrm{d}\tau\int\limits_0^t \mathrm{d}\tau^{\prime}\left[\mathcal{Z}_{nm}\left(\tau-\tau^{\prime}\right)+\mathcal{W}_{nm}\left(\tau-\tau^{\prime}\right)\right]\alpha_n^{*\prime}(\tau)\alpha_n^{\prime}(\tau)\alpha_m^{*}\left(\tau^{\prime}\right)\alpha_m\left(\tau^{\prime}\right)} \\ &\times \mathrm{e}^{-\kappa^2\sum\limits_{nm}\int\limits_0^t \mathrm{d}\tau\int\limits_0^\tau \mathrm{d}\tau^{\prime}\left[\mathcal{Z}_{nm}\left(\tau-\tau^{\prime}\right)+\mathcal{W}_{nm}\left(\tau-\tau^{\prime}\right)\right]\alpha_n^{*}(\tau)\alpha_n(\tau)\alpha_m^{*}\left(\tau^{\prime}\right)\alpha_m\left(\tau^{\prime}\right)} \\ &\times \mathrm{e}^{-\kappa^2\sum\limits_{nm}\int\limits_0^t \mathrm{d}\tau\int\limits_0^\tau \mathrm{d}\tau^{\prime}\left[\mathcal{Z}_{nm}\left(\tau-\tau^{\prime}\right)+\mathcal{W}_{nm}\left(\tau-\tau^{\prime}\right)\right]\alpha_n^{*\prime}(\tau)\alpha_n^{\prime}(\tau)\alpha_m^{*\prime}\left(\tau^{\prime}\right)\alpha_m^{\prime}\left(\tau^{\prime}\right)}.\end{aligned} \tag{2.14}$$

Here we introduced functions $\mathcal{Z}_{nm}\left(\tau-\tau^{\prime}\right)=\sum\limits_k g_{nk}^* g_{mk}\mathrm{e}^{-\mathrm{i}\omega_k\left(\tau-\tau^{\prime}\right)}\left(\overline{n}_k+1\right)$ and $\mathcal{W}_{nm}\left(\tau-\tau^{\prime}\right)=\sum\limits_k g_{nk}^* g_{mk}\mathrm{e}^{\mathrm{i}\omega_k\left(\tau-\tau^{\prime}\right)}\overline{n}_k$.

The influence functional (2.14) is not very convenient for further manipulations because forward and backward path variables of the system are coupled. In order to decouple them we need to use the Hubbard–Stratonovich transformation [35, 36] for the variables $\alpha_n^*\left(\tau\right)\alpha_n\left(\tau\right)$ and $\alpha_n^{*\prime}\left(\tau\right)\alpha_n^{\prime}\left(\tau\right)$. In practice this means that one introduces an additional Gaussian integral with appropriate sources over some auxiliary variable which gives the original coupled expression as a result. Applying this principle to the first exponent on the right-hand side of Eq. (2.14) we get

$$\begin{aligned}&\mathrm{e}^{\kappa^2\sum\limits_{nm}\int\limits_0^t \mathrm{d}\tau\int\limits_0^t \mathrm{d}\tau^{\prime}\mathcal{Z}_{nm}\left(\tau-\tau^{\prime}\right)\alpha_n^{*\prime}(\tau)\alpha_n^{\prime}(\tau)\alpha_m^{*}\left(\tau^{\prime}\right)\alpha_m\left(\tau^{\prime}\right)} \\ &\qquad = \int\limits_{-\infty}^{\infty}\mathrm{d}^2\boldsymbol{x}_Z\mathrm{e}^{-\boldsymbol{x}_Z^*\boldsymbol{x}_Z}\mathrm{e}^{\int\limits_0^t \mathrm{d}\tau\left(-\mathrm{i}\kappa\sum\limits_n z_n(\tau)\alpha_n^*(\tau)\alpha_n(\tau)+\mathrm{i}\kappa\sum\limits_n z_n^*(\tau)\alpha_n^{*\prime}(\tau)\alpha_n^{\prime}(\tau)\right)}\end{aligned} \tag{2.15a}$$

$$\begin{aligned}&\mathrm{e}^{\kappa^2\sum\limits_{nm}\int\limits_0^t \mathrm{d}\tau\int\limits_0^t \mathrm{d}\tau^{\prime}\mathcal{W}_{nm}\left(\tau-\tau^{\prime}\right)\alpha_n^{*\prime}(\tau)\alpha_n^{\prime}(\tau)\alpha_m^{*}\left(\tau^{\prime}\right)\alpha_m\left(\tau^{\prime}\right)} \\ &\qquad = \int\limits_{-\infty}^{\infty}\mathrm{d}^2\boldsymbol{x}_W\mathrm{e}^{-\boldsymbol{x}_W^*\boldsymbol{x}_W}\mathrm{e}^{\int\limits_0^t \mathrm{d}\tau\left(-\mathrm{i}\kappa\sum\limits_n w_n(\tau)\alpha_n^*(\tau)\alpha_n(\tau)+\mathrm{i}\kappa\sum\limits_n w_n^*(\tau)\alpha_n^{*\prime}(\tau)\alpha_n^{\prime}(\tau)\right)}\end{aligned} \tag{2.15b}$$

with notations $z_n^{(\mathrm{S})}\left(\tau\right)=\sum\limits_k\sqrt{\overline{n}_k+1}g_{nk}\mathrm{e}^{\mathrm{i}\omega_k\tau}x_{Z,k}^*$, $w_n^{(\mathrm{S})}\left(\tau\right)=\sum\limits_k\sqrt{\overline{n}_k}g_{nk}\mathrm{e}^{\mathrm{i}\omega_k\tau}x_{W,k}^*$ and $z_n^{(\mathrm{S})*}\left(\tau\right)$,$w_n^{(\mathrm{S})*}\left(\tau\right)$ as their complex conjugates. Here the superscript (S) is a reminder that these functions were derived in Schrödinger picture.

Now we can insert Eqs. (2.15a) and (2.15b) back into Eq. (2.14) and obtain the influence functional $\mathcal{I}\left(\boldsymbol{\alpha}^*,\boldsymbol{\alpha},\boldsymbol{\alpha}^{*\prime},\boldsymbol{\alpha}^{\prime}\right)=\mathcal{I}_{\mathrm{F}}\left(\boldsymbol{\alpha}^*,\boldsymbol{\alpha}\right)\mathcal{I}_{\mathrm{B}}\left(\boldsymbol{\alpha}^{*\prime},\boldsymbol{\alpha}^{\prime}\right)$ as a product of two functions acting on the forward and the backward time paths. Using this form

of the influence functional we can express the reduced density matrix in Eq. (2.11) as

$$\begin{aligned}\rho_{\mathrm{red}}&\left(\boldsymbol{\alpha}_f^*,\boldsymbol{\alpha}_f';t\right)\\&=\int_{-\infty}^{\infty}\mathrm{d}^2\boldsymbol{x}_Z\int_{-\infty}^{\infty}\mathrm{d}^2\boldsymbol{x}_W\mathrm{e}^{-\boldsymbol{x}_Z^*\boldsymbol{x}_Z-\boldsymbol{x}_W^*\boldsymbol{x}_W}\int\mathcal{D}\left[\boldsymbol{\alpha}^*\left(\tau\right),\boldsymbol{\alpha}\left(\tau\right)\right]\mathcal{D}\left[\boldsymbol{\alpha}^{*\prime}\left(\tau\right),\boldsymbol{\alpha}'\left(\tau\right)\right]\\&\times\psi_{\mathrm{F}}^{(\mathrm{S})}\left(\boldsymbol{\alpha}^*,\boldsymbol{\alpha},\boldsymbol{x}_Z^*,\boldsymbol{x}_W^*;t\right)\psi_{\mathrm{B}}^{(\mathrm{S})*}\left(\boldsymbol{\alpha}^{*\prime},\boldsymbol{\alpha}',\boldsymbol{x}_Z,\boldsymbol{x}_W;t\right),\end{aligned}\tag{2.16}$$

where $\psi_{\mathrm{F}}^{(\mathrm{S})}\left(\boldsymbol{\alpha}^*,\boldsymbol{\alpha},\boldsymbol{x}_Z^*,\boldsymbol{x}_W^*;t\right)$ and $\psi_{\mathrm{B}}^{(\mathrm{S})*}\left(\boldsymbol{\alpha}^{*\prime},\boldsymbol{\alpha}',\boldsymbol{x}_Z,\boldsymbol{x}_W;t\right)$ again (cf. Eq. (2.4)) can be interpreted as propagators of the system in the forward and backward time direction respectively. The forward propagator explicitly reads

$$\begin{aligned}\psi_{\mathrm{F}}^{(\mathrm{S})}\left(\boldsymbol{\alpha}^*,\boldsymbol{\alpha},\boldsymbol{x}_Z^*,\boldsymbol{x}_W^*;t\right)&=\mathrm{e}^{\mathrm{i}S_{\mathrm{S}}(\boldsymbol{\alpha}^*,\boldsymbol{\alpha})}\mathrm{e}^{-\mathrm{i}\kappa\sum\limits_n\int\limits_0^t\mathrm{d}\tau c_n(\tau)\alpha_n^*(\tau)\alpha_n(\tau)}\\&\times\mathrm{e}^{-\kappa^2\sum\limits_{nm}\int\limits_0^t\mathrm{d}\tau\int\limits_0^\tau\mathrm{d}\tau'\mathcal{C}_{nm}\left(\tau-\tau'\right)\alpha_n^*(\tau)\alpha_n(\tau)\alpha_m^*\left(\tau'\right)\alpha_m\left(\tau'\right)}.\end{aligned}\tag{2.17}$$

Here we denoted $c_n^{(\mathrm{S})}\left(\tau\right)=z_n^{(\mathrm{S})}\left(\tau\right)+w_n^{(\mathrm{S})}\left(\tau\right)$ and $\mathcal{C}_{nm}\left(\tau-\tau'\right)=\mathcal{Z}_{nm}\left(\tau-\tau'\right)+\mathcal{W}_{nm}\left(\tau-\tau'\right)$. The backward propagator can be obtained by complex conjugation of Eq. (2.17) and substitution $\boldsymbol{\alpha}^*,\boldsymbol{\alpha}\rightarrow\boldsymbol{\alpha}^{*\prime},\boldsymbol{\alpha}'$.

The last thing we have to do is to obtain the evolution equation for the forward propagator (2.17). Differentiating Eq. (2.17) we obtain

$$\begin{aligned}\frac{\mathrm{d}}{\mathrm{d}t}&\psi_{\mathrm{F}}^{(\mathrm{S})}\left(\boldsymbol{\alpha}^*,\boldsymbol{\alpha},\boldsymbol{x}_Z^*,\boldsymbol{x}_W^*;t\right)\\&=\Bigg(-\mathrm{i}H_S\left(\boldsymbol{\alpha}^*\left(t\right),\boldsymbol{\alpha}\left(t-\Delta\right)\right)\\&-\mathrm{i}\kappa\sum_n c_n^{(S)}\left(\tau\right)\alpha_n^*\left(t\right)\alpha_n\left(t-\Delta\right)-\kappa^2\sum_{nm}\alpha_n^*\left(t\right)\alpha_n\left(t-\Delta\right)\\&\times\int_0^t\mathrm{d}\tau\mathcal{C}_{nm}\left(t-\tau\right)\alpha_m^*\left(\tau\right)\alpha_m\left(\tau\right)\Bigg)\psi_{\mathrm{F}}^{(\mathrm{S})}\left(\boldsymbol{\alpha}^*,\boldsymbol{\alpha},\boldsymbol{x}_Z^*,\boldsymbol{x}_W^*;t\right).\end{aligned}\tag{2.18}$$

Here the $t-\Delta$ time moment is the reminder that α_n variables come one infinitesimal time step Δ before α_n^*. We should note that direct differentiation of the system action S_{S} yields an additional term containing derivatives $\frac{\partial\alpha_n^*(t)}{\partial t}\alpha_n\left(t\right)$, however it is demonstrated in Appendix B that they vanish. Eq. (2.18) still has one undesirable

feature – the third term on the right-hand side contains a dependence on variables $\alpha_m^*(\tau)$ and $\alpha_m(\tau)$ at time moments $\tau < t$. In order to avoid such situation we notice that if we calculate the functional derivative $\frac{\delta}{\delta c_m^{(\mathrm{S})}(\tau)}$ of Eq. (2.17) with respect to the function $c_m(\tau)$ we obtain the result $-\mathrm{i}\kappa\alpha_m^*(\tau)\,\alpha_m(\tau)$. Plugging this result into Eq. (2.18) we get the expression

$$\frac{\mathrm{d}}{\mathrm{d}t}\left|\psi^{(\mathrm{S})}(\boldsymbol{x}_Z^*,\boldsymbol{x}_W^*;t)\right\rangle = -\mathrm{i}\left(\widehat{H}_{\mathrm{S}} + \kappa\sum_n c_n^{(\mathrm{S})}(t)\,\widehat{a}_n^\dagger\widehat{a}_n - \mathrm{i}\kappa^2\sum_{nm}\widehat{a}_n^\dagger\widehat{a}_n\int_0^t \mathrm{d}\tau \right.$$
$$\left.\times\mathcal{C}_{nm}(t-\tau)\,\frac{\delta}{\delta c_m^{(\mathrm{S})}(\tau)}\right)\left|\psi^{(\mathrm{S})}(\boldsymbol{x}_Z^*,\boldsymbol{x}_W^*;t)\right\rangle. \tag{2.19}$$

In this final equation we switched to the operator form of the Eq. (2.18) with substitutions $\psi_{\mathrm{F}}^{(\mathrm{S})}(\boldsymbol{\alpha}^*,\boldsymbol{\alpha},\boldsymbol{x}_Z^*,\boldsymbol{x}_W^*;t) \to \left|\psi^{(\mathrm{S})}(\boldsymbol{x}_Z^*,\boldsymbol{x}_W^*;t)\right\rangle$, $H_{\mathrm{S}}(\boldsymbol{\alpha}^*(t),\boldsymbol{\alpha}(t-\Delta)) \to \widehat{H}_{\mathrm{S}}$ and $\alpha_n^*(t)\,\alpha_n(t-\Delta) \to \widehat{a}_n^\dagger\widehat{a}_n$. Such substitution is possible due to the fact that the path integral in Eq. (2.16) is really a coherent state representation of some evolution operator of the system. Correspondence between operators and their coherent state representations is explained in detail in Ref. [37].

With Eq. (2.19) we can write the reduced density matrix equation (2.16) in operator form as

$$\widehat{\rho}_{\mathrm{red}}(t) = \int_{-\infty}^{\infty}\mathrm{d}^2\boldsymbol{x}_Z\mathrm{d}^2\boldsymbol{x}_W p(\boldsymbol{x}_Z,\boldsymbol{x}_W)\left|\psi^{(\mathrm{S})}(\boldsymbol{x}_Z^*,\boldsymbol{x}_W^*;t)\right\rangle\left\langle\psi^{(\mathrm{S})}(\boldsymbol{x}_Z,\boldsymbol{x}_W;t)\right|. \tag{2.20}$$

In this expression the reduced density operator $\widehat{\rho}_{\mathrm{red}}(t)$ can be interpreted as the average of the function $\left|\psi^{(\mathrm{S})}(\boldsymbol{x}_Z^*,\boldsymbol{x}_W^*;t)\right\rangle\left\langle\psi^{(\mathrm{S})}(\boldsymbol{x}_Z,\boldsymbol{x}_W;t)\right|$ over multi-dimensional Gaussian variables $\boldsymbol{x}_Z$ and $\boldsymbol{x}_W$ with the probability density

$$p(\boldsymbol{x}_Z,\boldsymbol{x}_W) = \prod_k \frac{1}{\pi}\mathrm{e}^{-x_{Z,k}^* x_{Z,k} - x_{W,k}^* x_{W,k}}. \tag{2.21}$$

Exactly at this point after making the stochastic interpretation of the function under the Gaussian integrals we can think of Eq. (2.19) as the stochastic Schrödinger equation (SSE). This form of the SSE was first introduced by Diosi [38, 39].

2.1.2 Interaction picture stochastic equation

Deriving the stochastic Schrödinger equation (2.19) we used the time-independent Hamiltonian (2.1). However, one can introduce the interaction representation of $\widehat{H}$ with respect to the bath

$$\widehat{H}\left(t\right)=\mathrm{e}^{\mathrm{i}\widehat{H}_{B}t}\widehat{H}\mathrm{e}^{-\mathrm{i}\widehat{H}_{B}t}=\widehat{H}_{S}+\kappa\sum_{nk}\widehat{a}_{n}^{\dagger}\widehat{a}_{n}\left(g_{nk}\mathrm{e}^{\mathrm{i}\omega_{k}t}\widehat{b}_{k}^{\dagger}+g_{nk}^{*}\mathrm{e}^{-\mathrm{i}\omega_{k}t}\widehat{b}_{k}\right). \tag{2.22}$$

With this time-dependent Hamiltonian we can write down the Liouville equation (1.3) substituting $\widehat{H}\rightarrow\widehat{H}\left(t\right)$ and $\widehat{W}\left(t\right)\rightarrow\widehat{W}^{(\mathrm{I})}\left(t\right)=\left|\Psi^{(\mathrm{I})}\left(t\right)\right\rangle\left\langle\Psi^{(\mathrm{I})}\left(t\right)\right|=\mathrm{e}^{\mathrm{i}\widehat{H}_{\mathrm{B}}t}\widehat{W}\left(t\right)\mathrm{e}^{-\mathrm{i}\widehat{H}_{\mathrm{B}}t}$. Interaction picture wave vector $\left|\Psi^{(\mathrm{I})}\left(t\right)\right\rangle$ is given by the corresponding evolution operator expressed as time-ordered exponential

$$\widehat{U}^{(\mathrm{I})}\left(t\right)=\widehat{T}_{+}\mathrm{e}^{-\mathrm{i}\int\limits_{0}^{t}\mathrm{d}\tau\widehat{H}(\tau)}. \tag{2.23}$$

We notice that the reduced density operator $\widehat{\rho}_{\mathrm{red}}\left(t\right)$ does not change if we substitute $\widehat{W}\left(t\right)\rightarrow\widehat{W}^{(\mathrm{I})}\left(t\right)$ in Eq. (1.4). Thus, we can proceed with the same derivation path as in Subsection 2.1.1 only this time use the evolution operator (2.23) instead of $\widehat{U}\left(t\right)=\exp\left[-\mathrm{i}\widehat{H}t\right]$. In this case the system action $S_{\mathrm{S}}^{(\mathrm{I})}\left(\boldsymbol{\alpha}^{*},\boldsymbol{\alpha}\right)$ of the forward propagator (2.5) is identical to $S_{\mathrm{S}}\left(\boldsymbol{\alpha}^{*},\boldsymbol{\alpha}\right)$ in the Schrödinger picture and the only differences arise in bath and interaction parts:

$$S_{\mathrm{B}}^{(\mathrm{I})}\left(\boldsymbol{\beta}^{*},\boldsymbol{\beta}\right)=-\mathrm{i}\sum_{k}\beta_{k}^{*}\left(t\right)\beta_{k}\left(t\right)+\int\limits_{0}^{t}\mathrm{d}\tau\sum_{k}\mathrm{i}\beta_{k}^{*}\left(\tau\right)\frac{\partial}{\partial\tau}\beta_{k}\left(\tau\right), \tag{2.24a}$$

$$\begin{aligned}S_{\mathrm{I}}^{(\mathrm{I})}\left(\boldsymbol{\alpha}^{*},\boldsymbol{\alpha},\boldsymbol{\beta}^{*},\boldsymbol{\beta}\right)=&-\kappa\int\limits_{0}^{t}\mathrm{d}\tau\sum_{nk}\alpha_{n}^{*}\left(\tau\right)\alpha_{n}\left(\tau\right)\\&\times\left(g_{nk}\mathrm{e}^{\mathrm{i}\omega_{k}\tau}\beta_{k}^{*}\left(\tau\right)+g_{nk}^{*}\mathrm{e}^{-\mathrm{i}\omega_{k}\tau}\beta_{k}\left(\tau\right)\right).\end{aligned} \tag{2.24b}$$

The corresponding equations of motion for the stationary paths read

$$\mathrm{i}\frac{\partial}{\partial\tau}\beta_{k}\left(\tau\right)-\kappa\sum_{n}g_{nk}\mathrm{e}^{\mathrm{i}\omega_{k}\tau}\alpha_{n}^{*}\left(\tau\right)\alpha_{n}\left(\tau\right)=0, \tag{2.25a}$$

$$-\mathrm{i}\frac{\partial}{\partial\tau}\beta_{k}^{*\prime}\left(\tau\right)-\kappa\sum_{n}g_{nk}^{*}\mathrm{e}^{-\mathrm{i}\omega_{k}\tau}\alpha_{n}^{*\prime}\left(\tau\right)\alpha_{n}^{\prime}\left(\tau\right)=0. \tag{2.25b}$$

with the complex conjugates for $\beta_{k}^{*}\left(\tau\right)$ and $\beta_{k}^{\prime}\left(\tau\right)$. The stationary path solutions

in this case have the following form:

$$\widetilde{\beta}_k(\tau) = \beta_{i,k} - \mathrm{i}\kappa \sum_n g_{nk} \int_0^\tau \mathrm{d}\tau' \mathrm{e}^{\mathrm{i}\omega_k \tau'} \alpha_n^*(\tau') \alpha_n(\tau'), \tag{2.26a}$$

$$\widetilde{\beta}_k^*(\tau) = \beta_{f,k}^* - \mathrm{i}\kappa \sum_n g_{nk}^* \int_\tau^t \mathrm{d}\tau' \mathrm{e}^{-\mathrm{i}\omega_k \tau'} \alpha_n^*(\tau') \alpha_n(\tau'), \tag{2.26b}$$

$$\widetilde{\beta}_k'(\tau) = \beta_{f,k} + \mathrm{i}\kappa \sum_n g_{nk} \int_\tau^t \mathrm{d}\tau' \mathrm{e}^{\mathrm{i}\omega_k \tau'} \alpha_n^{*\prime}(\tau') \alpha_n'(\tau'), \tag{2.26c}$$

$$\widetilde{\beta}_k^{*\prime}(\tau) = \beta_{i,k}^* + \mathrm{i}\kappa \sum_n g_{nk}^* \int_0^\tau \mathrm{d}\tau' \mathrm{e}^{-\mathrm{i}\omega_k \tau'} \alpha_n^{*\prime}(\tau') \alpha_n'(\tau'). \tag{2.26d}$$

With these solutions we easily get the $\mathcal{F}\left(\boldsymbol{\alpha}^*, \boldsymbol{\alpha}, \boldsymbol{\alpha}^{*\prime}, \boldsymbol{\alpha}', \boldsymbol{\beta}_f^*, \boldsymbol{\beta}_f, \boldsymbol{\beta}_i^*, \boldsymbol{\beta}_i\right)$ function from Eq. (2.13):

$$\begin{aligned}
&\mathcal{F}\left(\boldsymbol{\alpha}^*, \boldsymbol{\alpha}, \boldsymbol{\alpha}^{*\prime}, \boldsymbol{\alpha}', \boldsymbol{\beta}_f^*, \boldsymbol{\beta}_f, \boldsymbol{\beta}_i^*, \boldsymbol{\beta}_i\right) \\
&\quad = \prod_k \frac{1}{\overline{n}_k} \mathrm{e}^{-\beta_{f,k}^* \beta_{f,k} - \sum_k \beta_{i,k}^* \beta_{i,k} \left(\overline{n}_k^{-1} + 1\right) + \beta_{f,k}^* \beta_{i,k} + \beta_{i,k}^* \beta_{f,k}} \\
&\quad \times \mathrm{e}^{-\mathrm{i}\kappa \sum_n \int_0^t \mathrm{d}\tau \left(z_n^{(I)}(\tau) + w_n^{(I)}(\tau)\right) \alpha_n^*(\tau) \alpha_n(\tau)} \\
&\quad \times \mathrm{e}^{\mathrm{i}\kappa \sum_n \int_0^t \mathrm{d}\tau \left(z_n^{(I)*}(\tau) + w_n^{(I)*}(\tau)\right) \alpha_n^{*\prime}(\tau) \alpha_n'(\tau)} \\
&\quad \times \mathrm{e}^{-\kappa^2 \sum_{nm} \int_0^t \mathrm{d}\tau \int_0^\tau \mathrm{d}\tau' \mathcal{C}_{nm}^{(0)}(t-\tau) \alpha_n^*(\tau) \alpha_n(\tau) \alpha_n^*\left(\tau'\right) \alpha_n\left(\tau'\right)} \\
&\quad \times \mathrm{e}^{-\kappa^2 \sum_{nm} \int_0^t \mathrm{d}\tau \int_0^\tau \mathrm{d}\tau' \mathcal{C}_{nm}^{(0)*}(t-\tau) \alpha_n^{*\prime}(\tau) \alpha_n'(\tau) \alpha_n^{*\prime}\left(\tau'\right) \alpha_n'\left(\tau'\right)}.
\end{aligned} \tag{2.27}$$

In this expression we introduced the notations $\mathcal{C}_{nm}^{(0)}(t-\tau) = \sum_k g_{nk}^* g_{mk} \mathrm{e}^{-\mathrm{i}\omega_k \left(\tau - \tau'\right)}$, $z_n^{(\mathrm{I})}(\tau) = \sum_k g_{nk} \mathrm{e}^{\mathrm{i}\omega_k \tau} \beta_{f,k}^*$ and $w_n^{(\mathrm{I})}(\tau) = \sum_k g_{nk}^* \mathrm{e}^{-\mathrm{i}\omega_k \tau} \beta_{i,k}$, and their complex conjugates. We can see that the function $\mathcal{F}$ can be written as a product

$$\begin{aligned}
&\mathcal{F}\left(\boldsymbol{\alpha}^*, \boldsymbol{\alpha}, \boldsymbol{\alpha}^{*\prime}, \boldsymbol{\alpha}', \boldsymbol{\beta}_f^*, \boldsymbol{\beta}_f, \boldsymbol{\beta}_i^*, \boldsymbol{\beta}_i\right) \\
&\quad = \mathcal{G}\left(\boldsymbol{\beta}_f^*, \boldsymbol{\beta}_f, \boldsymbol{\beta}_i^*, \boldsymbol{\beta}_i\right) \mathcal{F}_{\mathrm{F}}\left(\boldsymbol{\alpha}^*, \boldsymbol{\alpha}, \boldsymbol{\beta}_f^*, \boldsymbol{\beta}_f, \boldsymbol{\beta}_i^*, \boldsymbol{\beta}_i\right) \\
&\quad \times \mathcal{F}_{\mathrm{B}}\left(\boldsymbol{\alpha}^{*\prime}, \boldsymbol{\alpha}', \boldsymbol{\beta}_f^*, \boldsymbol{\beta}_f, \boldsymbol{\beta}_i^*, \boldsymbol{\beta}_i\right),
\end{aligned} \tag{2.28}$$

where $\mathcal{F}_{\mathrm{F}}$ and $\mathcal{F}_{\mathrm{B}}$ are the parts depending on system variables on forward and backward propagation paths and $\mathcal{G}$ is the Gaussian term depending only on initial and final states of the bath. Thus, we already have the forward and backward propagation variables separated and there is no need to integrate out the bath variables and then perform the Hubbard–Stratonovich transformation as we did in Eqs. (2.15a) and (2.15b). In the present case the role of the auxiliary Hubbard–Stratonovich variables is played by $\boldsymbol{\beta}$ variables representing the initial and final states of the bath, therefore, we readily obtain the expression for the reduced density matrix analogical to Eq. (2.16):

$$\begin{aligned}\rho_{\mathrm{red}}\left(\boldsymbol{\alpha}_f^*,\boldsymbol{\alpha}_f';t\right)=&\int\limits_{-\infty}^{\infty}\mathrm{d}^2\boldsymbol{\beta}_f\int\limits_{-\infty}^{\infty}\mathrm{d}^2\boldsymbol{\beta}_i\prod_k\frac{1}{\overline{n}_k}\mathrm{e}^{-\beta_{f,k}^*\beta_{f,k}-\beta_{i,k}^*\beta_{i,k}\left(\overline{n}_k^{-1}+1\right)+\beta_{f,k}^*\beta_{i,k}+\beta_{i,k}^*\beta_{f,k}}\\&\times\int\mathcal{D}\left[\boldsymbol{\alpha}^*\left(\tau\right),\boldsymbol{\alpha}\left(\tau\right)\right]\mathcal{D}\left[\boldsymbol{\alpha}^{*\prime}\left(\tau\right),\boldsymbol{\alpha}'\left(\tau\right)\right]\\&\times\psi_{\mathrm{F}}^{(\mathrm{I})}\left(\boldsymbol{\alpha}^*,\boldsymbol{\alpha},\boldsymbol{\beta}_f^*,\boldsymbol{\beta}_i;t\right)\psi_{\mathrm{B}}^{(\mathrm{I})*}\left(\boldsymbol{\alpha}^{*\prime},\boldsymbol{\alpha}',\boldsymbol{\beta}_i^*,\boldsymbol{\beta}_f;t\right),\end{aligned}\tag{2.29}$$

with the forward propagator having the form

$$\begin{aligned}\psi_{\mathrm{F}}^{(\mathrm{I})}\left(\boldsymbol{\alpha}^*,\boldsymbol{\alpha},\boldsymbol{\beta}_f^*,\boldsymbol{\beta}_i;t\right)=&\,\mathrm{e}^{\mathrm{i}S_{\mathrm{S}}(\boldsymbol{\alpha}^*,\boldsymbol{\alpha})}\mathrm{e}^{-\mathrm{i}\kappa\sum\limits_n\int\limits_0^t\mathrm{d}\tau c_n^{(\mathrm{I})}(\tau)\alpha_n^*(\tau)\alpha_n(\tau)}\\&\times\mathrm{e}^{-\kappa^2\sum\limits_{nm}\int\limits_0^t\mathrm{d}\tau\int\limits_0^\tau\mathrm{d}\tau'\mathcal{C}_{nm}^{(0)}(t-\tau)\alpha_n^*(\tau)\alpha_n(\tau)\alpha_m^*\left(\tau'\right)\alpha_m\left(\tau'\right)}.\end{aligned}\tag{2.30}$$

Here we introduced the function $c_n^{(\mathrm{I})}\left(t\right)=z_n^{(\mathrm{I})}\left(t\right)+w_n^{(\mathrm{I})}\left(t\right)$. From here we can follow the same procedure as in the previous subsection and obtain a stochastic differential equation for $\psi_{\mathrm{F}}^{(\mathrm{I})}\left(\boldsymbol{\alpha}^*,\boldsymbol{\alpha},\boldsymbol{\beta}_f^*,\boldsymbol{\beta}_i;t\right)\to\left|\psi^{(\mathrm{I})}\left(\boldsymbol{\beta}_f^*,\boldsymbol{\beta}_i;t\right)\right\rangle$:

$$\begin{aligned}\frac{\mathrm{d}}{\mathrm{d}t}\left|\psi^{(\mathrm{I})}\left(\boldsymbol{\beta}_f^*,\boldsymbol{\beta}_i;t\right)\right\rangle=-\mathrm{i}\Bigg(&\widehat{H}_{\mathrm{S}}+\kappa\sum_n c_n^{(\mathrm{I})}\left(t\right)\widehat{a}_n^\dagger\widehat{a}_n-\mathrm{i}\kappa^2\sum_{nm}\widehat{a}_n^\dagger\widehat{a}_n\\&\times\int\limits_0^t\mathrm{d}\tau\mathcal{C}_{nm}^{(0)}\left(t-\tau\right)\frac{\delta}{\delta c_m^{(\mathrm{I})}\left(\tau\right)}\Bigg)\left|\psi^{(\mathrm{I})}\left(\boldsymbol{\beta}_f^*,\boldsymbol{\beta}_i;t\right)\right\rangle.\end{aligned}\tag{2.31}$$

The corresponding final expression of the reduced density operator reads

$$\widehat{\rho}_{\mathrm{red}}(t)=\int_{-\infty}^{\infty}\mathrm{d}^2\boldsymbol{\beta}_f\int_{-\infty}^{\infty}\mathrm{d}^2\boldsymbol{\beta}_i\prod_k p_k\left(\boldsymbol{\beta}_f,\boldsymbol{\beta}_i\right)\left|\psi^{(\mathrm{I})}\left(\boldsymbol{\beta}_f^*,\boldsymbol{\beta}_i;t\right)\right\rangle\left\langle\psi^{(\mathrm{I})}\left(\boldsymbol{\beta}_i^*,\boldsymbol{\beta}_f;t\right)\right| \tag{2.32}$$

Here the Gaussian probability density is

$$p_k\left(\boldsymbol{\beta}_f,\boldsymbol{\beta}_i\right)=\frac{1}{\overline{n}_k}\mathrm{e}^{-\beta_{f,k}^*\beta_{f,k}-\beta_{i,k}^*\beta_{i,k}\left(\overline{n}_k^{-1}+1\right)+\beta_{f,k}^*\beta_{i,k}+\beta_{i,k}^*\beta_{f,k}}. \tag{2.33}$$

.

2.1.3 Interpretation of SSE

Comparing the two stochastic Schrödinger equations (Eqs. (2.19) and (2.31)) it is evident that both forms have the same structure: a coherent evolution term with $\widehat{H}_{\mathrm{S}}$, the stochastic term with noises $c_n^{(\mathrm{S})}(t)$ and $c_n^{(\mathrm{I})}(t)$and the memory term with the time integral. In the mathematical sense both fluctuations $c_n^{(\mathrm{S})}(t)$ and $c_n^{(\mathrm{I})}(t)$ are Fourier transforms of multidimensional (in principle infinite-dimensional) vectors of random Gaussian variables $\boldsymbol{x}_Z,\boldsymbol{x}_W$ and $\boldsymbol{\beta}_f,\boldsymbol{\beta}_i$ respectively. Their physical interpretation arises from the fact that both these functions are related to bath degrees of freedom. In case of Schrödinger picture SSE (2.19) the noise $c_n^{(\mathrm{S})}(t)$ is constructed from terms containing the Bose–Einstein function $\overline{n}_k$ which describes the average number of excitations of energy ω_k at temperature T in the bath. Thus, $c_n^{(\mathrm{S})}(t)$ must be related to the fluctuations of the heat bath and this function is the manifestation of bath's influence over the system. The same holds true for for the noise $c_n^{(\mathrm{I})}(t)$ only here the temperature dependence arises from the probability density $p_k\left(\boldsymbol{\beta}_f,\boldsymbol{\beta}_i\right)$. In this case we also see more clearly the nature of fluctuation $c_n^{(\mathrm{I})}(t)$ as it depends on the initial and final points of bath trajectories $\boldsymbol{\beta}_f$ and $\boldsymbol{\beta}_i$ (see Eqs. (2.2) - (2.5)), hence $c_n^{(\mathrm{I})}(t)$ indeed represents the evolution of the bath between two distinct configurations.

The main characteristic of any fluctuation is its correlation function. The correlation function between two noises $c_n^{(\mathrm{S})}(t)$ and $c_m^{(\mathrm{S})}(t)$ can be calculated using the formula

$$\begin{aligned}\mathcal{C}_{nm}(t)=\left\langle c_n^{(\mathrm{S})*}(t)\,c_m^{(\mathrm{S})}(0)\right\rangle_{\boldsymbol{x}_Z,\boldsymbol{x}_W}&=\int_{-\infty}^{\infty}\mathrm{d}^2\boldsymbol{x}_Z\int_{-\infty}^{\infty}\mathrm{d}^2\boldsymbol{x}_W p\left(\boldsymbol{x}_Z,\boldsymbol{x}_W\right)\\&\times c_{n,\boldsymbol{x}_Z,\boldsymbol{x}_W}^{(\mathrm{S})*}(t)\,c_{m,\boldsymbol{x}_Z,\boldsymbol{x}_W}^{(\mathrm{S})}(0).\end{aligned} \tag{2.34}$$

Here $\langle \cdots \rangle_{\boldsymbol{x}_Z,\boldsymbol{x}_W}$ denotes the statistical average over the random variables $\boldsymbol{x}_Z$ and $\boldsymbol{x}_W$. Calculating the correlation function $\mathcal{C}^{(\mathrm{I})}_{nm}(t) = \left\langle c^{(\mathrm{I})*}_n(t)\, c^{(\mathrm{I})}_m(0) \right\rangle_{\boldsymbol{\beta}_f,\boldsymbol{\beta}_i}$ in a similar manner we can show that both functions are equal and read

$$\begin{aligned}\mathcal{C}^{(\mathrm{S})}_{nm}(t) = \mathcal{C}^{(\mathrm{I})}_{nm}(t) &= \sum_k g^*_{nk} g_{mk} \left(\mathrm{e}^{-\mathrm{i}\omega_k t} (\overline{n}_k + 1) + \mathrm{e}^{\mathrm{i}\omega_k t} \overline{n}_k \right) \\ &= \sum_k g^*_{nk} g_{mk} \left(\cos(\omega_k t) \coth\left(\frac{\omega_k \beta_T}{2} \right) - \mathrm{i} \sin(\omega_k t) \right). \quad (2.35)\end{aligned}$$

Eq. (2.35) can be recognized as the standard correlation of function of bath fluctuations arising in arbitrary thermodynamic system at small deviations from the equilibrium [12, 13, 18]. It is very convenient to modify Eq. (2.35) by introducing the bath spectral density function $\mathcal{C}''_{nm}(\omega) = \sum_k g^*_{nk} g_{mk} \delta(\omega - \omega_k)$ yielding

$$\mathcal{C}_{nm}(t) = \int_0^\infty \mathrm{d}\omega \left(\cos(\omega t) \coth\left(\frac{\omega \beta_T}{2} \right) - \mathrm{i} \sin(\omega t) \right) \mathcal{C}''_{nm}(\omega). \quad (2.36)$$

Here $\mathcal{C}^{(\mathrm{S})}_{nm}(t) = \mathcal{C}^{(\mathrm{I})}_{nm}(t) = \mathcal{C}_{nm}(t)$. When the number of bath oscillators is very large spectral density $\mathcal{C}''_{nm}(\omega)$ essentially becomes a smooth function and represents the continuous distribution of frequencies in the bath. The explicit form of the spectral density depends on the microscopic model chosen to describe the environment, e. g. the Debye model, the ohmic and super-ohmic models [18]. Functional form of the Debye spectral density reads

$$\mathcal{C}''(\omega) = \frac{2\lambda \omega_{\mathrm{D}} \omega}{\omega_{\mathrm{D}}^2 + \omega^2} \quad (2.37)$$

and the super-ohmic is given by

$$\mathcal{C}''(\omega) = \frac{\pi \lambda}{\Gamma(s)} \frac{\omega^s}{\omega_{\mathrm{SO}}^s} \mathrm{e}^{-\frac{\omega}{\omega_{\mathrm{SO}}}}. \quad (2.38)$$

In both models of the spectral density $\lambda = \frac{1}{\pi} \int_0^\infty \mathrm{d}\omega \frac{\mathcal{C}''(\omega)}{\omega}$ is the reorganization energy [12, 13] parametrizing the system–bath coupling strength instead of the quantity κ ((2.1)) which in further calculations is set to 1. In Debye spectral density ω_{D} is the inverse bath fluctuations correlation time, while a similar quantity in the super-ohmic model is denoted by ω_{SO}. In the latter spectral density s is the parameter distinguishing several regimes of the bath fluctuations: sub-ohmic when $s < 1$, ohmic when $s = 1$ and super-ohmic when $s > 1$. $\Gamma(s)$ is the Euler Gamma

function.

As a consequence of having differently defined fluctuations in the two stochastic Schrödinger equations (2.19) and (2.31) the time integral terms in both equations are not identical. While $\mathcal{C}_{nm}(t)$ in Eq. (2.19) is identified as the finite-temperature correlation function (2.35), the function $\mathcal{C}_{nm}^{(0)}(t)$ is actually the zero-temperature version of $\mathcal{C}_{nm}(t)$.

Looking back at the discussion in Section 1 about the impossibility of describing the reduced system's dynamics with a single pure state or with a wave vector, it is important to carefully interpret physical meaning of the stochastic wave vectors obtained in Subsections 2.1.1 and 2.1.2. Stochastic Schrödinger equations (2.19) and (2.31) are equations for the wave vector $\left|\psi(t)\right\rangle$, hence similar to Eq. (1.2). However, in Section 1 we argued that such equation describing the exact dynamics of the reduced system cannot possibly be found and it would seem that the SSE formalism has an inherent flaw. To solve this discrepancy we must go back to the definition of the reduced density operator (1.4). Let us denote the degrees of freedom of the small system by $\boldsymbol{q}$ and those of the bath by $\boldsymbol{Q}$. Then the wave vector of the global system $\left|\Psi(\boldsymbol{q},\boldsymbol{Q};t)\right\rangle$ can be expressed in the following way:

$$\left|\Psi(\boldsymbol{q},\boldsymbol{Q};t)\right\rangle = \int \mathrm{d}\boldsymbol{q} \int \mathrm{d}\boldsymbol{Q} f(\boldsymbol{q},\boldsymbol{Q};t) \left|\boldsymbol{q}\right\rangle \otimes \left|\boldsymbol{Q}\right\rangle. \tag{2.39}$$

Here $\left|\boldsymbol{q}\right\rangle$, $\left|\boldsymbol{Q}\right\rangle$ are the orthonormal basis vectors of the system and the bath respectively and the expansion coefficient $f(\boldsymbol{q},\boldsymbol{Q};t) \neq f_{\mathrm{S}}(\boldsymbol{q};t)\, f_{\mathrm{B}}(\boldsymbol{Q};t)$ in general case is not separable as the wave vector $\left|\Psi(t)\right\rangle$ can be entangled. If we calculate the partial trace of the global density operator $\widehat{W}(t)$ we get

$$\begin{aligned}
\widehat{\rho}_{\mathrm{red}}(\boldsymbol{q},\boldsymbol{q}';t) &= \int \mathrm{d}\boldsymbol{Q} \int \mathrm{d}\boldsymbol{Q}' \int \mathrm{d}\boldsymbol{Q}'' \left\langle \boldsymbol{Q}''\middle|\boldsymbol{Q}\right\rangle \left\langle \boldsymbol{Q}'\middle|\boldsymbol{Q}''\right\rangle \\
&\quad \times \int \mathrm{d}\boldsymbol{q} \int \mathrm{d}\boldsymbol{q}' f(\boldsymbol{q},\boldsymbol{Q};t)\, f^{*}\left(\boldsymbol{q}',\boldsymbol{Q}';t\right) \left|\boldsymbol{q}\right\rangle \left\langle \boldsymbol{q}'\right| \\
&= \int \mathrm{d}\boldsymbol{Q} \int \mathrm{d}\boldsymbol{Q}' \int \mathrm{d}\boldsymbol{Q}'' p\left(\boldsymbol{Q},\boldsymbol{Q}',\boldsymbol{Q}''\right) \left|F(\boldsymbol{q},\boldsymbol{Q};t)\right\rangle \left\langle F\left(\boldsymbol{q}',\boldsymbol{Q}';t\right)\right|
\end{aligned} \tag{2.40}$$

with $p\left(\boldsymbol{Q},\boldsymbol{Q}',\boldsymbol{Q}''\right) = \left\langle \boldsymbol{Q}''\middle|\boldsymbol{Q}\right\rangle \left\langle \boldsymbol{Q}'\middle|\boldsymbol{Q}''\right\rangle$ and $\left|F(\boldsymbol{q},\boldsymbol{Q};t)\right\rangle = \int \mathrm{d}\boldsymbol{q} f(\boldsymbol{q},\boldsymbol{Q};t) \left|\boldsymbol{q}\right\rangle$. We see that $\left|F(\boldsymbol{q},\boldsymbol{Q};t)\right\rangle$ are wave vectors acting in the Hilbert space of the system but they carry a functional dependence on bath degrees of freedom $\boldsymbol{Q}$. Eq. (2.40) clearly indicates that the reduced density operator here describes a mixed state but what is the exact physical meaning of states $\left|F(\boldsymbol{q},\boldsymbol{Q};t)\right\rangle$? To answer that we should address this problem from a different angle. Let us calculate the probability

to find the bath in a particular state $\left|\boldsymbol{Q}''\right\rangle$ if the global system is described by the wave vector (2.39). We obtain the expression

$$\begin{aligned} P\left(\boldsymbol{Q}'';t\right) &= \left|\left\langle \boldsymbol{Q}''\right|\Psi\left(\boldsymbol{q},\boldsymbol{Q};t\right)\right\rangle\right|^2 = \left(\int \mathrm{d}\boldsymbol{Q}\left\langle \boldsymbol{Q}\right|\left.\boldsymbol{Q}''\right\rangle \int \mathrm{d}\boldsymbol{q} f^*\left(\boldsymbol{q},\boldsymbol{Q};t\right)\left\langle \boldsymbol{q}\right|\right) \\ &\times \left(\int \mathrm{d}\boldsymbol{Q}\left\langle \boldsymbol{Q}''\right|\left.\boldsymbol{Q}\right\rangle \int \mathrm{d}\boldsymbol{q} f\left(\boldsymbol{q},\boldsymbol{Q};t\right)\left|\boldsymbol{q}\right\rangle\right) \\ &= \int \mathrm{d}\boldsymbol{Q}\int \mathrm{d}\boldsymbol{Q}'\left\langle \boldsymbol{Q}''\right|\left.\boldsymbol{Q}\right\rangle\left\langle \boldsymbol{Q}'\right|\left.\boldsymbol{Q}''\right\rangle\left\langle F\left(\boldsymbol{q}',\boldsymbol{Q}'\right)\right|F\left(\boldsymbol{q},\boldsymbol{Q}\right)\right\rangle \\ &= \left\langle F\left(\boldsymbol{q}',\boldsymbol{Q}'';t\right)\right|F\left(\boldsymbol{q},\boldsymbol{Q}'';t\right)\right\rangle \\ &= \int \mathrm{d}\boldsymbol{q} f^*\left(\boldsymbol{q},\boldsymbol{Q}'';t\right) f\left(\boldsymbol{q},\boldsymbol{Q}'';t\right) \end{aligned} \tag{2.41}$$

where we used the fact that $\left|\boldsymbol{q}\right\rangle$ and $\left|\boldsymbol{Q}\right\rangle$ span an orthonormal basis, thus, $\left\langle \boldsymbol{Q}'\right|\left.\boldsymbol{Q}\right\rangle = \delta\left(\boldsymbol{Q}'-\boldsymbol{Q}\right)$ and $\left\langle \boldsymbol{q}'\right|\left.\boldsymbol{q}\right\rangle = \delta\left(\boldsymbol{q}'-\boldsymbol{q}\right)$.

Eq. (2.41) shows that the probability $P\left(\boldsymbol{Q}'';t\right)$ to find the bath in a particular configuration is equal to the overlap between the states $\left\langle F\left(\boldsymbol{q}',\boldsymbol{Q}'';t\right)\right|F\left(\boldsymbol{q},\boldsymbol{Q}'';t\right)\right\rangle$, hence we can interpret them as being the wave vectors of the small system when the bath is in a particular state. In other words it means we obtain the system wave vector $\left|F\left(\boldsymbol{q},\boldsymbol{Q}'';t\right)\right\rangle$ if the state of the bath is continuously monitored (measured) at every moment in time and thus, giving a definite stochastic trajectory $\boldsymbol{Q}''\left(t\right)$. In practice such a scenario would be quite difficult to implement, especially when the number of bath DOF to control is very large. However, as the reduced density operator (2.40) is used to calculate experimentally measurable quantities, theoretically we still can use the stochastic wave vector to give statistical information on the system dynamics because $\widehat{\rho}_{\mathrm{red}}\left(\boldsymbol{q},\boldsymbol{q}';t\right)$ is expressed as a statistical average over bath DOF, thus, making $\left|F\left(\boldsymbol{q},\boldsymbol{Q};t\right)\right\rangle$ a single realization of the statistical ensemble of all configurations of the bath.

It is important to mention that the norm $\left\|\left|F\left(\boldsymbol{q},\boldsymbol{Q};t\right)\right\rangle\right\|$ of the stochastic vector is not necessarily unity. This it is understandable because $P\left(\boldsymbol{Q};t\right) = \left\|\left|F\left(\boldsymbol{q},\boldsymbol{Q};t\right)\right\rangle\right\|^2$ is the probability of finding the bath in a particular state $\left|\boldsymbol{Q}\right\rangle$, hence it can vary between 0 and 1. If $P\left(\boldsymbol{Q};t\right)$ always were equal to 1 it would mean that there is only one available configuration of the bath which is obviously not true. However, postulates of quantum mechanics tell us that the norm of a wave vector has to remain constant and equal to 1 at all times so that it is regarded as a proper state descriptor. Hence, in order to comply with this requirement the stochastic wave vector $\left|F\left(\boldsymbol{q},\boldsymbol{Q};t\right)\right\rangle$ has to be renormalized at each moment in time. This renormalization can be done in two ways: analytical and numerical. In the an-

alytical approach a normalized stochastic wave vector $\left|\widetilde{F}\left(\boldsymbol{q},\boldsymbol{Q};t\right)\right\rangle = \frac{\left|F(\boldsymbol{q},\boldsymbol{Q};t)\right\rangle}{\left\|\left|F(\boldsymbol{q},\boldsymbol{Q};t)\right\rangle\right\|}$ is introduced and a non-linear stochastic equation is derived. Such equations for the SSEs of the form (2.19) and (2.31) were first presented in [39]. The numerical approach consists of numerically solving the linear SSE while explicitly renormalizing the stochastic wave vector at every time step. Such a procedure is justified because renormalization is just a multiplication of the stochastic wave vector $\left|F\left(\boldsymbol{q},\boldsymbol{Q};t\right)\right\rangle$ by a factor which does not change the relative magnitudes of different components of the wave vector, thus the relative probabilities of different events calculated from $\left|F\left(\boldsymbol{q},\boldsymbol{Q};t\right)\right\rangle$ and $\left|\widetilde{F}\left(\boldsymbol{q},\boldsymbol{Q};t\right)\right\rangle$ also stay the same.

2.2 Weak system–bath coupling approximation [P1, P3, P6]

The memory terms in both Eqs. (2.19) and (2.31) contain a functional derivative with respect to noise under the time integral. Such integrand is difficult to calculate in practice, thus an alternative form of the memory term is desirable. The easiest way to derive it is first to go back to Eq. (2.2) without encasing the reduced density operator in coherent states $\left\langle\boldsymbol{\alpha}_f\right|$ and $\left|\boldsymbol{\alpha}'_f\right\rangle$, hence obtaining the operator equation

$$\begin{aligned}\widehat{\rho}_{\mathrm{red}}\left(t\right) = \int\limits_{-\infty}^{\infty}\prod_k \mathrm{d}^2\beta_{f,k}\mathrm{d}^2\beta_{i,k}\frac{1}{\overline{n}_k}\mathrm{e}^{-\beta^*_{f,k}\beta_{f,k}-\beta^*_{i,k}\beta_{i,k}\left(\overline{n}_k^{-1}+1\right)}\\ \times\left\langle\boldsymbol{\beta}_f\right|\widehat{U}\left(t\right)\left|\boldsymbol{\beta}_i\right\rangle\left|\boldsymbol{\alpha}_i\right\rangle\left\langle\boldsymbol{\alpha}'_i\right|\left\langle\boldsymbol{\beta}_i\right|\widehat{U}^\dagger\left(t\right)\left|\boldsymbol{\beta}_f\right\rangle.\end{aligned} \tag{2.42}$$

Here the evolution $\widehat{U}\left(t\right)$ is the interaction picture evolution operator from Eq. (2.23). In all subsequent chapters we will use only the interaction picture stochastic Schrödinger equation derived in Subsection 2.1.2, hence we drop the (I) superscript from the notations to make them less cluttered.

We can interpret the quantities $\widehat{\mathcal{U}}\left(t\right) = \left\langle\boldsymbol{\beta}_f\right|\widehat{U}\left(t\right)\left|\boldsymbol{\beta}_i\right\rangle$ and its Hermitian conjugate as the evolution operators in the Hilbert space of the system. Defining the wave vector $\left|\psi\left(\boldsymbol{\beta}^*_f,\boldsymbol{\beta}_i;t\right)\right\rangle = \mathrm{e}^{-\boldsymbol{\beta}^*_f\boldsymbol{\beta}_i}\widehat{\mathcal{U}}\left(t\right)\left|\boldsymbol{\alpha}_i\right\rangle$ we can calculate its time derivative and obtain the evolution equation:

$$\begin{aligned}\frac{\mathrm{d}}{\mathrm{d}t}\left|\psi\left(\boldsymbol{\beta}^*_f,\boldsymbol{\beta}_i;t\right)\right\rangle &= \mathrm{e}^{-\boldsymbol{\beta}^*_f\boldsymbol{\beta}_i}\left\langle\boldsymbol{\beta}_f\right|\frac{\mathrm{d}}{\mathrm{d}t}\widehat{U}\left(t\right)\left|\boldsymbol{\beta}_i\right\rangle\left|\boldsymbol{\alpha}_i\right\rangle\\ &= -\mathrm{i}\widehat{H}_{\mathrm{S}}\left|\psi\left(\boldsymbol{\beta}^*_f,\boldsymbol{\beta}_i;t\right)\right\rangle - \mathrm{i}\kappa\sum_{nk}\widehat{a}^\dagger_n\widehat{a}_n g_{nk}\mathrm{e}^{\mathrm{i}\omega_k t}\beta^*_{f,k}\end{aligned}$$

$$\times \left|\psi\left(\boldsymbol{\beta}_f^*, \boldsymbol{\beta}_i; t\right)\right\rangle - \mathrm{i}\mathrm{e}^{-\boldsymbol{\beta}_f^* \boldsymbol{\beta}_i \kappa} \sum_{nk} \widehat{a}_n^\dagger \widehat{a}_n g_{nk}^* \mathrm{e}^{-\mathrm{i}\omega_k t}$$
$$\times \left\langle \boldsymbol{\beta}_f \middle| \widehat{b}_k \widehat{U}\left(t\right) \middle| \boldsymbol{\beta}_i \right\rangle \middle| \boldsymbol{\alpha}_i \right\rangle. \tag{2.43}$$

We make the substitution $\widehat{b}_k \widehat{U}\left(t\right) = \widehat{U}\left(t\right) \widehat{b}_k\left(t\right)$ where $\widehat{b}_k\left(t\right) = \widehat{U}^\dagger\left(t\right) \widehat{b}_k \widehat{U}\left(t\right)$ is the Heisenberg representation of the annihilation operator and it explicitly reads

$$\widehat{b}_k\left(t\right) = \widehat{b}_k - \mathrm{i}\kappa \sum_n \int_0^t \mathrm{d}\tau g_{nk} \mathrm{e}^{\mathrm{i}\omega_k \tau} \widehat{U}^\dagger\left(\tau\right) \widehat{a}_n^\dagger \widehat{a}_n \widehat{U}\left(\tau\right). \tag{2.44}$$

Using Eq. (2.44) evolution equation for the system wave vector becomes

$$\begin{aligned}
\frac{\mathrm{d}}{\mathrm{d}t}\left|\psi\left(\boldsymbol{\beta}_f^*, \boldsymbol{\beta}_i; t\right)\right\rangle = & -\mathrm{i}\widehat{H}_{\mathrm{S}} \left|\psi\left(\boldsymbol{\beta}_f^*, \boldsymbol{\beta}_i; t\right)\right\rangle \\
& - \mathrm{i}\kappa \sum_{nk} \widehat{a}_n^\dagger \widehat{a}_n g_{nk} \mathrm{e}^{\mathrm{i}\omega_k t} \beta_{f,k}^* \left|\psi\left(\boldsymbol{\beta}_f^*, \boldsymbol{\beta}_i; t\right)\right\rangle \\
& - \mathrm{i}\kappa \sum_{nk} \widehat{a}_n^\dagger \widehat{a}_n g_{nk}^* \mathrm{e}^{-\mathrm{i}\omega_k t} \beta_{i,k} \left|\psi\left(\boldsymbol{\beta}_f^*, \boldsymbol{\beta}_i; t\right)\right\rangle \\
& - \kappa^2 \sum_{nm} \widehat{a}_n^\dagger \widehat{a}_n \int_0^t \mathrm{d}\tau \sum_k g_{nk}^* g_{nk} \mathrm{e}^{-\mathrm{i}\omega_k (t-\tau)} \\
& \times \widehat{\mathcal{U}}\left(t\right) \widehat{\mathcal{U}}^\dagger\left(\tau\right) \widehat{a}_m^\dagger \widehat{a}_m \widehat{\mathcal{U}}\left(\tau\right) \widehat{\mathcal{U}}^\dagger\left(t\right) \left|\psi\left(\boldsymbol{\beta}_f^*, \boldsymbol{\beta}_i; t\right)\right\rangle,
\end{aligned} \tag{2.45}$$

where $\widehat{\mathcal{U}}\left(t\right)$ has the form (2.23) with (see Appendix A for details)

$$\widehat{H}\left(t\right) \to \widehat{\mathcal{H}}\left(t\right) = \widehat{H}_{\mathrm{S}} + \kappa \sum_{nk} \widehat{a}_n^\dagger \widehat{a}_n \left(g_{nk} \mathrm{e}^{\mathrm{i}\omega_k t} \beta_{f,k}^* + g_{nk}^* \mathrm{e}^{-\mathrm{i}\omega_k t} \frac{\partial}{\partial \beta_{f,k}^*} \right). \tag{2.46}$$

In Eq. (2.45) we notice that the fluctuation terms with the variables $\beta_{f,k}^*$ and $\beta_{i,k}$ are exactly the same as in Eq. (2.27) and the function under the time integral is $\mathcal{C}_{nm}^{(0)}\left(t-\tau\right)$. We notice that the memory term now does not contain the functional derivative with respect to the noise. The final form of this stochastic Schrödinger equation is

$$\frac{\mathrm{d}}{\mathrm{d}t}\left|\psi\left(\boldsymbol{\beta}_f^*, \boldsymbol{\beta}_i; t\right)\right\rangle = -\mathrm{i} \left(\widehat{H}_{\mathrm{S}} + \kappa \sum_n c_n\left(t\right) \widehat{a}_n^\dagger \widehat{a}_n - \mathrm{i}\kappa^2 \sum_{nm} \widehat{a}_n^\dagger \widehat{a}_n \int_0^t \mathrm{d}\tau \mathcal{C}_{nm}^{(0)}\left(t-\tau\right) \right.$$

$$\times \widehat{\mathcal{U}}(t)\widehat{\mathcal{U}}^{\dagger}(\tau)\widehat{a}_m^{\dagger}\widehat{a}_m\widehat{\mathcal{U}}(\tau)\widehat{\mathcal{U}}^{\dagger}(t)\Bigg)\left|\psi\left(\boldsymbol{\beta}_f^*,\boldsymbol{\beta}_i;t\right)\right\rangle. \tag{2.47}$$

Doing actual calculations with Eq. (2.47) is still difficult due to the dependence of $\widehat{\mathcal{U}}(t)$ on partial derivatives $\frac{\partial}{\partial\beta_{f,k}^*}$. However, when the system–bath coupling is weak ($\max\left(\left|\kappa g_{nk}\right|\right) \ll \min\left(\left|\widehat{H}_{\mathrm{S},nm}\right|\right)$) we can drop the term linear in κ in Eq. (2.46), thus transforming the operator $\widehat{\mathcal{U}}(t) \approx \mathrm{e}^{-\mathrm{i}\widehat{H}_{\mathrm{S}}t}$ to a simple evolution operator of the closed system $\widehat{H}_{\mathrm{S}}$ alone. Inserting this expression into Eq. (2.47) we get the weak coupling approximation form of the stochastic Schrödinger equation:

$$\frac{\mathrm{d}}{\mathrm{d}t}\left|\psi\left(\boldsymbol{\beta}_f^*,\boldsymbol{\beta}_i;t\right)\right\rangle = -\mathrm{i}\Bigg(\widehat{H}_{\mathrm{S}} + \kappa\sum_n c_n(t)\,\widehat{a}_n^{\dagger}\widehat{a}_n - \mathrm{i}\kappa^2\sum_{nm}\widehat{a}_n^{\dagger}\widehat{a}_n\int_0^t \mathrm{d}\tau\mathcal{C}_{nm}^{(0)}(\tau)$$
$$\times\, \mathrm{e}^{-\mathrm{i}\widehat{H}_{\mathrm{S}}\tau}\widehat{a}_m^{\dagger}\widehat{a}_m\mathrm{e}^{\mathrm{i}\widehat{H}_{\mathrm{S}}\tau}\Bigg)\left|\psi\left(\boldsymbol{\beta}_f^*,\boldsymbol{\beta}_i;t\right)\right\rangle. \tag{2.48}$$

2.3 Hierarchical stochastic Schrödinger equation [P6]

In the previous section we demonstrated how a practical form of stochastic Schrödinger equation (2.48) suitable for numerical calculations can be obtained. However, this equation is only approximate and valid only when the system–bath interaction is sufficiently weak. It is important to find a way to harness the full power of the formally exact SSE in Eq. (2.47). One way to deal with the difficult memory term consisting of a product of evolution operators $\widehat{\mathcal{U}}$ is to avoid introducing them in the first place and derive a system of coupled stochastic equations equivalent to the original equation. We start from the Eq. (2.43) and insert the unity operator $\int_{-\infty}^{\infty}\mathrm{d}^2\boldsymbol{\gamma}_1\mathrm{e}^{-\boldsymbol{\gamma}_1^*\boldsymbol{\gamma}_1}\left|\boldsymbol{\gamma}_1\right\rangle\left\langle\boldsymbol{\gamma}_1\right|$ between the annihilation operator $\widehat{b}_k$ and the evolution operator $\widehat{U}(t)$ in the third term of the equation:

$$-\mathrm{i}\mathrm{e}^{-\boldsymbol{\beta}_f^*\boldsymbol{\beta}_i}\kappa\sum_{nk}\widehat{a}_n^{\dagger}\widehat{a}_n g_{nk}^*\mathrm{e}^{-\mathrm{i}\omega_k t}\left\langle\boldsymbol{\beta}_f\right|\widehat{b}_k\widehat{U}(t)\left|\boldsymbol{\beta}_i\right\rangle\left|\boldsymbol{\alpha}_i\right\rangle$$
$$= -\mathrm{i}\mathrm{e}^{-\boldsymbol{\beta}_f^*\boldsymbol{\beta}_i}\kappa\sum_n\widehat{a}_n^{\dagger}\widehat{a}_n\int_{-\infty}^{\infty}\mathrm{d}^2\boldsymbol{\gamma}_1\mathrm{e}^{-\boldsymbol{\gamma}_1^*\boldsymbol{\gamma}_1}\sum_k g_{nk}^*\mathrm{e}^{-\mathrm{i}\omega_k t}$$
$$\times\left\langle\boldsymbol{\beta}_f\right|\widehat{b}_k\left|\boldsymbol{\gamma}_1\right\rangle\left\langle\boldsymbol{\gamma}_1\right|\widehat{U}(t)\left|\boldsymbol{\beta}_i\right\rangle\left|\boldsymbol{\alpha}_i\right\rangle$$

$$= -\mathrm{i}\mathrm{e}^{-\boldsymbol{\beta}_f^*\boldsymbol{\beta}_i}\kappa\sum_n \widehat{a}_n^\dagger\widehat{a}_n \int\limits_{-\infty}^{\infty}\mathrm{d}^2\boldsymbol{\gamma}_1\mathrm{e}^{-\boldsymbol{\gamma}_1^*\boldsymbol{\gamma}_1+\boldsymbol{\beta}_f^*\boldsymbol{\gamma}_1+\boldsymbol{\gamma}_1^*\boldsymbol{\beta}_i}$$
$$\times\sum_k g_{nk}^*\mathrm{e}^{-\mathrm{i}\omega_k t}\gamma_{1,k}\mathrm{e}^{-\boldsymbol{\gamma}_1^*\boldsymbol{\beta}_i}\big\langle\boldsymbol{\gamma}_1\big|\widehat{U}\left(t\right)\big|\boldsymbol{\beta}_i\big\rangle\big|\boldsymbol{\alpha}_i\big\rangle. \tag{2.49}$$

In the expression (2.49) we can define an auxiliary wave vector in the space of the system $\big|\psi\left(\boldsymbol{\gamma}_1^*,\boldsymbol{\beta}_i;t\right)\big\rangle = \mathrm{e}^{-\boldsymbol{\gamma}_1^*\boldsymbol{\beta}_i}\left\langle\boldsymbol{\gamma}_1\right|\widehat{U}\left(t\right)\left|\boldsymbol{\beta}_i\right\rangle\left|\boldsymbol{\alpha}_i\right\rangle$. With this definition Eq. (2.43) can be written in the following way:

$$\frac{\mathrm{d}}{\mathrm{d}t}\big|\psi\left(\boldsymbol{\beta}_f^*,\boldsymbol{\beta}_i;t\right)\big\rangle = -\mathrm{i}\widehat{H}_\mathrm{S}\big|\psi\left(\boldsymbol{\beta}_f^*,\boldsymbol{\beta}_i;t\right)\big\rangle - \mathrm{i}\kappa\sum_n\widehat{a}_n^\dagger\widehat{a}_n z_n\left(t\right)\big|\psi\left(\boldsymbol{\beta}_f^*,\boldsymbol{\beta}_i;t\right)\big\rangle$$
$$-\mathrm{i}\kappa\sum_n\widehat{a}_n^\dagger\widehat{a}_n\int\limits_{-\infty}^{\infty}\mathrm{d}^2\boldsymbol{\gamma}_1 p_{\boldsymbol{\beta}_f^*,\boldsymbol{\beta}_i}\left(\boldsymbol{\gamma}_1^*,\boldsymbol{\gamma}_1\right)s_{1,n}(t)\big|\psi\left(\boldsymbol{\gamma}_1^*,\boldsymbol{\beta}_i;t\right)\big\rangle. \tag{2.50}$$

Here we introduced the function $s_{1,n}(t)=\sum\limits_k g_{nk}^*\mathrm{e}^{-\mathrm{i}\omega_k t}\gamma_{1,k}$ and the probability density function $p_{\boldsymbol{\beta}_f^*,\boldsymbol{\beta}_i}\left(\boldsymbol{\gamma}_1^*,\boldsymbol{\gamma}_1\right)=\mathrm{e}^{-\boldsymbol{\gamma}_1^*\boldsymbol{\gamma}_1+\boldsymbol{\beta}_f^*\boldsymbol{\gamma}_1+\boldsymbol{\gamma}_1^*\boldsymbol{\beta}_i-\boldsymbol{\beta}_f^*\boldsymbol{\beta}_i}$. The integral in the third term of the Eq. (2.50) can be interpreted as the average over the multidimensional Gaussian random variable $\boldsymbol{\gamma}_1$, analogically as it was done in Eq. (2.29). The resulting Eq. (2.50) now depends on the wave vector $\big|\psi\left(\boldsymbol{\gamma}_1^*,\boldsymbol{\beta}_i;t\right)\big\rangle$. The form of this wave vector is identical to the expression of the original wave vector $\big|\psi\left(\boldsymbol{\beta}_f^*,\boldsymbol{\beta}_i;t\right)\big\rangle$, thus, it is governed by the same equation (2.50) and we can write:

$$\frac{\mathrm{d}}{\mathrm{d}t}\big|\psi\left(\boldsymbol{\gamma}_1^*,\boldsymbol{\beta}_i;t\right)\big\rangle = -\mathrm{i}\widehat{H}_\mathrm{S}\big|\psi\left(\boldsymbol{\gamma}_1^*,\boldsymbol{\beta}_i;t\right)\big\rangle - \mathrm{i}\kappa\sum_n\widehat{a}_n^\dagger\widehat{a}_n s_{1,n}^*(t)\big|\psi\left(\boldsymbol{\gamma}_1^*,\boldsymbol{\beta}_i;t\right)\big\rangle$$
$$-\mathrm{i}\kappa\sum_n\widehat{a}_n^\dagger\widehat{a}_n\int\limits_{-\infty}^{\infty}\mathrm{d}^2\boldsymbol{\gamma}_2 p_{\boldsymbol{\gamma}_1^*,\boldsymbol{\beta}_i}\left(\boldsymbol{\gamma}_2^*,\boldsymbol{\gamma}_2\right)s_{2,n}(t)\big|\psi\left(\boldsymbol{\gamma}_2^*,\boldsymbol{\beta}_i;t\right)\big\rangle. \tag{2.51}$$

where we again inserted another unity operator $\int\limits_{-\infty}^{\infty}\mathrm{d}^2\boldsymbol{\gamma}_2\mathrm{e}^{-\boldsymbol{\gamma}_2^*\boldsymbol{\gamma}_2}\big|\boldsymbol{\gamma}_2\big\rangle\big\langle\boldsymbol{\gamma}_2\big|$ in the third term and defined the a new auxiliary wave vector $\big|\psi\left(\boldsymbol{\gamma}_2^*,\boldsymbol{\beta}_i;t\right)\big\rangle$. From the structure of the Eq. (2.51) it is clear that performing the procedure described above M times we can arrive at the equation for the wave vector $\big|\psi\left(\boldsymbol{\gamma}_M^*,\boldsymbol{\beta}_i;t\right)\big\rangle$, thus obtaining a system of coupled stochastic differential equation. This system will be completely equivalent to the formally exact stochastic Schrödinger equation (2.47) only if the

hierarchy is infinite. Such form is of little use for practical applications, thus the hierarchy must be terminated at some finite order M, i. e., the last equation for $\left|\psi\left(\boldsymbol{\gamma}_M^*, \boldsymbol{\beta}_i; t\right)\right\rangle$ should have a closed form as in Eq. (2.47). However, with increasing order M of the hierarchy the equation (2.50) describing the evolution of the system wave vector $\left|\psi\left(\boldsymbol{\beta}_f^*, \boldsymbol{\beta}_i; t\right)\right\rangle$ effectively becomes of order $M+1$ in system–bath coupling strength κ. Thus in the last equation of the hierarchy we can make the weak system–bath coupling approximation which introduces only higher than $M+1$ order errors in the final expression of $\left|\psi\left(\boldsymbol{\beta}_f^*, \boldsymbol{\beta}_i; t\right)\right\rangle$. Alternatively, we can in principle use the zero-order in κ equation:

$$\frac{\mathrm{d}}{\mathrm{d}t}\left|\psi\left(\boldsymbol{\gamma}_M^*, \boldsymbol{\beta}_i; t\right)\right\rangle = -\mathrm{i}\widehat{H}_{\mathrm{S}}\left|\psi\left(\boldsymbol{\gamma}_M^*, \boldsymbol{\beta}_i; t\right)\right\rangle. \tag{2.52}$$

Thus the complete hierarchy of equations can be written in the following way:

$$\begin{aligned}
\frac{\mathrm{d}}{\mathrm{d}t}\left|\psi\left(\boldsymbol{\beta}_f^*, \boldsymbol{\beta}_i; t\right)\right\rangle &= -\mathrm{i}\left(\widehat{H}_{\mathrm{S}} + \kappa\sum_n \widehat{a}_n^\dagger \widehat{a}_n z_n\left(t\right)\right)\left|\psi\left(\boldsymbol{\beta}_f^*, \boldsymbol{\beta}_i; t\right)\right\rangle \\
&\quad - \mathrm{i}\kappa\sum_n \widehat{a}_n^\dagger \widehat{a}_n \left\langle s_{1,n}(t)\middle|\psi\left(\boldsymbol{\gamma}_1^*, \boldsymbol{\beta}_i; t\right)\right\rangle\right\rangle_{\boldsymbol{\gamma}_1}, \\
\frac{\mathrm{d}}{\mathrm{d}t}\left|\psi\left(\boldsymbol{\gamma}_1^*, \boldsymbol{\beta}_i; t\right)\right\rangle &= -\mathrm{i}\left(\widehat{H}_{\mathrm{S}} + \kappa\sum_n \widehat{a}_n^\dagger \widehat{a}_n s_{1,n}^*(t)\right)\left|\psi\left(\boldsymbol{\gamma}_1^*, \boldsymbol{\beta}_i; t\right)\right\rangle \\
&\quad - \mathrm{i}\kappa\sum_n \widehat{a}_n^\dagger \widehat{a}_n \left\langle s_{2,n}(t)\middle|\psi\left(\boldsymbol{\gamma}_2^*, \boldsymbol{\beta}_i; t\right)\right\rangle\right\rangle_{\boldsymbol{\gamma}_2}, \\
&\quad \ldots \\
\frac{\mathrm{d}}{\mathrm{d}t}\left|\psi\left(\boldsymbol{\gamma}_M^*, \boldsymbol{\beta}_i; t\right)\right\rangle &= -\mathrm{i}\left(\widehat{H}_{\mathrm{S}} + \kappa\sum_n \widehat{a}_n^\dagger \widehat{a}_n s_{M,n}^*(t) + \kappa\sum_n \widehat{a}_n^\dagger \widehat{a}_n w_n(t)\right. \\
&\quad \left. -\mathrm{i}\kappa^2\sum_{nm}\widehat{a}_n^\dagger \widehat{a}_n \int_0^t \mathrm{d}\tau C_{nm}^{(0)}(\tau)\mathrm{e}^{-\mathrm{i}\widehat{H}_{\mathrm{S}}\tau}\widehat{a}_m^\dagger \widehat{a}_m \mathrm{e}^{\mathrm{i}\widehat{H}_{\mathrm{S}}\tau}\right)\left|\psi\left(\boldsymbol{\gamma}_M^*, \boldsymbol{\beta}_i; t\right)\right\rangle.
\end{aligned} \tag{2.53}$$

Here $\left\langle\cdots\right\rangle_{\boldsymbol{\gamma}_j}$ denotes the average with respect to the Gaussian probability density $p_{\boldsymbol{\gamma}_{j-1}^*, \boldsymbol{\beta}_i}\left(\boldsymbol{\gamma}_j^*, \boldsymbol{\gamma}_j\right)$ in the third term of the j-th equation of the hierarchy.

Let us investigate the average $\left\langle s_{j,n}(t)\middle|\psi\left(\boldsymbol{\gamma}_j^*, \boldsymbol{\beta}_i; t\right)\right\rangle\right\rangle_{\boldsymbol{\gamma}_j}$ more closely. The probability density $p_{\boldsymbol{\gamma}_{j-1}^*, \boldsymbol{\beta}_i}\left(\boldsymbol{\gamma}_j^*, \boldsymbol{\gamma}_j\right)$ in this expression can be transformed to the standard Gaussian form by using the substitutions of variables $\boldsymbol{\gamma}_j^* = \widetilde{\boldsymbol{\gamma}}_j^* + \boldsymbol{\gamma}_{j-1}^*$ and $\boldsymbol{\gamma}_j = \widetilde{\boldsymbol{\gamma}}_j + \boldsymbol{\beta}_i$. We get

$$\begin{aligned}\left\langle s_{j,n}(t)\middle|\psi\left(\boldsymbol{\gamma}_j^*,\boldsymbol{\beta}_i;t\right)\right\rangle\right\rangle_{\boldsymbol{\gamma}^{(j)}} &= \int_{-\infty}^{\infty}\mathrm{d}^2\widetilde{\gamma}_j p\left(\widetilde{\gamma}_j^*,\widetilde{\gamma}_j\right)\sum_k g_{nk}^*\mathrm{e}^{-\mathrm{i}\omega_k t}\\ &\times\left(\widetilde{\gamma}_{j,k}+\beta_{i,k}\right)\left|\psi\left(\widetilde{\gamma}_j^*+\boldsymbol{\gamma}_{j-1}^*,\boldsymbol{\beta}_i;t\right)\right\rangle\\ &= \int_{-\infty}^{\infty}\mathrm{d}^2\widetilde{\gamma}_j p\left(\widetilde{\gamma}_j^*,\widetilde{\gamma}_j\right)\left(\widetilde{s}_{j,n}(t)+w_n\left(t\right)\right)\\ &\times\left|\psi\left(\widetilde{\gamma}_j^*+\boldsymbol{\gamma}_{j-1}^*,\boldsymbol{\beta}_i;t\right)\right\rangle, \qquad (2.54)\end{aligned}$$

where $\widetilde{s}_{j,n}(t)=\sum_k g_{nk}^*\mathrm{e}^{-\mathrm{i}\omega_k t}\widetilde{\gamma}_{j,k}$. Relation (2.54) shows us that the j-th auxiliary wave vector $\left|\psi\left(\widetilde{\gamma}_j^*+\boldsymbol{\gamma}_{j-1}^*,\boldsymbol{\beta}_i;t\right)\right\rangle$ depends on all previous $\boldsymbol{\gamma}$ variables, thus $\boldsymbol{\gamma}_j^*=\sum_{l=1}^{j}\widetilde{\gamma}_l^*+\boldsymbol{\beta}_f^*$ and the hierarchy (2.53) reads

$$\begin{aligned}\frac{\mathrm{d}}{\mathrm{d}t}\left|\psi\left(\boldsymbol{\beta}_f^*,\boldsymbol{\beta}_i;t\right)\right\rangle &= -\mathrm{i}\left(\widehat{H}_{\mathrm{S}}+\kappa\sum_n\widehat{a}_n^\dagger\widehat{a}_n z_n\left(t\right)\right)\left|\psi\left(\boldsymbol{\beta}_f^*,\boldsymbol{\beta}_i;t\right)\right\rangle\\ &-\mathrm{i}\kappa\sum_n\widehat{a}_n^\dagger\widehat{a}_n\left\langle\left(\widetilde{s}_{1,n}(t)+w_n(t)\right)\left|\psi\left(\boldsymbol{\gamma}_1^*,\boldsymbol{\beta}_i;t\right)\right\rangle\right\rangle_{\boldsymbol{\gamma}_1},\\ \frac{\mathrm{d}}{\mathrm{d}t}&\left|\psi\left(\boldsymbol{\gamma}_1^*,\boldsymbol{\beta}_i;t\right)\right\rangle\\ &= -\mathrm{i}\left(\widehat{H}_{\mathrm{S}}+\kappa\sum_n\widehat{a}_n^\dagger\widehat{a}_n\left(\widetilde{s}_{1,n}^*(t)+z_n\left(t\right)\right)\right)\left|\psi\left(\boldsymbol{\gamma}_1^*,\boldsymbol{\beta}_i;t\right)\right\rangle\\ &-\mathrm{i}\kappa\sum_n\widehat{a}_n^\dagger\widehat{a}_n\left\langle\left(\widetilde{s}_{2,n}(t)+w_n(t)\right)\left|\psi\left(\boldsymbol{\gamma}_2^*,\boldsymbol{\beta}_i;t\right)\right\rangle\right\rangle_{\boldsymbol{\gamma}_2}, \qquad (2.55)\end{aligned}$$

$\ldots$

$$\begin{aligned}\frac{\mathrm{d}}{\mathrm{d}t}\left|\psi\left(\boldsymbol{\gamma}_M^*,\boldsymbol{\beta}_i;t\right)\right\rangle &= -\mathrm{i}\left(\widehat{H}_{\mathrm{S}}+\kappa\sum_n\widehat{a}_n^\dagger\widehat{a}_n\left(\sum_{l=1}^{M}\widetilde{s}_{l,n}^*(t)+z_n\left(t\right)+w_n(t)\right)\right.\\ &\left.-\mathrm{i}\kappa^2\sum_{nm}\widehat{a}_n^\dagger\widehat{a}_n\int_0^t\mathrm{d}\tau C_{nm}^{(0)}(\tau)\mathrm{e}^{-\mathrm{i}\widehat{H}_{\mathrm{S}}\tau}\widehat{a}_m^\dagger\widehat{a}_m\mathrm{e}^{\mathrm{i}\widehat{H}_{\mathrm{S}}\tau}\right)\left|\psi\left(\boldsymbol{\gamma}_M^*,\boldsymbol{\beta}_i;t\right)\right\rangle.\end{aligned}$$

2.3.1 Solving the hierarchical stochastic Schrödinger equation

Solving the hierarchy in Eq. (2.55) directly is a difficult numerical task due to the necessity of generating many auxiliary noises and then calculating statistical average over them. In order to avoid such problems one would need to obtain a form of the

hierarchical stochastic Schrödinger equation were the Gaussian integrations over auxiliary fluctuations are solved analytically. One way to achieve this is to start with the last equation in the hierarchy (2.55) and write the formal solution of it using the propagator $\widehat{\mathcal{G}}_M(t)$:

$$\widehat{\mathcal{G}}_M(t)\left|\boldsymbol{\alpha}_i\right\rangle = \widehat{T}_+ \mathrm{e}^{-\mathrm{i}\int_0^t \mathrm{d}\tau \widehat{H}'_M(\tau)}\left|\boldsymbol{\alpha}_i\right\rangle, \tag{2.56}$$

where $\widehat{H}'_M(\tau)$ is the operator in the parentheses of the last equation in the hierarchy (2.55). We can see that the propagator depends on the complex conjugate noises $\widetilde{s}^*_{M,n}(t) = \sum_k g_{nk}\mathrm{e}^{\mathrm{i}\omega_k t}\widetilde{\gamma}^*_{M,k}$, thus we can expand it with respect to the Gaussian variables $\widetilde{\gamma}^*_{M,k}$:

$$\widehat{\mathcal{G}}_j\left[\widetilde{s}^*_{M,n}(t)\right] = \widehat{\mathcal{G}}_M[0] + \sum_k \left.\frac{\partial\widehat{\mathcal{G}}_M\left[\widetilde{s}^*_{M,n}(t)\right]}{\partial\widetilde{\gamma}^*_{M,k}}\right|_{\widetilde{s}^*_{M,n}(t)\equiv 0}\widetilde{\gamma}^*_{M,k} + \ldots \tag{2.57}$$

Here $\widehat{\mathcal{G}}_M[0] = \widehat{\mathcal{G}}_M(t)\big|_{\widetilde{s}^*_{M,n}(t)\equiv 0} \equiv \widehat{\mathcal{G}}_{M,0}(t)$. Calculating the first order term is a bit tricky due to the fact that $\left.\frac{\partial\widehat{H}'_M(t)}{\partial\widetilde{\gamma}^*_{M,k}}\right|_{\widetilde{s}^*_{M,n}(t)\equiv 0}$ does not commute with $\widehat{\mathcal{G}}_M\left[\widetilde{s}^*_{M,n}(t)\right]$. In this case we must apply the general expression for the first order derivative of an exponential operator [40]:

$$\left.\frac{\mathrm{d}}{\mathrm{d}\eta}\,\mathrm{e}^{\widehat{A}+\eta\widehat{B}}\right|_{\eta=0} = \int_0^1 \mathrm{d}s\mathrm{e}^{(1-s)\widehat{A}}\widehat{B}\mathrm{e}^{s\widehat{A}}, \tag{2.58}$$

where $\left[\widehat{A},\widehat{B}\right] \neq 0$. Thus, the first order expansion term in Eq. (2.57) is given by

$$\left.\frac{\partial\widehat{\mathcal{G}}_M\left[\widetilde{s}^*_{M,n}(t)\right]}{\partial\widetilde{\gamma}^*_{M,k}}\right|_{\widetilde{s}^*_{M,n}(t)\equiv 0} = -\mathrm{i}\kappa\int_0^1 \mathrm{d}s\widehat{\mathcal{G}}^{1-s}_{M,0}(t)\int_0^t \mathrm{d}\tau\sum_n \widehat{a}^\dagger_n\widehat{a}_n\widetilde{s}^*_{M,n}(\tau)\,\widehat{\mathcal{G}}^s_{M,0}(t)\,. \tag{2.59}$$

Now we insert this expression into the $M-1$-th auxiliary equation of the hierarchy (2.55) and for the Gaussian integral term we obtain

$$\kappa\sum_n \widehat{a}^\dagger_n\widehat{a}_n\left\langle\left(\widetilde{s}_{M,n}(t) + w_n(t)\right)\widehat{\mathcal{G}}_M(t)\left|\boldsymbol{\alpha}_i\right\rangle\right\rangle_{\boldsymbol{\gamma}_M} = \kappa\sum_n \widehat{a}^\dagger_n\widehat{a}_n w_n(t)\widehat{\mathcal{G}}_{M,0}(t)\left|\boldsymbol{\alpha}_i\right\rangle$$

$$
\begin{aligned}
&- \mathrm{i}\kappa^2 \sum_{nm} \widehat{a}_n^\dagger \widehat{a}_n \int_0^t \mathrm{d}\tau C_{nm}^{(0)}(t-\tau) \int_0^1 \mathrm{d}s \widehat{\mathcal{G}}_{M,0}^{1-s}(t)\, \widehat{a}_m^\dagger \widehat{a}_m \widehat{\mathcal{G}}_{M,0}^{s}(t) \left|\boldsymbol{\alpha}_i\right\rangle \\
&\equiv \widehat{Q}_{M-1}(t) \left|\boldsymbol{\alpha}_i\right\rangle. \qquad (2.60)
\end{aligned}
$$

In Eq. (2.60) only the terms which contain the combination of noises $\left(\widetilde{s}_{M,n}(t)\widetilde{s}_{M,n}^*(\tau)\right)^q$ where $q = 0, 1, 2...$ survive the Gaussian integration due to the unshifted form of the probability density. However, the noise $\widetilde{\gamma}_{M,n}(t)$ always enters only with the $q = 1$, thus the highest order needed in expansion (2.57) is only the first order and in this case the result (2.60) is exact. Now the hierarchy contains $M-1$ equations for auxiliary wave vectors where the last one reads

$$
\begin{aligned}
\frac{\mathrm{d}}{\mathrm{d}t}\left|\psi\left(\boldsymbol{\gamma}_{M-1}^*, \boldsymbol{\beta}_i; t\right)\right\rangle = -\mathrm{i}\left(\widehat{H}_\mathrm{S} + \kappa \sum_n \widehat{a}_n^\dagger \widehat{a}_n \left(\sum_{l=1}^{M-1} \widetilde{s}_{l,n}^*(t) + z_n(t)\right)\right) \\
\times \left|\psi\left(\boldsymbol{\gamma}_{M-1}^*, \boldsymbol{\beta}_i; t\right)\right\rangle - \mathrm{i}\widehat{Q}_{j-1}(t)\left|\boldsymbol{\alpha}_i\right\rangle. \qquad (2.61)
\end{aligned}
$$

Eq. (2.61) again can be solved and the propagator of $\left|\psi\left(\boldsymbol{\gamma}_{M-1}^*, \boldsymbol{\beta}_i; t\right)\right\rangle$ has the following form:

$$
\widehat{\mathcal{G}}_{M-1}(t) = \widehat{P}_{M-1}(t) - \mathrm{i}\widehat{P}_{M-1}(t) \int_0^t \mathrm{d}\tau \widehat{P}_{M-1}^\dagger(\tau)\, \widehat{Q}_{M-1}(\tau). \qquad (2.62)
$$

Here $\widehat{P}_{M-1}(t) = \widehat{T}_+ \mathrm{e}^{-\mathrm{i}\int_0^t \mathrm{d}\tau \left[\widehat{H}_\mathrm{S} + \kappa \sum_n \widehat{a}_n^\dagger \widehat{a}_n \left(\sum_{l=1}^{M-1} \widetilde{s}_{l,n}^*(\tau) + z_n(\tau)\right)\right]}$. In order to use the propagator $\widehat{\mathcal{G}}_{M-1}(t)$ in the $M-2$-th auxiliary equation it has to be expanded in the similar fashion as in Eq. (2.57) up to the first order in variables $\widetilde{\gamma}_{j-1,k}^*$. This process must be continued until reaching the very first equation if the hierarchy (2.55) which then reads:

$$
\frac{\mathrm{d}}{\mathrm{d}t}\left|\psi\left(\boldsymbol{\beta}_f^*, \boldsymbol{\beta}_i; t\right)\right\rangle = -\mathrm{i}\left(\widehat{H}_\mathrm{S} + \kappa \sum_n \widehat{a}_n^\dagger \widehat{a}_n z_n(t)\right)\left|\psi\left(\boldsymbol{\beta}_f^*, \boldsymbol{\beta}_i; t\right)\right\rangle - \mathrm{i}\widehat{Q}_0(t)\left|\boldsymbol{\alpha}_i\right\rangle. \qquad (2.63)
$$

Here the non-homogeneous contribution $\widehat{Q}_0(t)$ takes into account all the effects captured by the subsequent equation in the hierarchy, thus, in principle Eq. (2.63) is absolutely exact and equivalent to Eq. (2.47).

2.4 Performance of the stochastic Schrödinger equation [P3, P6]

All forms of full stochastic Schrödinger equations in Eqs. (2.19), (2.31), (2.47) and hierarchies (2.53), (2.55) in principle offer an exact treatment of the reduced system dynamics when linearly coupled to a bath of harmonic oscillators. However, as it was argued in chapters above the formally exact SSE is very difficult to solve, hence the weak system–bath coupling was introduced in Eq. (2.48) which is more tractable numerically. In this section we will compare the performance of the weak-coupling stochastic Schrödinger equation to other popular methods used for studying the dynamics of open quantum systems such as Redfield equation and Hierarchical Equations of Motion (see Section 1.2 for more details about these approaches). We also test similarly the performance of 1- and 2-level hierarchical stochastic Schrödinger equation (2.55) calculated using the approach in Subsection 2.3.1. Both weak coupling SSE and HSSE mathematically are systems of coupled first order homogeneous differential equations. They can be solved using many different numerical methods, however we chose the explicit embedded Runge-Kutta Cash-Karp (4, 5) method implemented in the scientific GSL library [41].

2.4.1 Noise generation

The hierarchical and ordinary stochastic Schrödinger equations depend on the noise functions $c_n(t)$ which must be known before solving the system itself. Thus, a major part of obtaining the time evolution of the stochastic wave vector $\left|\psi\left(\boldsymbol{\beta}_f^*, \boldsymbol{\beta}_i; t\right)\right\rangle \equiv \left|\psi(t)\right\rangle$ is the generation of fluctuation trajectories. One method for obtaining these stochastic trajectories is by application of the Wiener–Khinchin theorem [12, 42, 43]. Suppose the autocorrelation matrix of the stationary ergodic noise vector $\boldsymbol{c}(t) = (c_1(t), c_2(t), \ldots, c_n(t), \ldots)$ is $\boldsymbol{\mathcal{C}}(t) = \int_{-\infty}^{\infty} \mathrm{d}\tau \boldsymbol{c}^{*T}(t-\tau)\,\boldsymbol{c}(\tau)$. Then the Wiener –Khinchin theorem states that

$$\boldsymbol{\mathcal{C}}(t) = \frac{1}{2\pi}\int_{-\infty}^{\infty} \mathrm{d}\omega \mathrm{e}^{-\mathrm{i}\omega t}\boldsymbol{c}^{*T}(\omega)\,\boldsymbol{c}(\omega)\,. \tag{2.64}$$

Here the function $\boldsymbol{c}(\omega)$ is simply the Fourier transform $\boldsymbol{c}(\omega) = \int_{-\infty}^{\infty} \mathrm{d}t \mathrm{e}^{\mathrm{i}\omega t}\boldsymbol{c}(t)$ of the time-domain fluctuation vector $\boldsymbol{c}(t)$. Next we notice that Eq. (2.64) is the inverse Fourier transform of the function $\boldsymbol{\mathcal{C}}(\omega) = \boldsymbol{c}^{*T}(\omega)\,\boldsymbol{c}(\omega)$ and when the correlation function $[\boldsymbol{\mathcal{C}}(t)]_{nm}$ is given by Eq. (2.36) its frequency domain representation reads

$$[\boldsymbol{\mathcal{C}}(\omega)]_{nm} = \left(1 + \coth\frac{\omega\beta_T}{2}\right)\mathcal{C}''_{nm}(\omega)\,. \tag{2.65}$$

Comparing Eqs. (2.64) and (2.65) we can deduce that $\boldsymbol{c}(\omega) = \boldsymbol{\phi}(\omega)\sqrt{\boldsymbol{\mathcal{C}}(\omega)}$, where $\boldsymbol{\phi}(\omega) = \left(\mathrm{e}^{\mathrm{i}\phi_1(\omega)}, \mathrm{e}^{\mathrm{i}\phi_2(\omega)}, \ldots, \mathrm{e}^{\mathrm{i}\phi_n(\omega)}, \ldots\right)$. Thus, the fluctuation vector in time domain can be obtained performing the inverse Fourier transform:

$$\boldsymbol{c}(t) = \frac{1}{2\pi}\int_{-\infty}^{\infty}\mathrm{d}\omega\mathrm{e}^{-\mathrm{i}\omega t}\boldsymbol{\phi}(\omega)\sqrt{\boldsymbol{\mathcal{C}}(\omega)}. \tag{2.66}$$

Here the functions $\phi_n(\omega)$ must be random-valued so that $\boldsymbol{c}(t)$ is stochastic as well. According to the central limit theorem, the distribution of a sum obtained from a large number of random variables is Gaussian. It follows that the probability density function of the fluctuation $\boldsymbol{c}(t)$ remains Gaussian regardless of the distribution of the function under the integral. For this reason, we use the simple uncorrelated random process to generate the function $\phi_n(\omega)$ in the interval $[0, 2\pi)$. To have the real-valued stochastic trajectory of $\boldsymbol{c}(t)$ at high temperature (classical fluctuations), we also set $\phi_n(\omega) = -\phi_n(-\omega)$.

One difficulty arising when applying Eq. (2.66) is the calculation of the square root of matrix $\boldsymbol{\mathcal{C}}(\omega)$, which can be understood in terms of its as power series expansion. Since this matrix is real and symmetric by construction (see Eqs. (2.36) and (2.65)) it is diagonalizable, thus it can be written as $\boldsymbol{\mathcal{C}} = \boldsymbol{Q}\boldsymbol{D}\boldsymbol{Q}^{-1}$ where $\boldsymbol{D}$ is the diagonal matrix of the eigenvalues and $\boldsymbol{Q}$ is the unitary transform matrix consisting of eigenvectors of $\boldsymbol{\mathcal{C}}$. In this case it is known from linear algebra that for any function f we have the relation $f(\boldsymbol{\mathcal{C}}) = f\left(\boldsymbol{Q}\boldsymbol{D}\boldsymbol{Q}^{-1}\right) = \boldsymbol{Q}f(\boldsymbol{D})\boldsymbol{Q}^{-1}$ and, as $\boldsymbol{D}$ is diagonal, $[f(\boldsymbol{D})]_{nm} = f([\boldsymbol{D}]_{nm})$. Eq. (2.66) is valid for an arbitrary matrix of spectral density $\mathcal{C}''_{nm}(\omega)$, thus it describes correlated fluctuations when $\mathcal{C}''_{nm}(\omega) \neq 0$ for $n \neq m$. However, in all applications of the stochastic Schrödinger equation in this thesis we are assuming uncorrelated fluctuations – noises coupled to different system sites are independent. In this case the spectral density matrix $\mathcal{C}''_{nm}(\omega)$ is diagonal and thus there is no need for diagonalization of $\boldsymbol{\mathcal{C}}(\omega)$ and the matrix equation (2.66) can be simplified to

$$c_n(t) = \frac{1}{2\pi}\int_{-\infty}^{\infty}\mathrm{d}\omega\mathrm{e}^{-\mathrm{i}\omega t+\mathrm{i}\phi_n(\omega)}\sqrt{[\boldsymbol{\mathcal{C}}(\omega)]_{nn}}. \tag{2.67}$$

We use this noise generation method when solving the weak-coupling SSE (2.48).

Another method for generating fluctuations consists of straightforward application of the noise functions' $c_n(t)$ and $\widetilde{s}_{j,n}(t)$ definitions from Eqs. (2.27) and (2.54).

For this we need to generate a set of Gaussian complex random variables with the appropriate probability density distribution. Let us start with the generation of fluctuations driving the weak coupling stochastic Schrödinger equation (2.48). Noises $c_n(t)$ by their definition are sums of random variables

$$c_n(t) = z_n(t) + w_n(t) = \sum_k g_{nk} \mathrm{e}^{\mathrm{i}\omega_k \tau} \beta^*_{f,k} + \sum_k g^*_{nk} \mathrm{e}^{-\mathrm{i}\omega_k \tau} \beta_{i,k}. \tag{2.68}$$

Here $\beta^*_{f,k}$ and $\beta_{i,k}$ are Gaussian random variables characterized by the probability density (2.33). We can introduce new random vectors $\boldsymbol{b}^*_k = \left(\beta^*_{f,k}, \beta^*_{i,k}\right)$ and $\boldsymbol{b}^T_k = (\beta_{f,k}, \beta_{i,k})$ and rewrite the probability density as

$$p_k\left(\boldsymbol{\beta}_f, \boldsymbol{\beta}_i\right) = \frac{1}{\overline{n}_k} \mathrm{e}^{-\frac{1}{2}\boldsymbol{b}^{*T}_k \boldsymbol{\Sigma}^{-1}_k \boldsymbol{b}_k} \tag{2.69}$$

with $\boldsymbol{\Sigma}^{-1}_k = 2 \begin{pmatrix} 1 & -1 \\ -1 & \overline{n}^{-1}_k + 1 \end{pmatrix}$ acting as the inverse of the covariance matrix. It is obvious that variables $\beta_{f,k}$ and $\beta_{i,k}$ are not independent, thus they cannot be generated separately from each other. However, just as in 1D Gaussian in the current 2D case the required random values can be obtained from the normal Gaussian distribution. In order to do that with substitution $\boldsymbol{r}_k = \boldsymbol{S}_k \boldsymbol{b}_k$ we transform the exponent in Eq. (2.69) to $-\frac{1}{2}\boldsymbol{b}^{*T}_k \boldsymbol{\Sigma}^{-1}_k \boldsymbol{b}_k = -\frac{1}{2}\boldsymbol{r}^{*T}_k \boldsymbol{D}^{-1}_k \boldsymbol{r}_k$ where $\boldsymbol{D}^{-1}_k = \begin{pmatrix} \sigma^{-2}_{1,k} & 0 \\ 0 & \sigma^{-2}_{2,k} \end{pmatrix}$ is the diagonal matrix consisting of the eigenvalues of $\boldsymbol{\Sigma}^{-1}_k$ and $\boldsymbol{S}_k$ is the transform matrix constructed from the eigenvectors of $\boldsymbol{\Sigma}^{-1}_k$. The transformed probability density represents a simple Gaussian distribution of variables $\boldsymbol{r}_k$ characterized by the covariance matrix $\boldsymbol{D}_k$. Thus, the n-th component of $\boldsymbol{r}_k$ can be generated by drawing a random variable from the normal distribution $\mathcal{N}(0,1)$ and multiplying it by $\sigma_{n,k}$. Having the vector $\boldsymbol{r}_k$ it is easy to obtain the original vector $\boldsymbol{b}_k$ using the relation $\boldsymbol{b}_k = \boldsymbol{S}^{-1}_k \boldsymbol{r}_k$. According to Eq. (2.68) we construct vectors $\boldsymbol{z}_n = \left(g_{n1}\beta^*_{f,k}, \ldots, g_{nk}\beta^*_{f,k}, \ldots\right)$ and $\boldsymbol{w}_n = (g^*_{n1}\beta_{i,k}, \ldots, g^*_{nk}\beta_{i,k}, \ldots)$ where we identify $g_{nk} = g^*_{nk} = \sqrt{\mathcal{C}''_{nm}(\omega_k)}$. Now the noises $z_n(t)$ and $w_n(t)$ can be obtained by calculating respectively the inverse Fourier transform of $\boldsymbol{z}_n$ and the Fourier transform of $\boldsymbol{w}_n$ using the numerical Fast Fourier Transform routines. We use this noise generation method when solving the HSSE (2.55) where fluctuations $z_n(t)$ and $w_n(t)$ appear not in a sum but separately.

2.4.2 Calculation of observables

Stochastic Schrödinger equation (2.48) and corresponding hierarchy (2.55) are written using the second quantization creation and annihilation operators $\widehat{a}_n^\dagger/\widehat{a}_n$, hence they are already suitable for describing many particle system's dynamics. However, in this thesis we only study single particle systems which translates into the requirement that $\widehat{a}_n^\dagger\widehat{a}_m^\dagger = \widehat{a}_n\widehat{a}_m \equiv 0$, thus there are only two available states for the n-th bosonic degree of freedom - $\big|0\big\rangle_n$ containing 0 particles and $\big|1\big\rangle_n = \widehat{a}_n^\dagger\big|0\big\rangle_n$ containing a single particle. Since we are solving the single-particle evolution problem we can define a new basis in the Hilbert space of the system called site basis and corresponding to states $\big|n\big\rangle \equiv \bigotimes_m \big|\delta_{nm}\big\rangle_m$ when the n-th bosonic degree of freedom is populated. Now each bosonic degree of freedom is referred to as a site and in this basis the stochastic wave vector can be written as $\big|\psi\left(t\right)\big\rangle = \sum_n \psi_n\left(t\right)\big|n\big\rangle$.

Having a set of noises $c_n\left(t\right)$ we can solve the stochastic equation system and obtain one realization of the stochastic wave vector. For each realization r of the statistical ensemble a different set of noises $c_n\left(t\right)$ has to be generated. We usually want to calculate some mean value of a quantum observable $\overline{O}\left(t\right) = \big\langle\psi\left(t\right)\big|\widehat{O}\big|\psi\left(t\right)\big\rangle$, which is a random quantity, different in each realization. In general the ensemble-averaged mean value of an observable $\big\langle\overline{O}\left(t\right)\big\rangle_{\text{ens}} = \frac{1}{R}\sum_{r=1}^{R}\big\langle\psi_r\left(t\right)\big|\widehat{O}\big|\psi_r\left(t\right)\big\rangle$ is calculated averaging over R realizations of the stochastic wave vector $\big|\psi_r\left(t\right)\big\rangle$. If we gather the random values of $\overline{O}\left(t\right)$ from every realization it is easy to group this data set into a histogram and thus obtain an approximation of the probability density distribution $p_t\left(\overline{O}\right)$. It is important to remember that stochastic Schrödinger equation (2.48) and hierarchy (2.55) are not normalized just as Eqs. (2.19) and (2.31), thus we renormalize numerically the stochastic wave vector $\big|\psi_r\left(t\right)\big\rangle$ at every time step.

In order to test the suitability of the SSE to describe the dynamics of the reduced system we can calculate the whole reduced density matrix (populations and coherences) of the system and compare it to the results obtained by other methods. Averaged density matrix elements in the site basis $\big|n\big\rangle$ can be calculated using the wave vector as

$$\rho_{nm}\left(t\right) = \big\langle\psi_n^*\left(t\right)\psi_m\left(t\right)\big\rangle_{\text{ens}}. \tag{2.70}$$

A common situation encountered while investigating the dynamics of an open quantum system is when we need to determine the time τ_{tr} it takes for the excitation in the system to reach some defined state $\big|\zeta\big\rangle$ starting with an initial state $\big|\psi\left(0\right)\big\rangle$. Using the SSE (2.48) formalism we can naturally define this transition time τ_{tr} and construct the distribution of its values from the vast ensemble of different realizations of the stochastic wave vector $\big|\psi\left(t\right)\big\rangle$.

The transfer time is a stochastic property, unique for each member of the ensemble. Moreover τ_{tr} is a stochastic property even for a single member of the ensemble. From the theory of stochastic Markovian systems [43], it is known that the actual transition time from the initial state 1 to the final state 2, when the process is characterized by a single rate constant, must be a random number distributed according to the exponential law with the properly defined mean transition time equal to the inverse of the rate, i.e., $p(t) = B\mathrm{e}^{-k_{1\to 2}t}$. Consequently the mean transition time is given by $\tau_{1\to 2} = 1/k_{1\to 2}$. Hence, using the Fermi Golden Rule (FGR) [13] (or the Redfield theory), the mean transition time can be evaluated as the inverse of calculated transition rates. However, the Redfield theory as well as the rate concepts are valid only for the weak coupling regimes. In the case of intermediate or strong couplings, the HEOM method allows to exactly propagate the density matrix, however in this case it becomes difficult to define the rates and the transition times. In general, additional heuristic arguments may be necessary to define the transition times based on the density matrix population evolution. We next suggest a stochastic method to simulate the excitation transition time using the stochastic Schrödinger equation, which allows to properly define and evaluate the excitation transition time distribution function even if it is not exponential.

The meaning of the transition time implies that we start with a predefined state of the system and after some time we observe another state. Hence, to calculate the transition time to an arbitrary state of the system, first we have to define the process of the measurement (detection) of the excitation in the necessary state. This measurement procedure can be constructed in the following way. The system wave vector with components $\psi_n(t)$ is a stochastic variable depending on a set of fluctuations $c_n(t)$ according to Eq. (2.48). Additionally, the magnitudes of the components of the wave vector are generally nonzero. For this reason, the system can be found in an arbitrary state at an arbitrary time. We can calculate the overlap of the final state and the wave vector of the system $\langle\zeta|\psi(t)\rangle$ and according to the postulates of quantum mechanics the probability of finding the system in the state $|\zeta\rangle$ is now $p_{i\to f} = |\langle\zeta|\psi(t)\rangle|^2$. If the excitation is found in the state $|\zeta\rangle$, the system state collapses to $|\zeta\rangle$, we determine the arrival time and stop the propagation. This measurement process can be modeled using the Monte Carlo method by drawing a random number r uniformly distributed in the interval $[0, 1)$ before starting the propagation with the SSE (2.48). Now during the propagation as soon as we find $r < |\langle\zeta|\psi(\tau_{tr})\rangle|^2$, we register the excitation in the state $|\zeta\rangle$ and τ_{tr} is defined as the transition time. Due to the fact that the system state evolves stochastically and the random number r takes unique values for each propagation, the excitation detection condition is fulfilled at different time moments in each realization. With a sufficient number of realizations we can then calculate the distribution of the

transition time. Hence, the algorithm of the excitation registration in the state $\left|\zeta\right\rangle$ and construction of the transition time distribution can be summarized as follows:

1. A uniformly distributed random number r is generated in the interval $[0, 1)$.
2. The system wave vector is propagated, and at every time step the condition $r < \left|\left\langle\zeta\middle|\psi\left(\tau_{tr}\right)\right\rangle\right|^2$ is checked.
3. If the condition is satisfied, the propagation is stopped and the excitation transition time to the state $\left|\zeta\right\rangle$ is recorded; otherwise the propagation (step 2) is continued.
4. Stages 1–3 are repeated for the same system until a statistically sufficient amount of results is obtained.
5. The distribution of transition times is constructed as the histogram of the recorded times τ_{tr}.

This procedure is illustrated in Fig. 2.1 for the special case when the final state $\left|\zeta\right\rangle = \left|2\right\rangle$ is a site basis state of the system: the excitation detection time is marked by crossing point of r and $\left|\left\langle 2\middle|\psi\left(t\right)\right\rangle\right|^2$.

2.4.3 Application of the SSE to a toy system

To validate the stochastic Schrödinger equation theory, let us consider the evolution of a simple two-site system and investigate the situation when the coupling between the sites as well as the system–bath interaction is weak and the correlation time of bath fluctuations is short. We set the parameters of the system Hamiltonian $\widehat{H}_{\mathrm{S}}$ to $\epsilon_1 = 100\,\mathrm{cm}^{-1}$, $\epsilon_2 = 0\,\mathrm{cm}^{-1}$, $J_{12} = J_{21} = 9\,\mathrm{cm}^{-1}$ and generate the thermal noise from the Debye spectral density (2.37) with inverse correlation time $\omega_{\mathrm{D}} = 10\,\mathrm{fs}^{-1}$ and system–bath coupling of $\lambda = 2\,\mathrm{cm}^{-1}$ at temperature $T = 300\,\mathrm{K}$. The initial wave vector of the system is chosen to be $\left|\psi\left(0\right)\right\rangle = \left|1\right\rangle$, thus populating the higher energy site.

In Fig. 2.1 we illustrate the stochasticity of the SSE by showing two particular realizations of the second site population $\rho_{22}\left(t\right)$. It can clearly be seen that two stochastic trajectories quickly diverge and it is impossible to make any conclusions about the evolution of the system solely from individual realizations. This divergence of the population trajectories reflects how quickly two distinct trajectories of the bath degrees of freedom lead the system away from the coherent evolution. Summing many such realizations leads to the ensemble-averaged population dynamics depicted in Fig. 2.2 where the blue curve is calculated with $J_{12} = 13.5\,\mathrm{cm}^{-1}$ and the red one - with $J_{12} = 9\,\mathrm{cm}^{-1}$. When the inter-site and system–bath couplings are weak the dynamics of the system is incoherent and can be satisfactorily described by

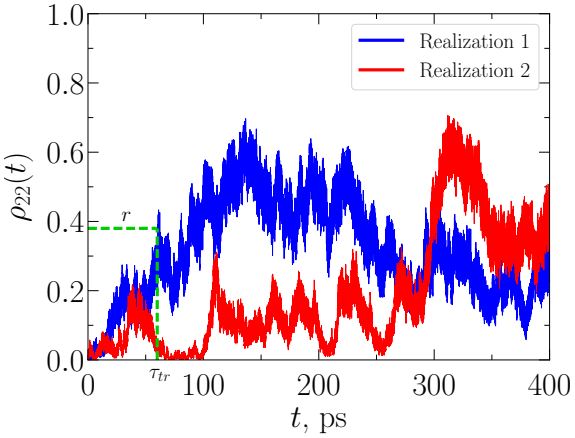

Fig. 2.1. Two different realizations of population dynamics of the two-site system. Green lines illustrate the procedure of the excitation transfer time calculation.

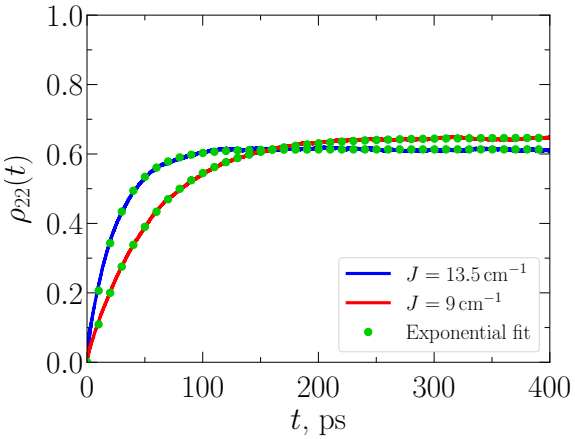

Fig. 2.2. Averaged populations of the two-site system calculated with different values of the inter-site coupling J_{12}.

the Fermi Golden Rule approach which states that populations have an exponential form, namely $\rho_{22}(t) = A\left(1 - \mathrm{e}^{-\frac{t}{\tau}}\right)$ with $A = k_{1\to2}/(k_{1\to2} + k_{2\to1})$ and $\tau = 1/(k_{1\to2} + k_{2\to1})$. Here $k_{1\to2}$ and $k_{2\to1}$ are the population transfer rates from the site 1 to site 2 and vice-versa, respectively. According to the Fermi Golden Rule these rates must be proportional to the square of the inter-site coupling J. To test this in Fig. 2.2 the curves obtained using the stochastic Schrödinger equation are fitted with the exponential function of the FGR and the transfer rates $k_{1\to2} = A/\tau$ and $k_{2\to1} = (1 - A)/\tau$ are calculated from the fitting parameters A, τ. For the blue curve we obtain $A_b = 0.62$ and $\tau_b = 24\,\mathrm{ps}$ and for the red curve we have $A_r = 0.65$, $\tau_r = 54\,\mathrm{ps}$. Calculating the ratio $(A_b\tau_r)/(A_r\tau_b)$ we obtain ≈ 2.15 which is in good agreement with the value $J_{12,r}^2/J_{12,b}^2 = 2.25$. Hence in the weak inter-site coupling limit, the stochastic Schrödinger equation is consistent with the Fermi Golden Rule.

The corresponding distribution of excitation transfer time from site 1 to 2 in the weakly coupled two-site system with parameters is presented in Fig. 2.3. As the Fermi Golden Rule holds in this case, we find proper exponential distribution of transfer times. The mean values of the transfer time indeed correspond to the inverse transfer rates, determined from population evolution in Fig. 2.2: for $J = 13.5\,\mathrm{cm}^{-1}$ and $J = 9\,\mathrm{cm}^{-1}$ we get $\tau_{1\to2} = 19.8\,\mathrm{ps}$ and $\tau_{1\to2} = 40.2\,\mathrm{ps}$, respectively.

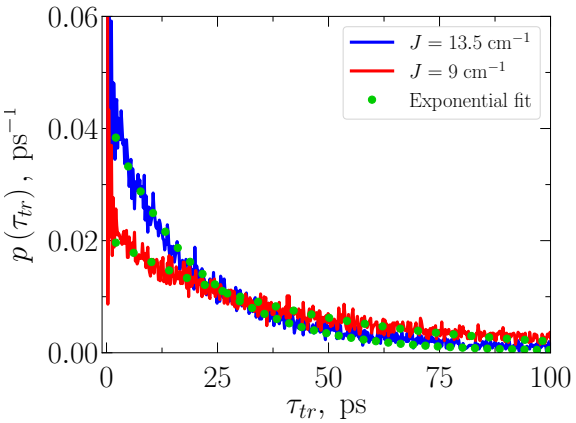

Fig. 2.3. Probability density functions of the transfer time τ_{tr} from the initially occupied state to the unoccupied state in two-site systems with different coupling J between the states. Parameters of the Debye spectral density are: $\lambda = 2\,\mathrm{cm}^{-1}$, $\omega_\mathrm{D} = 10\,\mathrm{fs}^{-1}$.

We must notice that the transfer time distributions in Fig. 2.3 contain a sharp rise at short times which is not accounted by the probabilistic theory of Markovian processes. This rise is the result of transient processes caused by slight non-Markovianity of the bath at short times originating from the finite-time correlation function for the environmental fluctuations. In our case the correlation time of the environment fluctuations is 10 fs. This initial rise corresponds to this time. In the ideal Markovian case, the fluctuation would be infinitely fast (white noise) and the initial rise and transition into the exponential function would happen at infinitesimal time interval.

We next consider the intermediate-to-strong coupling regime. Again we study the two-site system, but now we choose model parameters for intermediate couplings $J_{12} = 100\,\mathrm{cm}^{-1}$. For the environment, we choose the same Debye spectral density but increase both the reorganization energy $\lambda = 100\,\mathrm{cm}^{-1}$ and the bath fluctuations' correlation time $\omega_D = 100\,\mathrm{fs}^{-1}$ and study relaxation at two temperatures ($T = 300\,\mathrm{K}$ and $T = 77\,\mathrm{K}$). The initial condition is $\left|\psi\left(0\right)\right\rangle = \left|1\right\rangle$. The population of the second site is presented in Fig. 2.4* where the system's evolution is calculated with stochastic Schrödinger equation, time-dependent Redfield and HEOM methods. We can see that at both temperatures, the population rises very quickly in the first 100 fs and then performs oscillatory motion until it reaches the equilibrium value. It should be noted that in case of higher temperature the amplitude of the population oscillations is smaller and they are damped quicker ($\sim 0.3\,\mathrm{ps}$) than in the case of low temperature when oscillations die out after $\sim 0.5\,\mathrm{ps}$. The oscillations are mostly Rabi beats due to coupling J_{12} and non-stationary initial state. The damping is due to the coupling with the bath. It has been discussed in Section 1.2 that the approximate Redfield theory is not appropriate for such system, since the relaxation rates and consequently the excitation transfer times cannot be accurately defined [44]. It is easily seen in Fig. 2.4 that the Redfield theory result shows large deviations from the SSE calculation. However, as both are approximate,

*HEOM and Redfield calculations performed by A. Gelzinis, Vilnius University.

the provided information is not sufficient to judge about their correctness. Therefore we additionally present population dynamics calculated using the exact HEOM method. We can see that all methods give results that coincide perfectly at the very beginning of the simulation. We can also notice that the equilibrium values of the populations at $T = 300\,\mathrm{K}$ calculated with the SSE agree well with those obtained with the HEOM and Redfield methods. It is evident that the Redfield method gives largest errors at short times at $T = 300\,\mathrm{K}$ and overestimates the value of the population at $T = 77\,\mathrm{K}$. At low temperature there are moderate deviations between HEOM and SSE however, the results of the stochastic method qualitatively reproduce the character of the HEOM dependencies from short to intermediate times when transient processes are still present in the system.

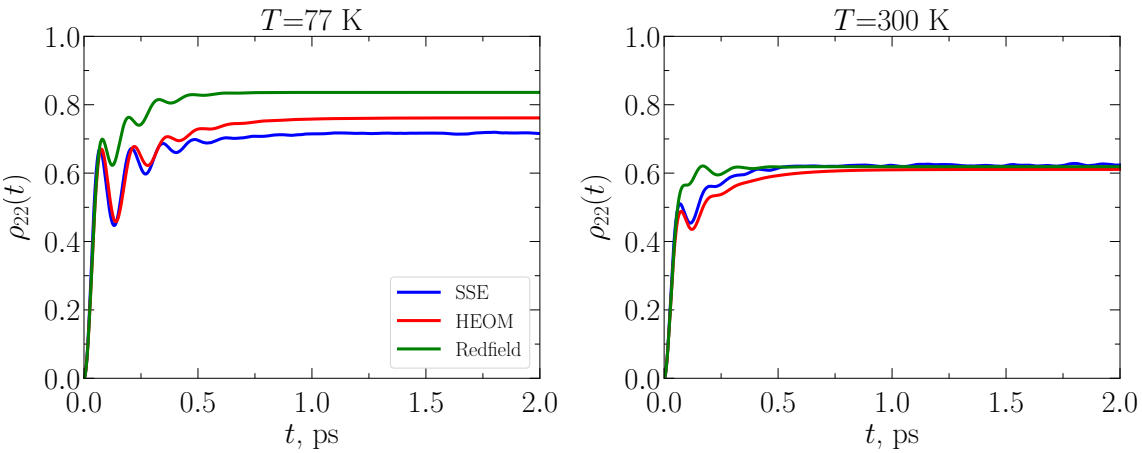

Fig. 2.4. Comparison of the population $\rho_{22}(t)$ evolution calculated with SSE, HEOM and Redfield methods.

The dynamics of the two-site strong-coupling system with the above-given parameters and heat bath characteristics should be rather non-Markovian due to the long decay time of the bath correlation function (100 fs) and this behavior must be reflected in the distributions of the excitation transfer time. These distributions are presented in Fig. 2.5. Comparing these results with distributions obtained for the weakly interacting Markovian system (Fig. 2.3), we clearly see that now the distributions are not exponential which indicates the significance of non-Markovian effects in this two-site system. The second peak in the transfer time distribution is a sign of the coherent components. We can notice that the duration of the initial rise of the probability density functions corresponds to the relaxation time of the heat bath ($\omega_\mathrm{D} = 100\,\mathrm{fs}^{-1}$). Such non-exponential distributions do not correspond to any process described by simple constant-rate equations, which define the transfer mean times. Thus, in this respect, the stochastic Schrödinger equation approach has an advantage in describing energy transfer over the density matrix approaches.

The process of transition time measurement described above closely resembles a

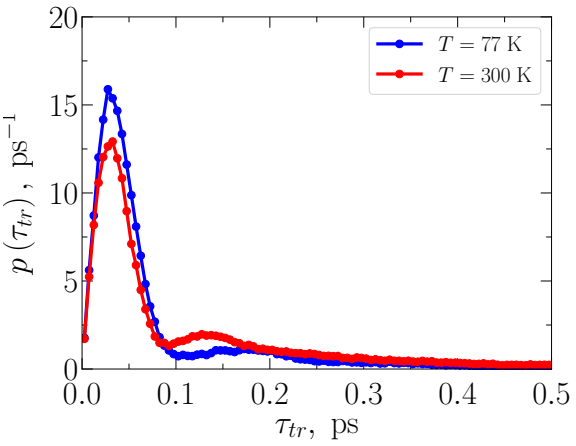

Fig. 2.5. Probability density functions of the transfer time τ_{tr} from the initially occupied state to the unoccupied state in the two-site system at different bath temperatures $T = 77\,\mathrm{K}$ and $T = 300\,\mathrm{K}$. Parameters of the Debye spectral density are: $\lambda = 100\,\mathrm{cm}^{-1}$, $\omega_\mathrm{D} = 100\,\mathrm{fs}^{-1}$.

quantum measurement of the system state with the N-slit-like measurement device in analogy with the two-slit experiment: the stochastic populations of the system represent the probabilities to find the excitation on a particular site and the random number r models the operation of the excitation detector at one of the "slits" [45]. The adequacy of this procedure of excitation transfer time calculation is clearly illustrated in Fig. 2.3 by applying this method to a two level system interacting with a nearly Markovian heat bath [12].

2.4.4 Application of the HSSE to a toy system

For investigating the hierarchical stochastic Schrödinger equations of different levels we calculate the dynamics of the simple model 2-site system with the same Hamiltonian as that used for calculations in Fig. 2.4. Initially only the higher energy site is populated. In Figs. 2.6 and 2.7 we present the dynamics of population of the other site, $\rho_{22}(t)$, of the model system calculated with Debye (2.37) and super-ohmic (2.38) spectral densities respectively. Here we show the results of calculations using the 2- and 1-level HSSEs, the latter being equivalent to the weak coupling SSE (2.48). The 2-level HSSE is solved by first reducing it from a system of coupled equations to a single effective equation as outlined in Subsection 2.3.1. In order to simulate various regimes of the system's evolution we choose different values of the system–bath coupling and the bath fluctuation correlation time. It should be noted that the fluctuations for HSSE are generated using the second method for obtaining noise realizations described in Subsection 2.4.1.

Both 1- and 2-level hierarchical stochastic Schrödinger equations are approximate, thus for benchmarking purpose we use the HEOM approach which is formally exact for systems linearly coupled to the bath where fluctuations are characterized by exponential correlation functions. Brownian oscillator (Debye) spectral density bath satisfies this requirement, in contrast with super-ohmic spectral density, thus

we only present HEOM reference curves in Fig. 2.6[†].

Calculations with Debye spectral density in Fig. 2.6 show little difference between HEOM and both versions of hierarchical stochastic Schrödinger equation in cases when system–bath interaction is $\lambda = 10\,\mathrm{cm}^{-1}$. However, when the coupling is increased to $\lambda = 100\,\mathrm{cm}^{-1}$ we notice that the effective 1-level stochastic Schrödinger equation shows slightly faster dynamics for the fast environment fluctuation case with $\omega_\mathrm{D} = 10\,\mathrm{fs}^{-1}$. For the last set of parameters, $\lambda = 100\,\mathrm{cm}^{-1}$ and $\omega_\mathrm{D} = 100\,\mathrm{fs}^{-1}$, during the first 400 fs the 1-level hierarchical stochastic Schrödinger equation closely follows the HEOM.

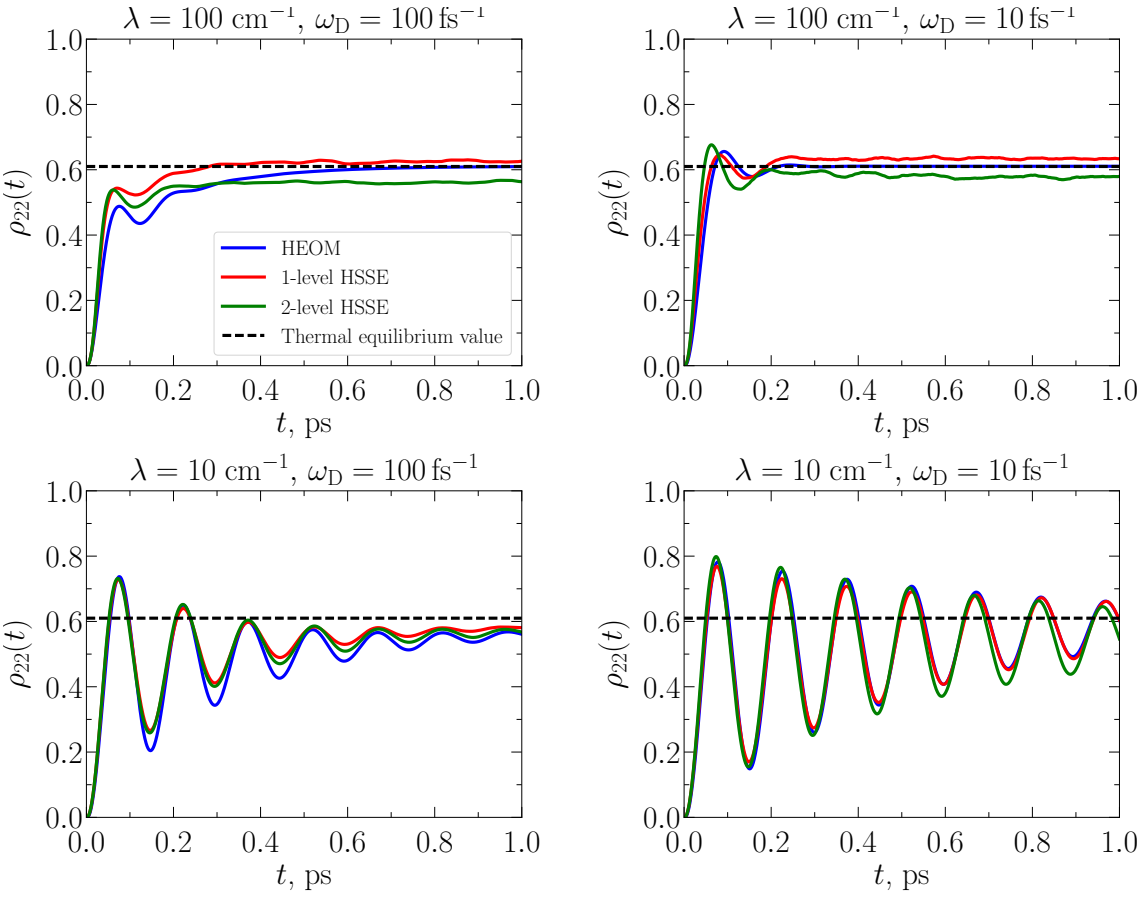

Fig. 2.6. Comparison of the population $\rho_{22}(t)$ evolution calculated with ordinary and hierarchical stochastic Schrödinger equation and HEOM methods using the Debye spectral density. Thermal equilibrium values were calculated using a method based on stochastic unraveling of influence functional in imaginary-time path integral formalism [46].

Results of calculations performed using the super-ohmic ($s = 3$) spectral density are depicted in Fig. 2.7. Here we see that similarly to the results presented in Fig. 2.6 the parameter sets with weak coupling produce curves matching each other with both versions of the hierarchical stochastic Schrödinger equation. However, the dy-

[†]HEOM calculations performed by A. Gelzinis, Vilnius University.

namics with $\lambda = 100\,\mathrm{cm}^{-1}$ and $\omega_{\mathrm{SO}} = 10\ \mathrm{fs}^{-1}$ is quite different when calculating with the 1-level HSSE and 2-level HSSE. The 2-level HSSE shows modulation of frequency for parameters $\lambda = 100\,\mathrm{cm}^{-1}$ and $\omega_{\mathrm{SO}} = 10\ \mathrm{fs}^{-1}$), reminiscent to polaronic feedback process of the system onto the bath. In the last case with strong coupling and slow bath ($\lambda = 100\ \mathrm{cm}^{-1}$ and $\omega_{\mathrm{SO}} = 100\,\mathrm{fs}^{-1}$) the equilibrium value is closer to 2-level HSSE.

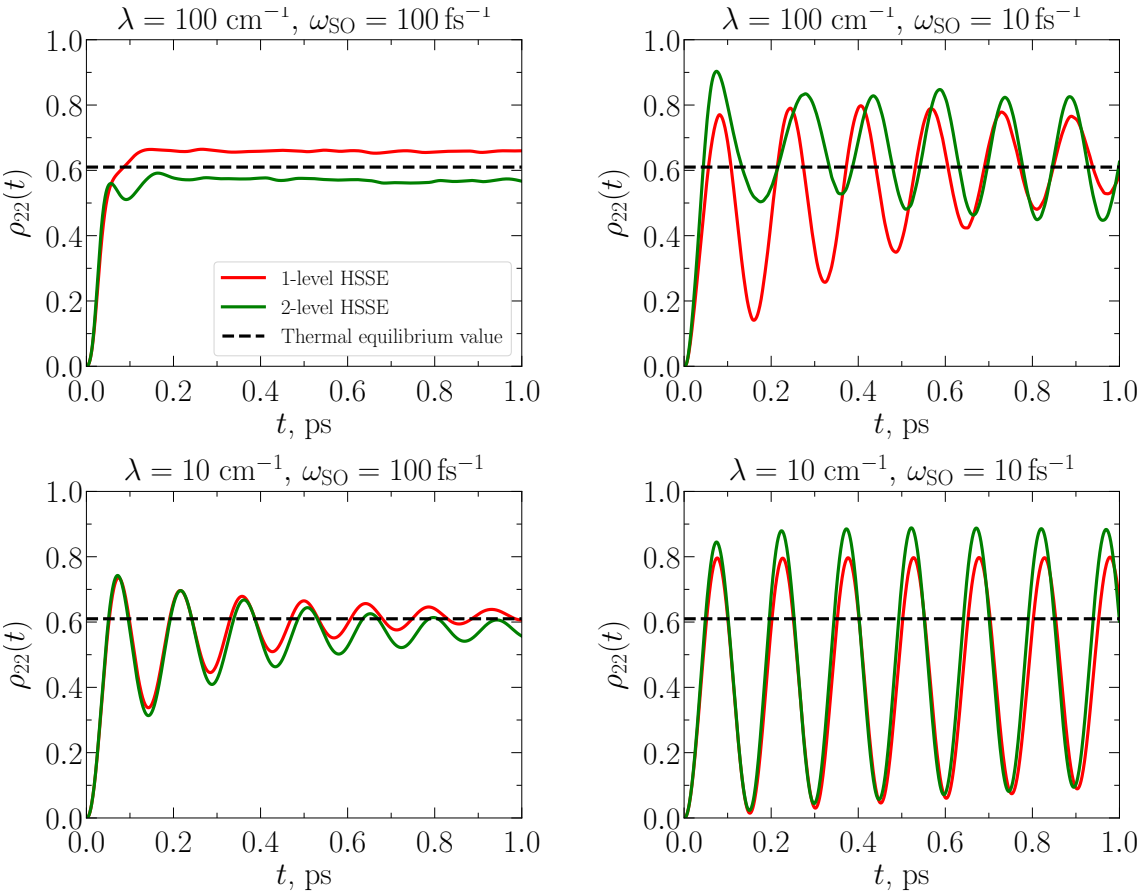

Fig. 2.7. Comparison of the population $\rho_{22}(t)$ evolution calculated with ordinary and hierarchical stochastic Schrödinger equation methods using the super-ohmic spectral density.

Hierarchy (2.55) can be compared to a number of other approaches based on solving a single or a system of coupled stochastic differential equations. One possible form of the stochastic equation for calculating the evolution of the reduced system was proposed by Peskin and Steinberg [47]. Their method relies on the assumption that the system–bath interaction is so small that the wavefunction of the global system can be factorized into system and bath wavefunctions and then the trajectories of the environmental oscillators can be approximated by their classical analogues. Due to this fact the noise driving the system evolution is purely classical, thus the method works well only in the high-temperature regime when the quantum effects of the bath lose their importance. In contrast, all forms of our ordinary and hierar-

chical stochastic Schrödinger equations are completely quantum approaches which account for all quantum effects in the bath with the only approximation applied to the SSE (2.47) in order to obtain the easier to calculate weak-coupling version.

A direct analogue of the system of equations (2.55) is the Hierarchy of Pure States (HOPS) method developed by Suess et al [48]. HOPS is obtained in a similar fashion to our hierarchy only the starting point of the derivation is Eq. (2.19) and not Eq. (2.43) as it is in our case. Hierarchical structure of the HOPS is obtained by defining auxiliary wavefunctions equal to the integral term of the SSE (2.19). However, to maintain the form of the time derivative of the auxiliary wavefunction similar for all levels of the hierarchy the correlation function which enters the integral in the original stochastic equation must have an exponential form. In order to use more complicated correlation functions one would need to resort to Pade decomposition mimicking the original functional form with a sum of complex exponentials. Such extension of the allowed forms of HOPS correlation function might not be sufficient in many cases where the experimentally measured correlation function of the environmental fluctuations is intended for use in numerical modeling. Our hierarchy (2.55) does not have any limitation on the form of the correlation function or the spectral density of the bath. However, compared to HOPS the directly calculating the hierarchical stochastic Schrödinger equation requires additional noises driving the stochastic equations for the auxiliary wavevectors which then have to be statistically averaged over many realizations of these fluctuations. Such a scheme is very demanding computationally and due to averaging over many Gaussian fluctuations the convergence is slow. The convergence issue is also present when solving the hierarchical stochastic Schrödinger equation using the method described in Subsection 2.3.1. Despite this fact we can see from Figs. 2.6 and 2.7 that already the 1-level and 2-level hierarchy produces good agreement with the formally exact HEOM and the asymptotic thermal equilibrium value so the proposed set of stochastic Schrödinger equations form a promising and solid background for further developments of approximations.

2.5 Conclusions

In Chapter 2 we derived the exact and approximate expressions of the stochastic Schrödinger equation and its hierarchical form. We calculated the dynamics of a two-site system with both stochastic Schrödinger equation and its hierarchical form and by comparing the results with the data obtained using other theoretical approaches we can state that **the stochastic Schrödinger equation is a versatile tool for modeling the dynamics of open quantum systems applicable in a wide range of parameter values. Its hierarchical form can be used to solve the**

formally exact stochastic Schrödinger equation to an arbitrary accuracy and approach the formally exact result. It is the **first** statement of this thesis.

Chapter 3

Energy transport in photosynthetic Fenna–Matthews–Olson complex

In this chapter we apply the weak-coupling stochastic Schrödinger equation (2.48) to investigate the dynamics of the photosynthetic Fenna–Matthews–Olson complex. Its quantum mechanical model is presented in Section 3.1 and the excitation transfer evolution is discussed in Section 3.2.

3.1 FMO model [P3]

Recent 2D spectroscopy studies of photosynthetic pigment-protein complexes [49,50] have shown the evidence of coherent dynamics which may play a role in energy transfer processes. These results sparked numerous debates whether the coherent system dynamics are related to the observed high efficiency and speed of the excitation energy transfer in such systems [51–56]. Persistence of the coherent beats over picosecond and their robustness contradict with predictions using conventional exciton relaxation theory based on Markovian Redfield equation [57, 58]. Possible vibronic contribution into some of these beats has been proposed in a number of recent studies resulting in complex behavior of the excitonic/vibronic 2D spectra [59–61]. Although long lasting beats in photosynthetic complexes reported by Raman spectroscopy measurements are well known for a long time [62], the Raman experiments only provide information about the molecular ground state. However, the coherent beats observed by 2D spectroscopy have contributions from the electronic excited states and hence the origin of the beats becomes obscure even in a such well studied photosynthetic complex as Fenna–Matthews–Olson (FMO) [60,63,64]. A number of experiments and theoretical studies has been recently accomplished to disentangle the electronic/vibrational origin of these beats in simple systems [65–67].

FMO complex found in the green sulfur bacteria is the first pigment-protein which had its structure revealed using the method of x-ray crystallography, hence it is one of

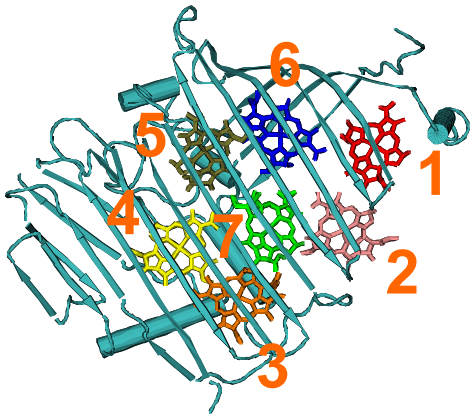

Fig. 3.1. Arrangement of the bacteriochlorophylls in one monomer of the FMO complex.

Table 3.1. Matrix elements of the FMO Hamiltonian given in cm^{-1}. Sites are numbered according to the crystallographic nomenclature [70].

	1	2	3	4	5	6	7
1	280	-106	0	0	0	-4	-4
2		420	28	0	0	13	0
3			0	-62	0	0	17
4				175	-70	-19	-57
5					320	40	-2
6						360	32
7							260

the best studied photosynthetic aggregates [49, 50, 63, 68]. FMO complex is a trimer consisting of 3 identical monomers which are formed from 8 bacteriochlorophyll (BChl) molecules supported by a rigid protein carcass (Fig. 3.1). In green sulfur bacteria, the FMO aggregate acts as a molecular wire which transports the excitation energy from the light-harvesting chlorosomes to the reaction centers of the I type located in the membrane [49, 50, 68]. We next apply the SSE theory to study the energy transfer dynamics in the FMO aggregate [69].

We assume that the FMO system consists only of 7 sites corresponding to different BChl molecules. The 8th molecule is not taken into account due to its weak coupling with the rest of the BChls. Setting the energy of the 3rd site, through which the energy excitation travels to the reaction center, to zero, we obtain the Hamiltonian matrix presented in Table 3.1 [68]. In all simulations of the FMO system, the initial state was chosen to be the superposition $\left|\psi\left(0\right)\right\rangle = \frac{1}{\sqrt{2}}\left(\left|1\right\rangle + \left|6\right\rangle\right)$. This state is chosen because the 1st and the 6th BChl molecules are nearest to the light-harvesting chlorosomes where the excitation is created [68]. The interaction with the environment induces fluctuations of the excitation energies of the BChl molecules.

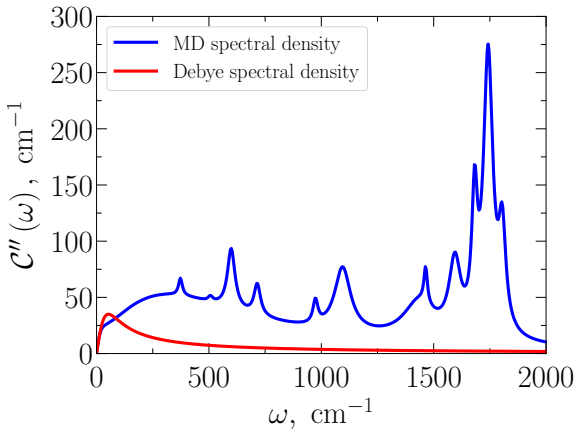

Fig. 3.2. MD and Debye spectral densities used for the FMO complex. Parameters of the Debye spectral density are: $\lambda = 35\,\mathrm{cm}^{-1}$, $\omega_\mathrm{D} = 100\,\mathrm{fs}^{-1}$ [72].

Classical correlation functions of these energy fluctuations for every BChl molecule have been estimated by the Olbrich *et al.* molecular dynamics (MD) simulations of the whole FMO complex in the solution [71]. These correlation functions have been approximated by a combination of exponents and decaying oscillations. After performing the Fourier transformation, the spectral density of the n-th BChl molecule at room temperature ($T = 300\,\mathrm{K}$) is given by the expression

$$\mathcal{C}''_{\mathrm{MD},n}(\omega) = \frac{2}{\pi}\tanh\left(\frac{\beta_T\omega}{2}\right)\left(\sum_{m=1}^{N_0}\frac{\eta_{nm}\gamma_{nm}}{\gamma_{nm}^2+\omega^2} + \frac{1}{2}\sum_{m=1}^{N_0}\frac{\tilde{\eta}_{nm}\tilde{\gamma}_{nm}}{\tilde{\gamma}_{nm}^2+\left(\omega-\tilde{\omega}_{nm}\right)^2}\right). \tag{3.1}$$

Here η_{nm}, γ_{nm}, $\tilde{\eta}_{nm}$, $\tilde{\gamma}_{nm}$ and $\tilde{\omega}_{nm}$ are parameters obtained from fitting the corresponding correlation functions and N_0 is the number of terms in the sum. In this expression, the hyperbolic tangent factor is introduced to take into account the temperature dependence of the parameters. We denote this spectral density as the MD spectral density.

The MD spectral density in Eq. (3.1) consists of two terms. The first is a Debye term determining the overdamped low frequency modes. The second part reflects the high-frequency modes. These should be associated with the intra-molecular vibrations. As the intra-molecular vibrational frequencies are the same for all chrorophylls, while their amplitudes vary from site to site, for simplicity we assume the averaged spectral density for all BChl molecules with $N_0 = 12$ terms in Eq. (3.1). As a reference, we use the Debye spectral density (Eq. (2.37)) without high frequency intra-molecular vibrations. Both Debye and MD spectral densities have similar low-frequency parts, while they are different at high frequencies as shown in Fig. 3.2. The low frequency part also corresponds to the experimentally determined spectral density in this range of frequencies.

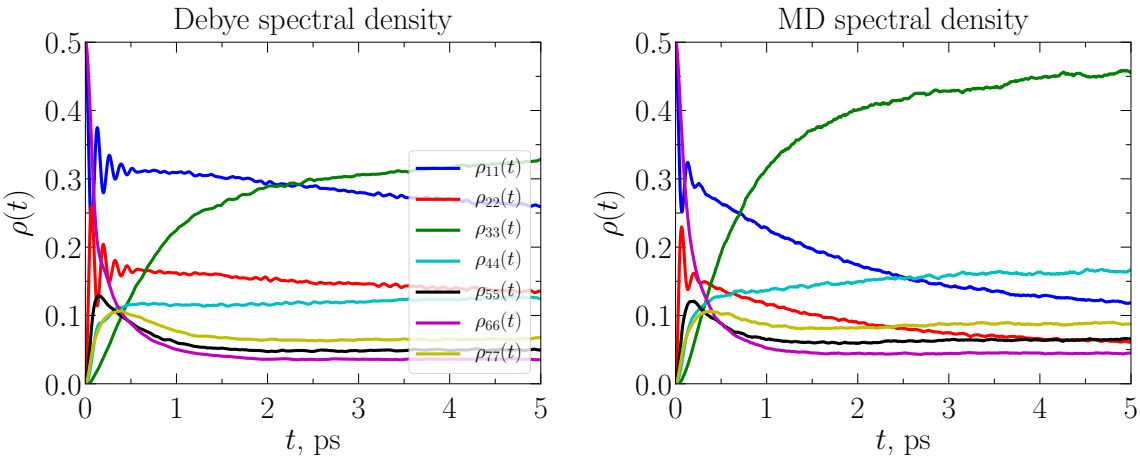

Fig. 3.3. Populations of the FMO system calculated in the site basis. Debye spectral density parameters are $\lambda = 35\,\mathrm{cm}^{-1}$ and $\omega_\mathrm{D} = 100\,\mathrm{fs}^{-1}$.

3.2 Energy transport through FMO [P3]

The dynamics and relaxation of the excitation in the FMO aggregate can be investigated by first analyzing the evolution of the site populations. They are averaged over the ensemble according to Eq. (2.70) at the temperature $T = 300\,\mathrm{K}$ and are presented in Fig. 3.3. Here calculations with both spectral densities indicate that when the system approaches equilibrium the value of the population $\rho_{33}(t)$, corresponding to the site with the lowest energy $\epsilon_3 = 0$, becomes the largest in accord with previous simulations [73]. Equilibrium values of other sites' populations are also ordered in accord with their energy corresponding to proper thermal equilibrium. From the populations' dynamics calculated with Debye spectral density we can see that despite $\rho_{44}(t)$, $\rho_{55}(t)$, $\rho_{66}(t)$, and $\rho_{77}(t)$ reaching equilibrium after $\sim 2\,\mathrm{ps}$, other curves are still not stationary, thus the full relaxation of the system occurs in more than 5 ps. The results obtained with MD spectral density demonstrate qualitatively similar but slightly quicker relaxation process. The coherent evolution as well as delocalized excitons in the system can be recognized from the oscillations of the presented populations. From the calculations with Debye spectral density, we can see that oscillations decay after $\sim 500\,\mathrm{fs}$. Using MD spectral density we obtain smaller amplitudes of oscillations and they decay faster – after $\sim 300\,\mathrm{fs}$. This damping is the manifestation of the electronic coherences' decay. Hence the MD spectral density seems to slightly speed-up the relaxation dynamics without noticeable qualitative differences.

In Subsection 2.4.2 we developed the algorithm to obtain the probability distribution of the transition time between two states of the system using the stochastic Schrödinger equation. We applied this method to obtain the distributions of the transfer time from the initial state of the FMO to the seven states corresponding

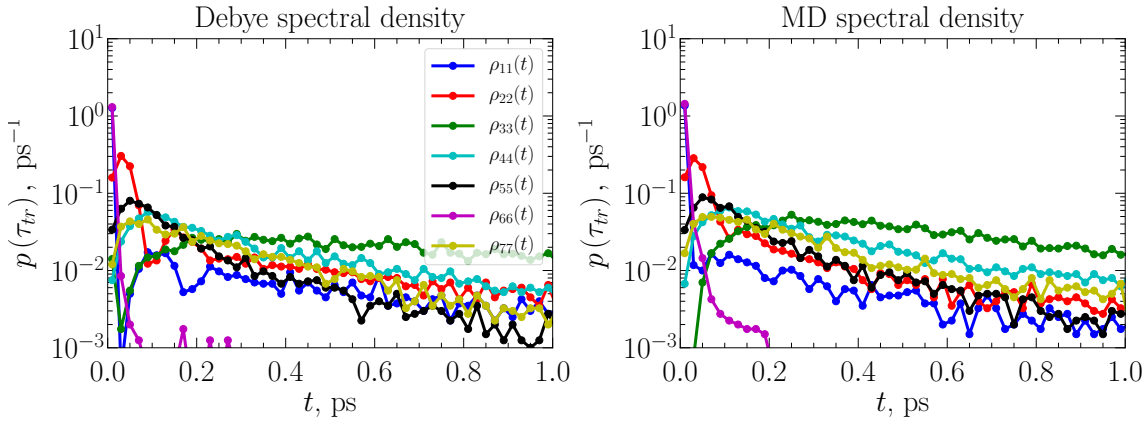

Fig. 3.4. Distributions of energy excitation transfer time calculated for all sites of the system. Debye spectral density paramters are $\lambda = 35\,\mathrm{cm}^{-1}$ and $\omega_\mathrm{D} = 100\,\mathrm{fs}^{-1}$.

to excitation localized on different BChl molecules. Calculations presented in Fig. 3.4 were performed with both Debye and MD spectral densities. It is evident that due to transient processes in the system initial parts of all distributions calculated with both spectral densities exhibit non-exponential form which in the log-linear scale should manifest as a set of linear dependencies. We can notice that with both spectral densities we obtain similar overall arrangement of the excitation transfer time distribution curves and also the most probable transfer times. It is obvious that the energy excitation can be registered at the 1st or the 6th site in the shortest time. Analyzing the positions of the maxima of the probability distributions we can see that the excitation travels through the FMO complex in such order: 2nd site, 5th site, 7th site, 4th site, and it takes the longest time for the excitation to arrive at the 3rd site. Hence, the transfer time distributions reveal the excitation transfer pathways in multi-site excitonic systems. From the Fig. 3.4, we can also see that the transfer time distribution at the 3rd site is the broadest, which means that in this case the time τ_{tr} has the biggest uncertainty.

From the results of population dynamics in Fig. 3.3 and transfer time distributions in Fig. 3.4 we can draw the conclusion on the effect of intra-molecular high-frequency vibrations on the energy transfer dynamics in the photosynthetic FMO aggregate. 2D spectroscopy experiments revealed long-lasting quantum coherences in FMO and in a range of other systems [57, 74, 75]. There is a continuous debate on the origin of these beats, while their assignment recently was shifted to be vibrational. The role of the coherence is considered to be an important factor for defining the excitation dynamics in molecular aggregates. We hence addressed the very core of the problem and simulated the excitation transfer processes by including or excluding the high-frequency vibrations. As revealed by the distribution of the excitation transfer time to the 3rd FMO site shown in Fig. 3.5, the overall dynamics becomes slightly faster; however, the excitation transfer pathways are not

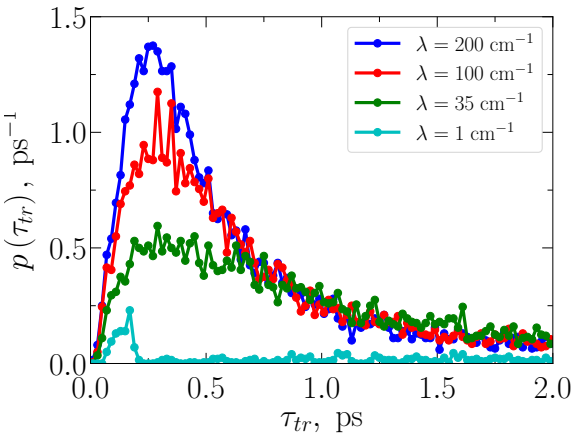

Fig. 3.5. Distributions of the excitation transfer time to the 3rd site in the FMO system calculated at different system–bath interaction strengths. Debye frequency is $\omega_D = 100\,\mathrm{fs}^{-1}$, temperature $T = 300\,\mathrm{K}$.

very sensitive to the choice of the spectral density, i.e., whether we have or do not have high frequency vibrational modes. It could be argued that the system–bath coupling strength parameters, the reorganization energies, of both spectral densities are different so the results do not have complete one-to-one correspondence. The reorganization energy includes contributions from both the low frequency and the high frequency components, so obviously the two models of spectral density cannot have the same reorganization energy. However, the low frequency parts of the spectral densities are comparable, so the effect on the transfer times is necessarily related to the high frequency spectral components.

3.3 Conclusion

In Chapter 3 we applied the stochastic Schrödinger equation to investigate the excitation energy transfer dynamics in the photosynthetic FMO complex. Using two different models for the bath spectral density (with and without high frequency modes) we calculate the evolution of the populations in the FMO system, as well as excitation transfer times distributions and reveal that **the excitation transport pathways in the FMO aggregate are not sensitive to high-frequency modes of the bath**. This is the **second** statement of the thesis.

Chapter 4

Charge transport in bulk heterojunction organic solar cells

This chapter is dedicated to studying charge separation dynamics in organic solar cells. In Section 4.1 we present an overview of the operating principles of organic solar cells and difficulties associated with theoretical description of charge dynamics in these devices. Later, in Section 4.2 we apply the stochastic Schrödinger equation to calculate the short-time evolution of the charge pair and in Section 4.3 we investigate the long-time charge separation dynamics using the Monte-Carlo method.

4.1 Charge generation mechanism [P2, P4, P5]

Organic solar cells (OSCs) in recent years have gained much attention as a possible cheaper alternative to photo-voltaic elements based on inorganic materials, e. g. silicon. However, the light conversion efficiency of OSCs was much lower compared to their inorganic counterparts. A major improvement in cell efficiency was obtained by the introduction of the bulk heterojunction device (BHJ) structure [76,77] consisting of a mesostructured blend film of conjugated polymer and fullerene. This structure is shown schematically in Fig. 4.1. Upon light absorption, excitons are produced in the polymer phase and are converted into closely bound electron–hole pairs at the polymer–fullerene interface, sometimes also referred to as charge transfer states. In an operating solar cell, these bound charge pair states have to dissociate by overcoming the mutual Coulomb attraction between electrons and holes, to form free mobile charges (charge-separated states) that can be extracted as photocurrent.

Electron-hole pairs split into nearly-free charge carriers on a femtosecond time scale and despite the strong Coulomb interaction between the charges this process is known to be often close to 100% efficient. However, to this day it is not completely clear what mechanism is responsible for efficient charge separation at organic heterojunctions. Several explanations were suggested for the initial dissociation stage,

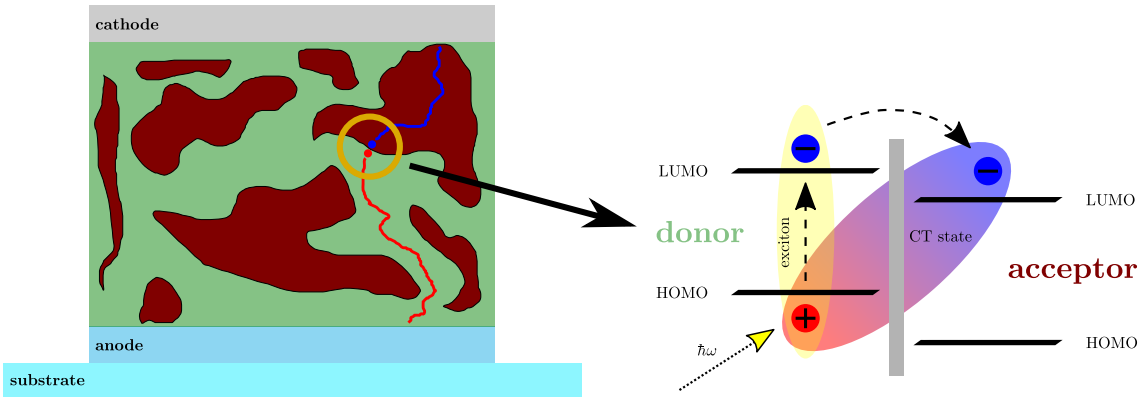

Fig. 4.1. Schematic representation of a bulk heterojunction OSC. The active layer consisting of donor (light green) and acceptor (maroon) materials is sandwitched between the transparent anode and metalic cathode. A photon excites a donor molecule forming a molecular exciton, then the excited electron is transfered to the acceptor molecule due to LUMO energy diference.

for example: charge carrier delocalization over several polymer segments and/or fullerene molecules [78], hot interfacial charge transfer states with delocalized wavefunctions [79,80] or, alternatively, with electron and/or hole wavefunctions localized on molecules situated at large distances from the interface [81]. Recently, a partially coherent model, assuming electron delocalization over the entire aggregated fullerene domain [82], and a hybrid model of a 1D polymer/fullerene lattice with semi-classical dynamics at short time scales and Redfield relaxation theory at long time scales [83], have been proposed. Consequently, charge separation on an ultrafast time scale is often considered to be predominantly coherent. However, carrier delocalization and coherent propagation, their extent and temporal evolution have only been qualitatively postulated. Although the later time scales of charge separation have been successfully described by incoherent hopping (see Section 4.3 for detailed discussion and calculations), a consistent model at the earliest time scales, describing the coherent propagation of charge and the gradual transition into the classical hopping regime, is still absent. As a consequence, the role of coherence remains elusive.

4.2 Short-time charge separation dynamics [P5]

To elucidate the role of delocalization and coherence in the initial stage of charge separation a full quantum mechanical description is necessary due to the non-equilibrium nature of such process. In this section we use the stochastic Schrödinger equation to describe the charge separation process by the principles of open quantum systems on the timescale from femtoseconds to several picoseconds. This approach allows us to evaluate the interplay between coherent dynamics and bath induced de-

phasing, and predict the importance of delocalization in systems with a wide range of inter-molecular couplings, leading to different charge separation scenarios [84].

4.2.1 Quantum mechanical model of the donor–acceptor interface

The acceptor medium together with a single donor site coupled to the bath of harmonic oscillators is described as a quantum system characterized by the Hamiltonian (2.1). Donor and acceptor sites are arranged into a cubic lattice with nearest-neighbor interactions between different sites, as shown in Fig. 4.2. We consider only single particle states $\left|n\right\rangle$ denoting the electron on the site n. The harmonic oscillator environment is described by the Debye model (2.37). The model is implemented on a 3D cubic lattice of $8\times16\times16$ sites and this size corresponds to the expected size of a PCBM aggregate in well-intermixed bulk heterojunction solar cells. Transmission electron microscopy images of P3TI:$PC_{71}BM$ indicate a well-intermixed morphology, in agreement with our assumption. In order to model photo-excitation in the donor phase, we initially place both the electron and the hole at the donor site. It has been recently experimentally demonstrated that mainly electron motion in PCBM is responsible for the initial evolution of the charge separation process – hole motion is significantly slower [82, 85, 86]. Therefore, in our treatment we consider the hole to be immobile, thus the donor site is merely the source of the electrostatic Coulomb field and the electron is described quantum mechanically using the stochastic Schrödinger equation. In this setup the charge transfer state is obtained when the electron is transferred from the donor to the neighboring acceptor site.

The variable size of acceptor aggregates and the overall complexity of interfaces in the hierarchical morphology of the bulk heterojunction blend does not allow straightforward simulation of its entire structure using the stochastic Schrödinger equation. In this case we reflect different morphologies by a variation of couplings between the acceptor sites.

Site energies ϵ_n in the Hamiltonian of the system (Eq. (2.1)) are given by

$$\epsilon_n = \begin{cases} \epsilon_{\mathrm{D}} + \delta_n, & n = 1 \\ \epsilon_{n,\mathrm{C}} + \epsilon_{n,F} + \delta_n, & n \neq 1 \end{cases} \tag{4.1}$$

Here ϵ_{D} is the electron self-energy on the donor site (it is the molecular excitation energy since the hole is localized on this site as well), while self-energies of the acceptor sites are set to zero, $\epsilon_{n,\mathrm{C}}$ is the Coulomb interaction energy between the hole and the electron, $\epsilon_{n,F}$ is the energy contribution due to some external electric field and δ_n – the contribution due to the static energetic disorder of electron energies in the lattice. δ_n is taken as a Gaussian random number, characterized by the standard deviation σ, and all calculation results must be averaged over this parameter. In-

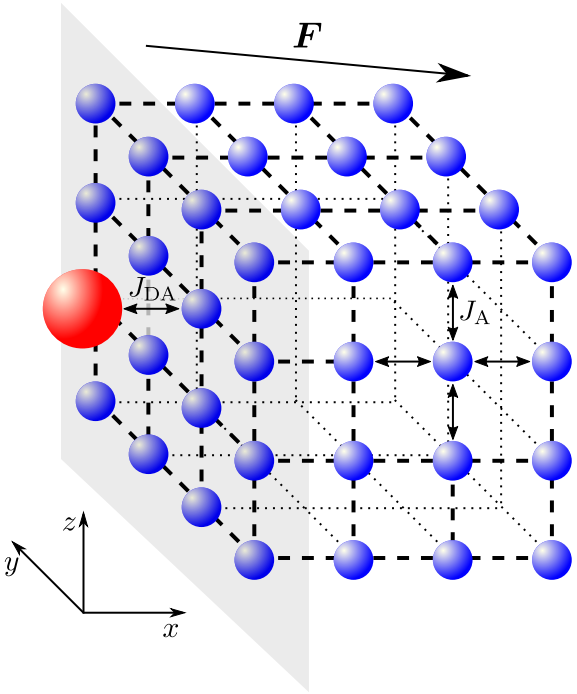

Fig. 4.2. Schematic of the donor–acceptor interface model. Red sphere denotes the donor site, blue spheres denote the acceptor sites, $\boldsymbol{F}$ denotes the arbitrary direction of the external electric field reflecting the random orientation of the donor–acceptor interface with respect to $\boldsymbol{F}$ (see the main text), J_{DA} and J_{A} denote the interaction energies between the donor and the nearest acceptor site and between the nearest neighbor acceptor sites respectively.

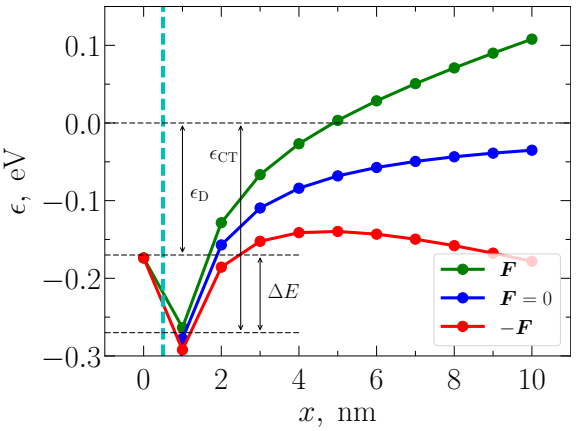

Fig. 4.3. Energy profile in the direction perpendicular to the donor–acceptor interface plane (dashed cyan line). The red and green curves represent the shift of the Coulomb potential due to the applied external electric field, the blue curve – the shifted Coulomb potential when a net zero electric field is applied. The donor site corresponds to $x = 0$. ϵ_{D} is the donor site excitation energy, ϵ_{CT} denotes the state energy of the CT exciton and ΔE is the driving force.

teraction energy J_{nm} in the system Hamiltonian is equal to J_{DA} if n and m denote the donor and the nearest-neighbor acceptor site, otherwise, $J_{nm} = J_{\mathrm{A}}$ if n and m denote nearest-neighbor acceptor sites.

Coulomb potential between the hole and the electron contribution from Eq. (4.1) has the form

$$\varepsilon_{n,\mathrm{C}} = -\frac{q^2}{4\pi\epsilon\epsilon_0\,(r_n + b)}, \tag{4.2}$$

where $|q|$ is the electron charge, ϵ_0 and ϵ are the dielectric constants of empty-space and of material, respectively, r_n is the distance between the n-th site of the lattice and the donor site, parameter b accounts for the finite size of the donor and acceptor molecules shifting up the CT exciton energy according to the experimentally

determined binding energy. The energy term $\epsilon_{n,F} = q\boldsymbol{F} \cdot \boldsymbol{r}_n$ is due to the external electric field $\boldsymbol{F}$. Using Eq. (4.1) and expressions for $\varepsilon_{n,\mathrm{C}}$ and $\varepsilon_{n,F}$ we can visualize the energy profile in the x direction, perpendicular to the donor–acceptor interface as presented in Fig. 4.2. Here, the energy profile is given for three different cases: when the external electric field is applied perpendicular to the donor–acceptor interface (with negative values of F pointing from the acceptor to the donor phase), in the opposite direction (positive F values) and with no external electric field.

The main quantities we use to investigate the charge separation dynamics in our model are the site populations (electron probability density) calculated with Eq. (2.70) and the absolute electron–hole separation distance given by

$$d_{\mathrm{abs}}(t) = \left\langle \sum_n r_n \psi_n^*(t)\, \psi_n(t) \right\rangle_{\mathrm{ens}} . \tag{4.3}$$

Using this expression we can calculate the ensemble-averaged value of the absolute electron–hole separation distance, however, the stochastic Schrödinger equation formalism allows access to the stochastic and probabilistic parameters of the quantum observable, as described in Section 2.4. Using this property of the SSE we can construct the probability density distribution $p_t\left(d'_{\mathrm{abs}}\right)$ of the absolute charge separation distance at some particular time t. The average absolute separation distance (4.3) is then given by $d_{\mathrm{abs}}(t) = \int \mathrm{d}d'_{\mathrm{abs}} p_t\left(d'_{\mathrm{abs}}\right) d'_{\mathrm{abs}}(t)$ where d'_{abs} is the value of the absolute separation distance obtained from a single realization.

Since we are interested to study coherent effects at the very beginning of the charge separation process we require a numerical measure to quantitatively describe the degree of coherence present in the system. For this task we introduce introduce the average coherence radius of the electron

$$R_e(t) = \frac{a}{2} \sqrt[3]{\sum_{n \neq m} \left\langle \left| \psi_n^*(t)\, \psi_m(t) \right| \right\rangle_{\mathrm{ens}}} \tag{4.4}$$

which denotes the linear extent of delocalization. Here a is the lattice constant. The main building block of the definition (4.4) is the sum of the density matrix off-diagonal components' absolute values [87]. Values of the parameter $R_e(t)$ are bounded by two limiting cases of the electronic wave vector: when the system is either completely coherent or incoherent. In the fully coherent case all N components of the wave vector $\psi_n(t) = \frac{1}{\sqrt{N}}$ are equal, thus the coherence radius is at its maximum with $R_e(t) = \frac{a}{2}\sqrt[3]{(N-1)}$. When the system is completely incoherent it means that its state must be described by a statistical mixture of fully localized electronic states which all have equal probabilities of $\frac{1}{N}$, thus the reduced density of the system only has diagonal components and the off-diagonal elements are zero.

In this case the extent of electron's delocalization (4.4) is zero as well.

Previously introduced observables are difficult or even impossible to measure experimentally, hence for checking our simulation results with experimental data we calculate the electron-hole drift separation distance

$$d_F(t) = \left\langle \sum_n \psi_n^*(t)\,\psi_n(t)\,\boldsymbol{r}_n \cdot \frac{\boldsymbol{F}}{|\boldsymbol{F}|} \right\rangle_{\text{ens}} \tag{4.5}$$

along the direction of the applied external electric field. Using the calculated drift distance we are also able to estimate the electron mobility

$$\mu(t) = \frac{\mathrm{d}}{\mathrm{d}t}\frac{d_F(t)}{F}. \tag{4.6}$$

4.2.2 Simulation results and comparison with the experiment

The donor–acceptor interface is characterized by the lattice constant a, the molecular dimension parameter b (in the Coulomb potential expression (4.2)), the interaction energies between sites J_{DA} and J_{A}, the donor site excitation energy ϵ_{D}, the site energy disorder σ and the system–bath coupling strength λ. In addition, the overall size of the lattice could be variable due to the complexity of interfacial domains at hierarchical morphologies of the blend. We assume that differences in morphologies are mostly reflected by a variation of couplings between the acceptor sites. Simulation parameters were chosen as those typical for polymer–PCBM systems: driving force $\Delta E = 0.1\,\text{eV}$ for P3TI:PC_{71}BM, CT exciton binding energy $\epsilon_{\text{CT}} = -0.27\,\text{eV}$ and the energetic disorder σ of PCBM was set equal to $\sigma = 75\,\text{meV}$, corresponding to the experimentally determined value [88] and J_{DA} is set equal to $12.5\,\text{meV}$ leading to an electron transfer time of $100\,\text{fs}$, in agreement with experimental transient absorption data [84]. The lattice constant is equal to $1\,\text{nm}$. However, we point out that absolute values of these parameters, such as for example the energetic disorder of the PCBM phase, are model dependent. In order to determine the sensitivity of our simulations to different parameters, we have calculated the dynamics of the system by varying the parameters in the vicinity of the values given. For this investigation we used a smaller acceptor lattice of $8 \times 8 \times 8$ sites. Results are presented in Figs. 4.4. We find that the most important parameter governing the coherent dynamics ($< 500\,\text{fs}$) of the electron is the inter-acceptor coupling J_{A}. While the dynamics at later times ($> 500\,\text{fs}$) somewhat differ, they remain qualitatively the same within the range of parameter values reported by other studies. Hence, in later analysis we have kept all of the parameters fixed to those outlined above, except for the inter-acceptor coupling J_{A}, which was varied.

Fig. 4.5 shows the simulated temporal evolution of electron density for the in-

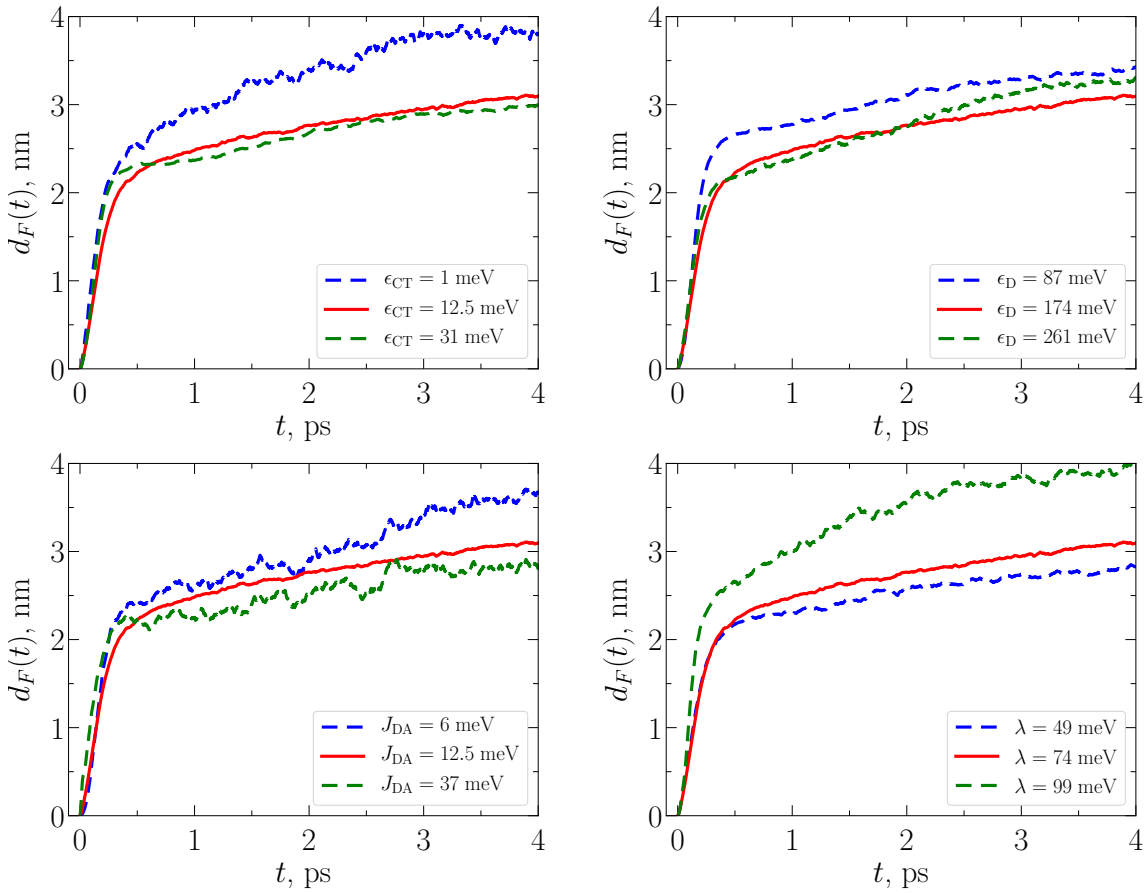

Fig. 4.4. Drift charge separation distance dynamics calculated for different values of CT state energy ϵ_{CT}, donor site excitation energy ϵ_D, donor–acceptor coupling strength J_{DA} and system–bath interaction energy λ. Strength of external electric field $\boldsymbol{F}$ is set to $5.7 \times 10^5\,\mathrm{V \cdot cm^{-1}}$.

dicated values of inter-acceptor electron coupling J_A. Data are projected in the plane perpendicular to the donor–acceptor interface. External electric field is not applied to highlight the effects of delocalization. Our results show that the electron is transferred from the donor site to a nearby pool of coherently coupled acceptor sites within $\sim 500\,\mathrm{fs}$. The number of accessible sites in a given time interval grows with increasing inter-acceptor coupling, allowing for the electron to be transferred to more distant sites already at very early times. Electron transfer is quantitatively characterized in the rightmost column of Fig. 4.5, where the kinetics of the absolute electron–hole separation distance, $d_{abs}\,(t)$ (Fig. 4.5, red curves) and the average electron coherence radius, $R_e\,(t)$ (Fig. 4.5, blue curves), are shown. The extent of electron delocalization is also visualized by the blue circles which are the graphical representations of the probability density distributions of the electron coherence radius (4.4). These results only weakly depend on the donor excitation energy ϵ_D, in agreement with experimental studies of charge separation efficiency versus excitation energy [89].

The kinetics of both $d_{abs}\,(t)$ and $R_e\,(t)$, for different J_A exhibit a similarly rapid

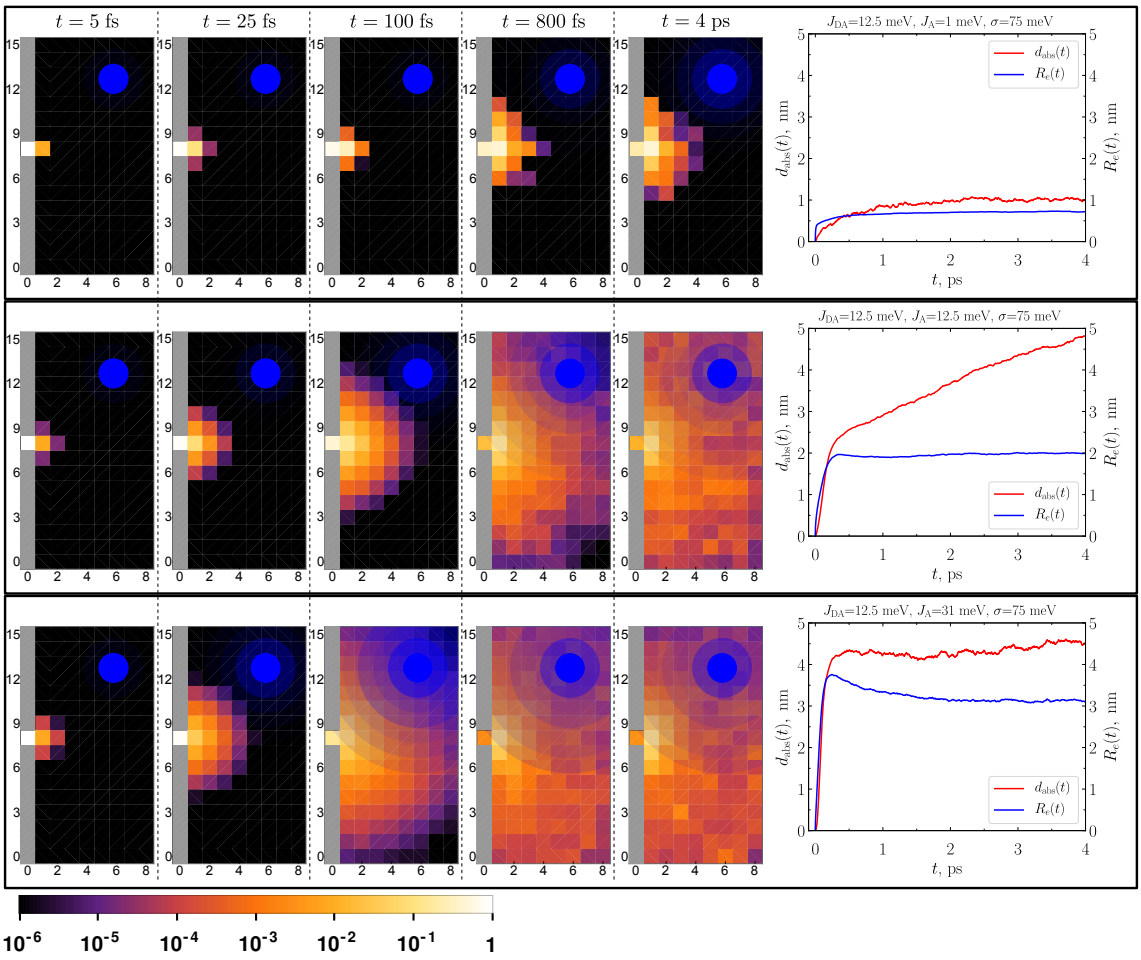

Fig. 4.5. Ensemble-averaged evolution of electron probability density in the plane perpendicular to the donor (gray area) and acceptor ($8 \times 16 \times 16\,\mathrm{nm}^3$ domain) interface at different times following photoexcitation for the indicated values of inter-acceptor coupling J_A. The rightmost column shows the corresponding absolute charge separation distance $d_\mathrm{abs}\,(t)$ and delocalization radius $R_e\,(t)$. Filled blue circles illustrate the extent of electron coherence at a given time. The color scale at the bottom describes the probability of finding the electron at the indicated distance from the interface.

initial rise. For very weak coupling both electron delocalization and initial electron transfer distance are small, and thus the electron is only transferred from the donor to the nearest acceptor site. For intermediate coupling the initial transfer distance is increased and the electron is more, although still weakly, delocalized. In this regime at later times $> 500\,\mathrm{fs}$ the average electron distance increases while its delocalization remains constant. In case of strong coupling, the electron is strongly delocalized, we thus observe the largest electron transfer distance at early times, whereas the later part of the transfer process is mainly determined by time-dependent localization. Note that for strong couplings electron delocalization is confined by the size of the acceptor lattice in our model, chosen to correspond to the expected PCBM domain size ($8 \times 16 \times 16\,\mathrm{nm}^3$) in efficient polymer–PCBM blends. Despite similar

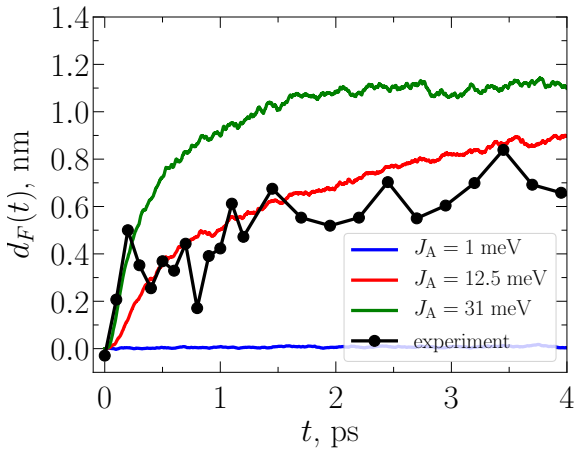

Fig. 4.6. Time dependence of the charge separation distance $d_F(t)$ along the direction of the electric field $\boldsymbol{F}$ of $5.7 \times 10^5\,\mathrm{V \cdot cm^{-1}}$ for the indicated inter-acceptor coupling values J_A.

probability distributions at long times in the second and third rows of Fig. 4.5, the extent of delocalization of individual electrons and, consequently, the character of their motion is very different with the dynamics in the strong coupling case being more wave-like.

To determine which regime corresponds to real polymer–PCBM blends, we have compared our model prediction to experimentally measured carrier drift dynamics probed by a recently developed experimental technique, time-resolved electric-field induced second harmonic generation (TREFISH), enabling ultrafast measurements [84, 90]. We have chosen a bulk heterojunction solar cell based on P3TI:$PC_{71}BM$. This system is of particular interest due its exceptionally low driving force $\Delta E \sim 0.1\,\mathrm{eV}$ for charge separation [91], nevertheless leading to an internal quantum efficiency (IQE) of 90%. Transient absorption spectroscopy also indicates ultrafast photo-induced charge transfer on a $< 100\,\mathrm{fs}$ time scale. Charge separation in P3TI:$PC_{71}BM$ is thus expected to rely on charge delocalization and coherent electron propagation.

Figure 4.6 shows the experimental and simulated average electron–hole separation along the direction of the electric field of $5.7 \times 10^5\,\mathrm{V \cdot cm^{-1}}$, created by applied voltage and the built-in field of the OSC contributing $0.7 \times 10^5\,\mathrm{V \cdot cm^{-1}}$. Transient absorption spectroscopy shows no signatures of delayed charge transfer due to exciton diffusion, only prompt photo-induced charge transfer at a time scale of $< 100\,\mathrm{fs}$. Thus, the experimental TREFISH data in Fig. 4.6* directly monitors the motion of the photo-induced electron away from the donor–acceptor interface. The experiment shows a fast $\sim 500\,\mathrm{fs}$ initial rise to a charge separation distance of 0.4 nm. The later part of the charge separation process is considerably slower – separation distance gradually rises up to 0.9 nm in 3.5 ps.

To simulate the experiment with the added external electric field we must take into account the fact that donor–acceptor interfaces can be arbitrarily oriented with

*Experiments performed by V. Pranculis in the group of V. Gulbinas, FTMC.

respect to the direction of the field. This situation is reproduced by performing simulations with a randomly oriented electric field and averaging the obtained electron–hole separation distance projected along the direction of the field. Our model with $J_A = 12.5\,\text{meV}$ (intermediate coupling) reproduces the experiment (see Fig. 4.6) and points to an absolute carrier separation distance of 2.5 nm in 500 fs as shown in Fig. 4.5. It is considerably smaller than the 4 nm distance evaluated in Ref. [82] for PCDTBT:$PC_{61}BM$. The latter corresponds to our model prediction in the strong coupling regime where we also obtain a carrier separation distance of 4 nm (third row in Fig. 4.5). However, at least for the case of P3TI:$PC_{71}BM$, comparison with experiment indicates that such coupling and initial separation are overestimated. Given that P3TI:$PC_{71}BM$ operates at an IQE of 90%, we thus suggest that intermediate couplings, leading to electron delocalization just over two lattice sites (Fig. 4.5), are already sufficient to facilitate efficient charge separation at organic interfaces. To further support our results we calculate electron mobilities (4.6) using the same set of parameters. The obtained values are 0.03, 0.37 and $1.26\,\text{cm}^2 \cdot \text{V}^{-1} \cdot \text{s}^{-1}$ for $J_A = 1$, 12.5 and 31.5 meV respectively. The predicted mobility at $J_A = 12.5\,\text{meV}$ is in excellent agreement with the experimentally measured electron mobility value of $0.3\,\text{cm}^2 \cdot \text{V}^{-1} \cdot \text{s}^{-1}$ in PCBM at the picosecond time scale [92].

Classical hopping models have been used extensively to describe electron–hole separation and subsequent charge motion in organic materials [93]. The simulations rely on the initial e-h distance distribution following photoexcitation, which is difficult to access experimentally. Initial charge separation distances of $3 - 4\,\text{nm}$ have been estimated [94]. Our present simulations allows us to visualize the formation of the electron–hole distance distribution with high spatio-temporal resolution. We find that coherent electron transfer when its wavepacket rapidly expands lasts up to $\sim 500\,\text{fs}$ and is responsible for shaping the "initial" electron–hole distance distribution. Following the coherent propagation stage charge separation kinetics gradually switch to the slower phase (see, e.g., the dynamics of $d_{\text{abs}}(t)$ in Fig. 4.5 calculated with $J_A = 12.5\,\text{meV}$ and exhibiting a two-phase evolution), which effectively corresponds to the incoherent-hopping phase. Strictly speaking, in this slow phase the motion of the electron is not completely incoherent because this would require all coherences in the system to die-out, thus dropping the delocalization radius to zero. However, as we see from Fig. 4.5 $R_e(t)$ saturates after approximately 500 fs consequently, this regime can be interpreted as the particle-like hopping of the "bigger" slightly delocalized electron instead of the wave-like spreading of its wavepacket. Hence, 500 fs marks the transition from coherent electron propagation to incoherent hopping where classical hopping models become valid.

Figure 4.7 shows the probability density functions of the absolute charge separation distance calculated at different times without external electric field in the

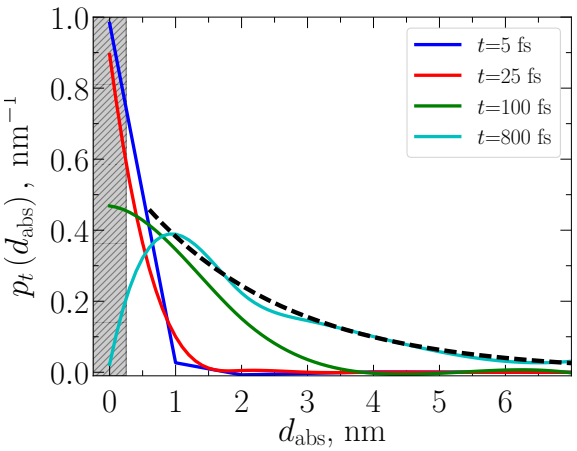

Fig. 4.7. Radial distribution of electron-hole separation distance at early times. The shaded gray area indicates the position of the donor site. Dashed black line represents the exponential character of the e-h distance distribution after 800 fs.

intermediate coupling regime. The electron gets completely transferred from the donor site to the acceptor lattice in ~ 500 fs, however, it is still strongly bound to the hole. Further charge separation is facilitated by incoherent electron hopping as outlined in Ref. [95]. The resulting electron–hole distance distribution at 800 fs can be approximated as an exponential (black dashed line in Fig. 4.7) and could be used in classical hopping models as the initial distribution.

Our results suggest a complex coherence dynamics and their role in photo-induced electron transfer at organic interfaces: electron delocalization occurs on a femtosecond time scale, during which the electron wavefunction spreads in the acceptor phase. This stage is followed by electron's partial localization and gradual loss of coherence which after several hundreds of femtoseconds leaves the electron dynamics incoherent. Although the extent of the electron wavefunction in PCBM is limited to only several molecules, it is already sufficient to facilitate an average electron-hole separation distance of ~ 2.5 nm on a femtosecond time scale. Coherent propagation also shapes the "initial" electron–hole distance distribution, which can be implemented in classical hopping models that are valid at time scales > 500 fs – the transition time from coherent propagation to incoherent hopping. We have to point out that our model does not include geminate recombination, which although considered insignificant in efficient OSC systems, is necessary for a complete description. The extent of electron delocalization, as elucidated here, may be one of the key factors minimizing geminate recombination [96]. Finally, it should be noted that our model based on the stochastic Schrödinger equation is not specific to OSCs and may be generalized to explain charge transfer not only at any molecular interface but also in other collectively coupled molecular systems.

4.3 Long-time charge separation dynamics [P2, P4]

In Section 4.2 we investigated the short-time dynamics of the electron-hole separation using the fully quantum stochastic Schrödinger equation approach which

revealed complex interplay between system's coherent evolution and bath-induced relaxation. However, after several hundreds of femtoseconds the coherent quantum effects no longer play a significant role in electron's motion and its evolution can be satisfactorily interpreted as incoherent hopping. In principle we could propagate the system for tens and hundreds of picoseconds using the stochastic Schrödinger equation, however this would be an overkill due to high computational demands of the SSE and availability of much simpler rate equation-based approaches which are completely adequate for describing incoherent dynamics. When the motion of the electron is incoherent it generally means that the off-diagonal elements of the reduced density matrix of the system (see Eqs. (1.3) and (1.4)) have already decayed to zero. In this case the evolution of the system can be described by the Pauli master equation [13, 42]

$$\frac{\mathrm{d}}{\mathrm{d}t}p_m\left(t\right) = \sum_n \left(\nu_{mn}p_n\left(t\right) - \nu_{nm}p_m\left(t\right)\right). \tag{4.7}$$

This equation describes the evolution of the system state characterized by a set of probabilities $p_m\left(t\right)$ (populations of the density matrix) for a particle to occupy the m-th site. If the coupling between different sites is small the transition between the m-th and n-th sites is governed by the rate ν_{mn} given by the Fermi–Golden–Rule $\nu_{mn} = 2\pi\left|\left\langle m\middle|\widehat{H}_{\mathrm{int}}\middle|n\right\rangle\right|^2\delta\left(\epsilon_m - \epsilon_n\right)$. Here $\widehat{H}_{\mathrm{int}}$ is the interaction Hamiltonian coupling states $\left|m\right\rangle$ and $\left|n\right\rangle$. The explicit expression of this interaction term depends on the underlying microscopic model, hence the hopping rates in the Pauli master equation are also model-dependent. One of the simplest models for hopping rate calculation is the widely used Miller–Abrahams [97] model originally designed for charge transport description in classical semiconductors. The Miller–Abrahams hopping rates are given by

$$\nu_{mn} = \nu_0 \exp\left(-2\gamma r_{mn}\right)\begin{cases}\exp\left(-\frac{\epsilon_n-\epsilon_m}{kT}\right), & \epsilon_n > \epsilon_m \\ 1, & \epsilon_n \leq \epsilon_m\end{cases}, \tag{4.8}$$

where ν_0 is a characteristic frequency of the phonon field facilitating the hopping process, γ is a parameter which characterizes the inverse localization length of the charge density and is related to the overlap integral of the wavefunctions situated on different sites, r_{mn} is the distance between the origin site m and the target site n, and ϵ_m and ϵ_n are their energies, respectively.

If the size of the simulated system is big, direct solution of Eq. (4.7) is quite difficult due to the necessity to deal with a massive system of coupled differential equations. For this reason we chose to investigate the incoherent evolution of the electron-hole pair in the P3HT:PCBM blend using Monte-Carlo (MC) modeling. We

simulate the charge separation process on the timescale from several picoseconds to nanoseconds and assess the contribution of diffusion and drift to to the process of charge separation [93]. Computational cheapness of the Monte-Carlo method allows creating much bigger donor–acceptor lattices representing the whole active layer of the OSC with its internal morphology, hence we also study the dependence of charge separation parameters on the structure of donor and acceptor domains [98].

4.3.1 Monte-Carlo model of the solar cell

P3HT:PCBM blend has a different polymer P3HT as the donor material instead of P3TI familiar from the short-time charge separation investigations in Section 4.2. However, the properties of P3HT:PCBM and P3TI:PCBM blends are comparable and the general features of charge separation dynamics are the same. Thus, in a similar fashion to the short-time dynamical model we assume the structure of the P3HT:PCBM blend to be represented by a cubic lattice, with the lattice constant a. We assume two types of sites representing electron and hole transporting moieties. The lattice is divided into the donor part, where only holes are allowed to reside and the acceptor part for electrons. To simulate the blend structure, the acceptor sites are defined by filling the lattice volume with ellipsoids described by a characteristic volume V_c and having randomly distributed semi-axes. The lengths $x = a, b, c$ of the semi-axes are given by

$$x = \frac{1}{4}\sqrt[3]{V_\mathrm{c}}\,(1 + r_x)\,, \tag{4.9}$$

where r_x is a uniformly distributed random number from the interval $[0, 1)$. These ellipsoids are placed at random positions in the lattice. We generate as many ellipsoids as the required proportion between acceptor and donor sites requests. The remaining space in the lattice is filled with donor sites, representing the polymer. The chain length is chosen randomly from the interval $[L - 3, L + 3]$, where L is the average chain length. A fragment of the final structure can be seen in Fig. 4.8.

The energy of an electron or hole is given by Eq. (4.1), only in Monte-Carlo simulations we let both charges to move through the lattice, thus the hole energy has the contributions due to the Coulomb field $\epsilon^{(h)}_{n,\mathrm{C}}$ and the external electric field $\epsilon^{(h)}_{n,F}$ as well. We also set the excitation self-energies of both donor and acceptor sites to zero. Electron and hole disorder energy contributions are sampled according to a modified Gaussian distribution defined as a weighted sum of a normal Gaussian distribution and an exponential distribution extended symmetrically to negative energy values:

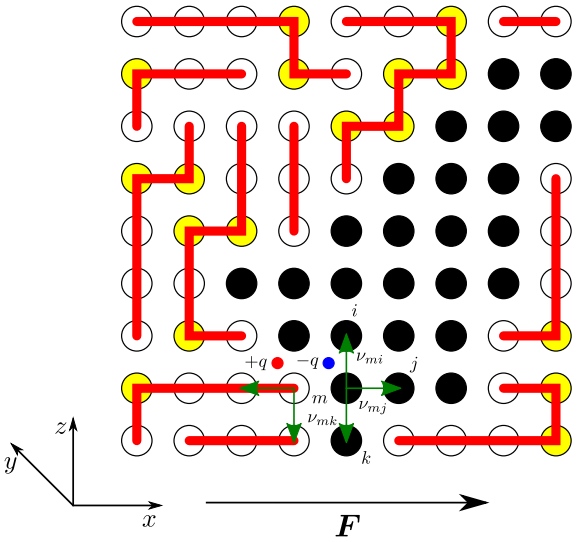

Fig. 4.8. Scheme of the model used for the Monte-Carlo calculations. Black dots represent acceptor sites, white dots represent donor sites, yellow dots represent folding points of the polymer chains, which are represented by red lines. The external electric field $\boldsymbol{F}$ is oriented along the x direction.

$$p\left(\delta_n\right) = \frac{1-w}{\sqrt{2\pi}\sigma}\exp\left(-\frac{\delta_n^2}{2\sigma^2}\right) + \frac{w}{2\sigma}\exp\left(-\frac{|\delta_n|}{\sigma}\right). \tag{4.10}$$

Here the widths of the distributions are assumed to be different for electrons and holes: σ_{D} in the donor part of the lattice (for holes) and σ_{A} in the acceptor part (for electrons). Parameter w controls the shape of the distribution $p\left(\delta_n\right)$: when $w = 1$ we have a purely exponential distribution and when $w = 0$ – Gaussian. This coefficient is necessary to correctly capture the disorder profile of the blend and, consequently, charge separation dynamics in the nanosecond timescale where according to the experimental measurements charges tend to relax into deep traps and the Gaussian distribution tails give insufficient number of such high energy sites.

At the start of the simulation, the hole and the electron are placed on neighboring sites in the interfacial region of the donor and acceptor domains. Hopping rates for both holes and electrons are given by the Miller–Abrahams formula (4.8). Only nearest neighbor sites are taken into account for a hopping event. Thus, a charge can hop into one of six surrounding sites when it is far from the interface, while hopping possibilities are fewer in the interfacial region. In the acceptor domain the rate prefactor $\nu_0 \equiv \nu_{\mathrm{A}}$ is constant, whereas in the donor part we assume $\nu_0 \equiv \nu_{\mathrm{D1}}$ for hopping to a target site located in a straight part of the same polymer chain, $\nu_0 \equiv \nu_{\mathrm{D2}}$ for hopping to a target site located on a folding point where orientation of the polymer chain changes, and $\nu_0 \equiv \nu_{\mathrm{D3}}$ for hopping to a target site located in a different polymer chain. Carrier motion in a hierarchical polymer structure is expressed by defining $\nu_{\mathrm{D1}} > \nu_{\mathrm{D2}} > \nu_{\mathrm{D3}}$. Since in our model both types of charges can hop through their respective domains we calculate the probability of obtaining a new configuration of charges n from the previous configuration m using the expression

$$p_{mn} = \frac{\nu_{mn}}{\sum\limits_{k \in m \to n} \nu_k}. \tag{4.11}$$

Here the summation is performed over the rates of all allowed jumps of both the electron and the hole. These probabilities are used to determine the destination site for either the hole or the electron, chosen by a linearly distributed random number. The charge configuration is then switched to the one that has been determined and the rates of the next hopping events are recalculated.

The time interval between two hops is taken as a random value described by the exponential distribution, characterizing the total hopping rate. In the m-th configuration, the time to reach the n-th configuration, τ_m, is a random number drawn from

$$p\left(\tau_m\right) = \frac{1}{\overline{\tau}_m} \exp\left(-\frac{\tau_m}{\overline{\tau}_m}\right), \tag{4.12}$$

where $\overline{\tau}_m$ is the lifetime of the m-th configuration:

$$\overline{\tau}_m = \frac{1}{\sum\limits_{k \in m \to n} \nu_k}. \tag{4.13}$$

Eqs. (4.12) and (4.13) determine the time flow of the simulation which allows us to calculate the time-dependent characteristics of charge evolution.

4.3.2 Simulation results and comparison with the experiment

Stochastic Schrödinger equation simulations in Section 4.2 revealed the general features of the initial charge separation dynamics up to several picoseconds. To investigate the evolution of charge pairs beyond this timescale we use the incoherent Monte-Carlo model which is fully applicable in this case due to quantum effects in the system becoming negligible already after several hundreds of femtoseconds.

For the simulation we choose a lattice of $100 \times 400 \times 400\,\mathrm{nm}$ representing the actual structure of the blend, therefore, no cyclic boundary conditions are introduced. Initially, charges are created at a random location on the interface and due to the external electric field, diffusion and boundary effect they drift apart in opposite directions. While charges move through the lattice, we record the absolute charge separation distance $d_{\mathrm{abs}}\left(t\right)$ and the drift separation distance $d_F\left(t\right)$ between them along the direction of the external electric field $\boldsymbol{F}$. In order to give our simulations a connection to real-life measurements of the charge separation dynamics in the P3HT:PCBM blend we fit the simulated drift separation distance kinetics to the experimental data obtained using the TREFISH method [93]. These results are

Table 4.1. Numerical values of the model parameters corresponding to the results in Fig. 4.9.

Lattice dimension in the x direction, (nm)	Lattice dimension in the y direction, (nm)	Lattice dimension in the z direction, (nm)	Lattice constant a, (nm)	Characteristic volume of the acceptor ellipsoid, (nm^3)
100	400	400	1	18000
Average length of the donor chain, (nm)	Hopping rate prefactor in the acceptor ν_{A}, (s^{-1})	Hopping rate prefactor in the donor ν_{D1}, (s^{-1})	Hopping rate prefactor in the donor ν_{D2}, (s^{-1})	Hopping rate prefactor in the donor ν_{D3}, (s^{-1})
6	7.2×10^{15}	3×10^{16}	1×10^{16}	3.5×10^{15}
Parameter γ, (nm^{-1})	Disorder in the acceptor σ_{A}, (meV)	Disorder in the donor σ_{D}, (meV)	Temperature T, (K)	Mean dielectric permittivity ϵ
5	70	80	293	3
Fraction w of exponential distribution in the modified Gaussian distribution (see Eq. (4.10))			CT state energy, (eV)	
0.14			0.2	

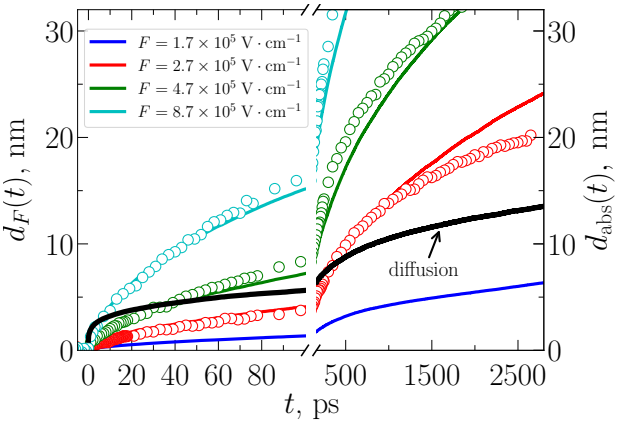

Fig. 4.9. Experimental kinetics of the drift charge separation distance $d_F\,(t)$(empty circles) together with simulated Monte-Carlo results (solid curves). Thick solid black curve represents the absolute charge separation distance at zero external electric field.

shown in Fig. 4.9[†]. Parameter values of the simulation including those obtained from the fitting procedure are given in Table 4.1. The obtained best-fit energy disorder values for acceptor and donor materials, 70 and 80 meV respectively are close to those determined in the study by Deibel *et al.* [99]. The Coulomb potential (4.2) profile is set to give the CT state energy of 0.2 eV, consistent with Ref. [100]. We set the coefficient w in the distribution (4.10) to 0.14, implying that the modified Gaussian distribution practically has the shape of an ordinary Gaussian distribution only with the addition of somewhat longer exponential tails.

Random hopping of the electron–hole pair in our Monte-Carlo model is a simulation of a diffusion process with the constraint of finite and irregular electron and

[†]Experiments performed by D. A. Vithanage and Y. Infahsaeng, Lund University.

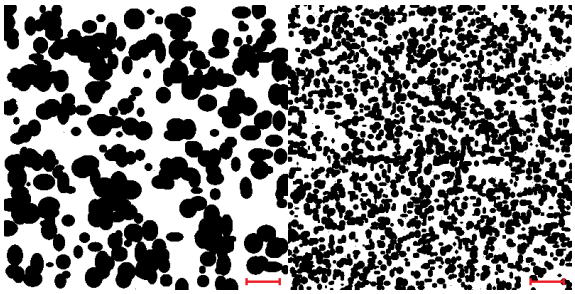

Fig. 4.10. Cross section of typical simulated structures of annealed (left) and as-spun (right) samples. Dark areas denote acceptor regions (PCBM) and white areas denote donor regions (P3HT). The red line represents the length of 50 nm.

hole domains and the mutual attracting force between both charges. Adding the external electric field introduces the drift component in the charge motion which is quantified in our calculations by the drift charge separation distance $d_F(t)$. In order to investigate the interplay between diffusion and drift contributions we must first obtain the charge separation kinetic without the drift component. Thus, we calculate the absolute charge separation distance $d_{\text{abs}}(t)$ at zero external electric field (Fig. 4.9). Black curve in Fig. 4.9 shows that after 10 ps charge carriers are already dragged apart by ~ 3 nm by diffusion, whereas the drift separation distances are smaller with all but the strongest external electric fields. The drift starts to contribute more substantially to the carrier separation during the slower ($t > 20$ ps) phase, but diffusion still strongly dominates at typical electric fields in solar cells ($\sim 1 \times 10^5\,\text{V} \cdot \text{cm}^{-1}$), even on a sub-nanosecond timescale when the Coulomb electron–hole attraction is effectively overcome ($\sim 7 - 8$ nm). These observations are confirmed by the calculations using the Einstein relation connecting the experimentally measured charge mobility kinetics and the time-dependent diffusion coefficient which is then used to obtain the diffusion distance distributions at different time moments [93].

Absolute charge separation distance calculated with Monte-Carlo method (black curve in Fig. 4.9) can be directly compared to analogous kinetics from Fig. 4.5 obtained using the SSE formalism. The latter gives the absolute e-h separation distance of approximately a few nanometers after several picoseconds. At this timescale our Monte-Carlo simulations become valid and we can see from Fig. 4.9 that diffusion separates the charge pair by several nanometers as well. As we mentioned in Subsection 4.3.1 the polymers in the blends used for experimental measurements in Figs. 4.6 and 4.9 were different. However, as the hole mobility is much lower than the electron mobility we can safely assume that the overall charge separation dynamics, at least on the timescale of a few picoseconds, is shaped by the electron motion which is not sensitive to the donor material type.

The morphology of the blend, on the other hand, is a major factor influencing the dynamics of charge separation. In Fig. 4.10 two simulated blend structures are shown: annealed sample on the left and as-spun sample on the right. Annealing to a high temperature changes the morphology and enhances the hole mobil-

ity [101, 102], resulting in it being only an order of magnitude below the electron mobility [101]. A similar effect was achieved with slow solvent evaporation [103]. Using microsecond time scale techniques, a large spread in mobilities and their differences in as-spun and annealed samples have been reported [101, 104, 105]. The measurements show that the two different processing methods drastically affect the mobility and charge separation time scales. Morphological studies have shown that high temperature results in phase separation due to crystallization of the polymer [101, 104, 106, 107] and formation of large PCBM clusters [104, 106, 108–110]. There is a consensus that thermal annealing results in improved device efficiency due to enhanced phase segregation, which consequently leads to increased charge separation efficiency [111, 112], improved hole conductivity and formation of optimized charge transport pathways [102, 104] and consequently reduced bimolecular recombination [113].

The mechanism through which the thermal annealing process enables higher charge carrier mobilities is now fairly well understood. Annealing induced crystallization of the polymer results in larger domains (thicker lamellae) of the pure polymer and at the same time expels fullerene molecules out of the crystallizing polymer, thereby making more fullerene available [104, 107, 114, 115] to build a robust electron transport network. It is clear from such studies that the improvement in charge collection (reflected through photocurrent quantum efficiency) is associated with the growth in pure polymer and fullerene domains and resulting improvement in charge carrier mobility relative to the recombination coefficient [101, 102].

To investigate quantitatively charge separation dynamics in polymer–fullerene blends with different morphologies we use the same Monte-Carlo model from Subsection 4.3.1 and calculate the drift and absolute electron–hole pair separation distances. Carrier drift kinetics in as-spun and annealed samples are modeled by using exactly the same model parameters except for polymer and PCBM domain sizes. The best agreement was obtained with an average acceptor domain diameter of $7.5\,\mathrm{nm}$ for the as-spun sample and $33\,\mathrm{nm}$ for the annealed sample. As a result of fullerene aggregation the polymer domain dimensions were accordingly larger for annealed samples as well, but because of non-regular shapes their quantitative characterization, is more difficult. Fig. 4.10 illustrates the corresponding material morphologies and Fig. 4.11[‡] shows the simulated carrier drift dynamics. The quite good agreement with experimental results obtained for all curves with only one free variable, the domain size, validates the simulation results. The obtained domain dimensions of the annealed samples are somewhat larger than the $\sim 10\,\mathrm{nm}$ domains estimated in similar samples from experimental results [116]. On the other hand,

[‡]Experiments performed by D. A. Vithanage and Y. Infahsaeng, Lund University.

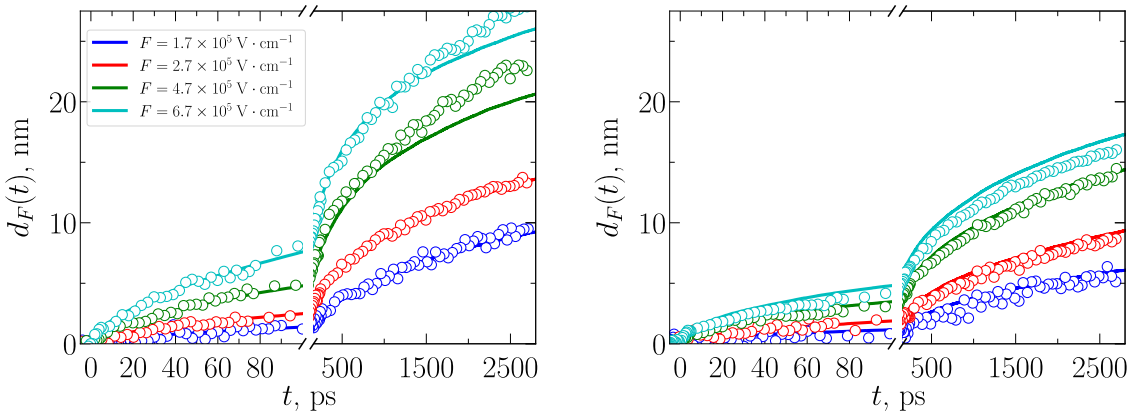

Fig. 4.11. Experimental (empty circles) and simulated (solid curves) charge drift dynamics in the annealed (left) and as-spun (right) samples at various electric fields strengths.

quite similar domain sizes of 10 to 30 nm were estimated by MC modeling of carrier recombination in a P3HT:PCBM blend [113]. Monte-Carlo simulations do not perfectly reproduce the carrier drift kinetics in annealed samples at high applied electric fields ($6.7 \times 10^5\,\mathrm{V \cdot cm^{-1}}$) at times longer than 1 ns. This is not very surprising taking into account the relatively simple blend structure used in calculations.

We proceed to infer effective charge carrier mobilities from the data of drift charge separation distance as a function of time using Eq. (4.6). Note that these are not mobilities as usually defined, describing drift of relaxed populations of charges in the steady state, but instantaneous mobilities describing the instantaneous separation velocity of unrelaxed charge carrier populations. Since the experimental data gives us information on the sum of electron and hole drift distances, the actual electron and hole mobilities remain undisclosed, the ratio between electron and hole hopping rates being a free parameter. We have chosen the electron hopping rate on the basis of additional available information on the ultrafast time-resolved electron mobility and on the basis of the best agreement between experimental and calculated carrier drift kinetics. By means of time-resolved microwave conductivity [117], Savenije *et al.* obtained the electron mobility inside PCBM nanocrystals of $8 \times 10^{-2}\,\mathrm{cm^2 \cdot V^{-1} \cdot s^{-1}}$ and a similar mobility of about $0.1\,\mathrm{cm^2 \cdot V^{-1} \cdot s^{-1}}$ was also obtained on a subpicosecond - several picosecond timescale in PCBM film by dynamic Stark effect measurements [118]. Thus, we have chosen an electron hopping rate prefactor ν_A to give an electron mobility of $0.1\,\mathrm{cm^2 \cdot V^{-1} \cdot s^{-1}}$ at 0.3 ps, while its subsequent evolution was obtained from the best fitting with experimental data. Similar information on the initial hole mobility in P3HT is not available and therefore it was obtained from the modeling of the carrier drift kinetics. The best agreement was obtained with about ten times lower hole mobility than that of electrons. The simulation parameters used to obtain the best agreement between

Table 4.2. Numerical values of the model parameters corresponding to the results in Fig. 4.11.

Characteristic volume of the acceptor ellipsoid, (nm^3)	Hopping rate prefactor in the acceptor ν_A, (s^{-1})	Hopping rate prefactor in the donor ν_{D1}, (s^{-1})	Hopping rate prefactor in the donor ν_{D2}, (s^{-1})	Hopping rate prefactor in the donor ν_{D3}, (s^{-1})
as-spun: 220, annealed: 19800	2.8×10^{16}	2×10^{15}	1×10^{15}	5×10^{14}
Fraction w of exponential distribution in the modified Gaussian distribution (see Eq. (4.10))			CT state energy, (eV)	
0.19			0.17	

calculated and measured drift kinetics (see Fig. 4.11) are presented in Table 4.2. Other model parameters are the same as in Table 4.1.

Next we calculate the average absolute carrier separation distances $d_{\text{abs}}(t)$ caused by both carrier drift and diffusion using the same set of parameters as for the carrier drift kinetics. Fig. 4.12 shows a comparison of the absolute carrier separation distances in as-spun and annealed samples at different electric field strengths. At zero electric field, only the diffusion drives the carrier motion, thus curves at zero field represent diffusion driven charge separation dynamics. At 0 and $1.7 \times 10^5\,\text{V} \cdot \text{cm}^{-1}$ electric fields the separation distances on a tens of picoseconds timescale are almost independent of the sample annealing. The difference appears on a nanosecond timescale, when electrons approach the boundaries of small PCBM domains in the as-spun sample, while in the annealed sample with larger PCBM domains, they continue an unrestricted motion. At higher electric field, when the carrier drift contributes more to their motion, charge carriers move faster and reach domain boundaries in the as-spun sample already on a picosecond timescale, thus the difference in separation distances appears already during tens of picoseconds. Strongly restricted carrier motion in the as-spun sample with smaller PCBM and polymer domains prevents carrier escape from the Coulomb attraction. In devices such restricted carrier motion leads to enhanced charge carrier recombination, which is apparently one of the major factors limiting the carrier generation yield and performance efficiency of non-annealed P3HT:PCBM solar cells [113].

Our MC simulations have been performed assuming that only nearest neighbor electron–hole pairs are created by exciton splitting at the donor–acceptor interface as was suggested in Refs. [93] and [119]. However, there are publications [79,99,120] arguing that charge carrier separation at much longer distances takes place on a femtosecond time scale and it helps for final separation of electron–hole pairs into free charges. This point of view is also supported by the short-time charge separation dynamics results discussed in Section 4.2. Since this is still not a fully settled

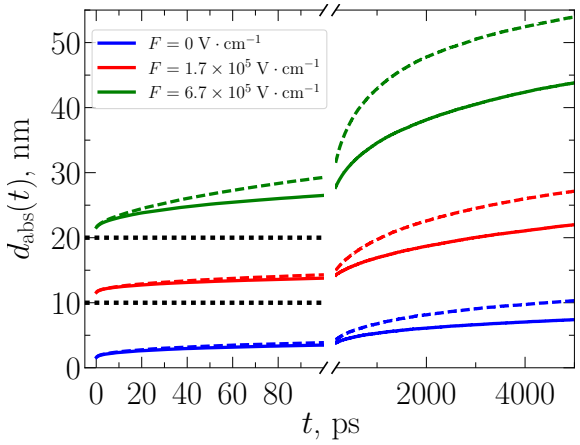

Fig. 4.12. Absolute charge separation distances in annealed (dashed curves) and as-spun (solid curves) samples at different electric field strengths obtained by Monte Carlo simulation using the model parameters fitted to the drift distance data in Fig. 4.11. The curves at higher electric field strengths are vertically shifted.

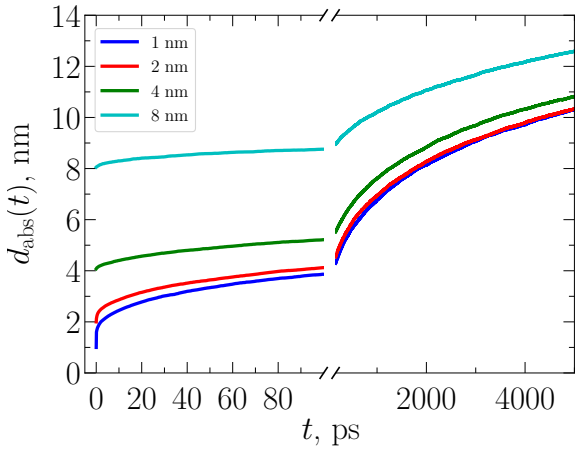

Fig. 4.13. Calculated time dependence of the absolute carrier separation distance at zero electric field and at various initial separation distances.

question, which could be also related to the blend annealing, we have also performed additional calculations directed towards evaluation of the role of the initial carrier separation distance in the charge separation process. Fig. 4.13 shows the calculated absolute charge carrier separation distances at zero applied field with the model parameters taken from Table 4.2. Diffusion driven separation at long times is large with larger initial separation, but the influence of the initial separation gradually decreases with time and after several nanoseconds the separation distance is almost independent of the initial ultrafast separation if this separation is significantly smaller than 8 ns. Thus, initial carrier separation only weakly influences the final carrier separation process (at several nanoseconds when charges have reached a distance where the electrostatic attraction energy is similar to the thermal energy quantum $k_B T$), unless the initial separation is comparable with the Coulomb capture radius.

Our experimental investigations of the initial carrier motion in as-spun and annealed P3HT:PCBM blends together with Monte Carlo simulations of the carrier drift dynamics suggest a mechanism for the improved performance of annealed solar cells. The carrier drift separation distances, on a subnanosecond–nanosecond timescale are about two times larger in annealed samples (see Fig. 4.11). Monte-Carlo simulations of the motion dynamics suggest that the increase in the carrier

separation rate caused by blend annealing is related to the increased polymer and PCBM domain sizes enabling longer distance carrier separation on a picosecond time scale, which reduces the probability of their geminate recombination and thus increases the free charge carrier generation yield in annealed samples. On the other hand, the role of other material properties such as the presence of energy traps, or formation of semi-crystalline polymer domains, which change as a result of annealing, cannot be completely ruled out.

Additional MC simulations directed towards evaluation of the role of the initial carrier separation distance showed that the more efficient carrier separation in annealed samples can be hardly related to increased initial carrier separation distance. The initial separation distance only weakly influences the carrier separation efficiency at times and distances where free charges are formed if it is shorter than about 8 nm, while longer distance separation is non-compatible with the experimental data presented in both Sections 4.2 and 4.3.

4.4 Conclusions

In Chapter 4 Section 4.2 we used the stochastic Schrödinger equation to model short-time charge separation dynamics in the organic solar cells. We calculated absolute and drift charge separation distance kinetics for different inter-acceptor couplings over the femtosecond to picosecond timescale and revealed the complex evolution of the electron which allows us to state that **the stochastic Schrödinger equation adequately captures the dynamics of the charge separation in bulk heterojunction organic solar cells from the beginning of the coherent phase of the exciton dissociation, through the transient phase of partially delocalized charges until the incoherent hopping phase of separated charges**. **The initial coherent spreading of the electron wavefunction greatly facilitates further electron-hole pair separation**. This is the **third** statement of the thesis.

Further, in Section 4.3 we turned our attention to long-time charge separation dynamics in the organic blends and model this process using the Monte-Carlo method. Calculation of absolute and drift charge separation distance kinetics together with experimental data showed that **diffusion is the main driving force behind the charge separation at long times with minor contribution from the drift in the internal electric field inside the organic solar cell**. Performing the same calculations using lattices that describe different morphologies of the organic blend we found that **cell morphology greatly influences the charge pair motion as smaller donor and acceptor material domains limit the range of charge separation distance**. This is the **fourth** statement of the thesis.

Summary of the results

In this thesis we address the complex issues regarding the energy and charge transport in various organic molecular systems such as photosynthetic aggregates and organic material blends used in solar cells. These systems are generally described as open quantum systems where the small part of the whole containing a few relevant degrees of freedom (the reduced system) interacts with the rest of the system denoted as the bath. Solving the dynamics of the reduced system is a highly non-trivial problem requiring sophisticated quantum mechanical approaches due to the necessity to incorporate the influence of the bath on the evolution of the relevant system. The problem becomes even more complicated when we want to perform calculations of processes, e. g., energy transport and charge separation, manifesting over many different timescales, from femtoseconds to microseconds. In this case, several methods of calculations are needed, and it is usually a difficult task to bridge them together and ensure the correct description of the intermediate timescales. Another issue encountered when investigating real-life organic molecular compounds is the wide range of interaction strength between the system and its environment which again requires different theoretical methods for calculations with different system–bath couplings.

In Chapter 2 we develop the stochastic Schrödinger equation (SSE) formalism to obtain a consistent approach for tackling open quantum system evolution problems over a wide range of timescales and interaction strengths. We start with the general path integral theory for the general reduced system's dynamics and derive several forms of stochastic equations incorporating the effects of the bath through the addition of Gaussian complex-valued fluctuations to the usual Schrödinger equation. We further explore possible simplifications of the SSE and obtain its form with the applied weak system–bath approximation. Later we develop a systematic approach to solve the general formally exact SSE with a linear system–bath coupling of arbitrary strength up to a desired accuracy. This results in a hierarchy of coupled stochastic equation which we denote as hierarchical stochastic Schrödinger equation (HSSE). The accuracy of both weak-coupling SSE and HSSE is tested on a toy two-site system and it is found to be satisfactory in a wide range of system parameters. We also introduce a general procedure to calculate probabilistic characteristics of system

observables using the stochastic Schrödinger equation. Particularly, we apply it to obtain excitation transfer time distributions in an open quantum system.

The weak-coupling SSE is applied for calculation of excitation energy transfer in the photosynthetic Fenna–Matthews–Olson (FMO) complex in Chapter 3. We calculate the evolution of the 7-site FMO system interacting with the bath described by two different spectral density models and reveal the influence of high-frequency modes in the energy transfer dynamics. Using the transfer time distributions we investigate the excitation transfer pathway through the FMO aggregate and find that it only weakly depends on the presence of high-frequency modes in the environment.

We next turn to studying the charge separation process in organic solar cells (OSCs). In Chapter 4 we model the OSC as a cubic lattice of sites representing the donor and acceptor molecules of the organic blend material. Application of the SSE allows us to reveal the complex dynamics of the electron during the initial phase of the separation on the scale of several picoseconds. Calculations show how the coherent evolution of the electron gradually transitions into incoherent hopping motion due to the dephasing influence of the bath. For investigation of the incoherent motion stage of the charge separation process we choose the Monte-Carlo method. Hopping rates between the different sites of the system are described using the Miller–Abrahams model. Calculations of the charge separation dynamics up until the nanosecond timescale shows the dominating contribution of the diffusion in moving charges apart from each other. We also investigate the influence of the organic blend's morphology on the charge separation distance and find that larger clusters of donor material facilitate longer separation distances.

Bibliography

[1] X. Wang, K. Maeda, X. Chen, K. Takanabe, K. Domen, Y. Hou, X. Fu and M. Antonietti, *Polymer semiconductors for artificial photosynthesis: hydrogen evolution by mesoporous graphitic carbon nitride with visible light*, J. Am. Chem. Soc. **131**, 1680–1681 (2009).

[2] Y. Tachibana, L. Vayssieres and J. R. Durrant, *Artificial photosynthesis for solar water-splitting*, Nat. Photonics **6**, 511–518 (2012).

[3] D. Gust, T. A. Moore and A. L. Moore, *Solar fuels via artificial photosynthesis*, Acc. Chem. Res. **42**, 1890–1898 (2009).

[4] A. J. Bard and M. A. Fox, *Artificial photosynthesis: solar splitting of water to hydrogen and oxygen*, Acc. Chem. Res. **28**, 141–145 (1995).

[5] R. E. Blankenship, D. M. Tiede, J. Barber, G. W. Brudvig, G. Fleming, M. Ghirardi, M. Gunner, W. Junge, D. M. Kramer, A. Melis *et al.*, *Comparing photosynthetic and photovoltaic efficiencies and recognizing the potential for improvement*, Science **332**, 805–809 (2011).

[6] M.-Q. Yang, N. Zhang, M. Pagliaro and Y.-J. Xu, *Artificial photosynthesis over graphene - semiconductor composites. Are we getting better?*, Chem. Soc. Rev. **43**, 8240–8254 (2014).

[7] H.-L. Guo, H. Du, Y.-F. Jiang, N. Jiang, C.-C. Shen, X. Zhou, Y.-N. Liu and A.-W. Xu, *Artificial photosynthetic z-scheme photocatalyst for hydrogen evolution with high quantum efficiency*, J. Phys. Chem. C **121**, 107–114 (2017).

[8] I. Gur, N. A. Fromer, M. L. Geier and A. P. Alivisatos, *Air-stable all-inorganic nanocrystal solar cells processed from solution*, Science **310**, 462–465 (2005).

[9] K. Masuko, M. Shigematsu, T. Hashiguchi, D. Fujishima, M. Kai, N. Yoshimura, T. Yamaguchi, Y. Ichihashi, T. Mishima, N. Matsubara *et al.*, *Achievement of more than 25% conversion efficiency with crystalline silicon heterojunction solar cell*, IEEE J. Photovolt. **4**, 1433–1435 (2014).

[10] M. A. Green, K. Emery, Y. Hishikawa, W. Warta and E. D. Dunlop, *Solar cell efficiency tables (version 45)*, Prog. Photovolt. Res. Appl. **23**, 1–9 (2015).

[11] S. Kim, J.-W. Chung, H. Lee, J. Park, Y. Heo and H.-M. Lee, *Remarkable progress in thin-film silicon solar cells using high-efficiency triple-junction technology*, Sol. Energy Mater. Sol. Cells **119**, 26–35 (2013).

[12] L. Valkunas, D. Abramavicius and T. Mančal, *Molecular excitation dynamics and relaxation: quantum theory and spectroscopy* (John Wiley & Sons, 2013).

[13] V. May, K. Oliver *et al.*, *Charge and energy transfer dynamics in molecular systems* (John Wiley & Sons, 2008).

[14] W. T. Pollard and R. A. Friesner, *Solution of the Redfield equation for the dissipative quantum dynamics of multilevel systems*, J. Chem. Phys. **100**, 5054–5065 (1994).

[15] M. Yang and G. R. Fleming, *Influence of phonons on exciton transfer dynamics: comparison of the Redfield, Förster, and modified Redfield equations*, Chem. Phys. **282**, 163–180 (2002).

[16] J. Ma and J. Cao, *Förster resonance energy transfer, absorption and emission spectra in multichromophoric systems. I. Full cumulant expansions and system-bath entanglement*, J. Chem. Phys. **142**, 094106 (2015).

[17] Y.-H. Hwang-Fu, W. Chen and Y.-C. Cheng, *A coherent modified Redfield theory for excitation energy transfer in molecular aggregates*, Chem. Phys. **447**, 46–53 (2015).

[18] U. Weiss, *Quantum dissipative systems* (World Scientific, 2012).

[19] V. I. Novoderezhkin, A. G. Yakovlev, R. van Grondelle and V. A. Shuvalov, *Coherent nuclear and electronic dynamics in primary charge separation in photosynthetic reaction centers: a Redfield theory approach*, J. Phys. Chem. B **108**, 7445–7457 (2004).

[20] J. Jeske, D. J. Ing, M. B. Plenio, S. F. Huelga and J. H. Cole, *Bloch-Redfield equations for modeling light-harvesting complexes*, J. Chem. Phys. **142**, 064104 (2015).

[21] G. Panitchayangkoon, D. V. Voronine, D. Abramavicius, J. R. Caram, N. H. Lewis, S. Mukamel and G. S. Engel, *Direct evidence of quantum transport in photosynthetic light-harvesting complexes*, Proc. Natl. Acad. Sci. U.S.A. **108**, 20908–20912 (2011).

[22] D. Abramavicius, B. Palmieri, D. V. Voronine, F. Šanda and S. Mukamel, *Coherent multidimensional optical spectroscopy of excitons in molecular aggregates; quasiparticle versus supermolecule perspectives*, Chem. Rev. **109**, 2350–2408 (2009).

[23] R. P. Feynman and F. L. Vernon, *The theory of a general quantum system interacting with a linear dissipative system*, Ann. Phys. **24**, 118–173 (1963).

[24] Y. Tanimura and R. Kubo, *Two-time correlation functions of a system coupled to a heat bath with a Gaussian-Markoffian interaction*, J. Phys. Soc. Jpn. **58**, 1199–1206 (1989).

[25] Y. Tanimura, *Stochastic Liouville, Langevin, Fokker-Planck, and master equation approaches to quantum dissipative systems*, J. Phys. Soc. Jpn. **75**, 082001 (2006).

[26] N. Makri, *Numerical path integral techniques for long time dynamics of quantum dissipative systems*, J. Math. Phys. **36**, 2430–2457 (1995).

[27] A. J. Daley, C. Kollath, U. Schollwöck and G. Vidal, *Time-dependent density-matrix renormalization-group using adaptive effective Hilbert spaces*, J. Stat. Mech. Theor. Exp. **2004**, P04005 (2004).

[28] S. R. White and A. E. Feiguin, *Real-time evolution using the density matrix renormalization group*, Phys. Rev. Lett. **93**, 076401 (2004).

[29] J. Prior, A. W. Chin, S. F. Huelga and M. B. Plenio, *Efficient simulation of strong system-environment interactions*, Phys. Rev. Lett. **105**, 050404 (2010).

[30] J. Eckel, F. Heidrich-Meisner, S. G. Jakobs, M. Thorwart, M. Pletyukhov and R. Egger, *Comparative study of theoretical methods for non-equilibrium quantum transport*, New J. Phys. **12**, 043042 (2010).

[31] V. Chorošajev, A. Gelzinis, L. Valkunas and D. Abramavicius, *Dynamics of exciton-polaron transition in molecular assemblies: The variational approach*, J. Chem. Phys. **140**, 244108 (2014).

[32] V. Chorošajev, O. Rancova and D. Abramavicius, *Polaronic effects at finite temperatures in the B850 ring of the LH2 complex*, Phys. Chem. Chem. Phys. **18**, 7966–7977 (2016).

[33] C. L. Mehta, *Diagonal coherent-state representation of quantum operators*, Phys. Rev. Lett. **18**, 752–754 (1967).

[34] J. W. Negele and H. Orland, *Quantum many-particle systems* (Westview, 1988).

[35] J. Hubbard, *Calculation of partition functions*, Phys. Rev. Lett. **3**, 77 (1959).

[36] R. L. Stratonovich, *On a method of calculating quantum distribution functions*, Sov. Phys. Dokl. **2**, 416 (1957).

[37] A. Vourdas and R. Bishop, *Thermal coherent states in the Bargmann representation*, Phys. Rev. A **50**, 3331 (1994).

[38] L. Diósi and W. T. Strunz, *The non-Markovian stochastic Schrödinger equation for open systems*, Phys. Lett. A **235**, 569–573 (1997).

[39] L. Diósi, N. Gisin and W. T. Strunz, *Non-Markovian quantum state diffusion*, Phys. Rev. A **58**, 1699 (1998).

[40] M. Suzuki, *Quantum analysis - non-commutative differential and integral calculi*, Commun. Math. Phys. **183**, 339–363 (1997).

[41] B. Gough, *GNU Scientific Library Reference Manual - Third Edition* (Network Theory Ltd., 2009), 3rd ed.

[42] C. W. Gardiner and H. Haken, *Quantum noise* (Springer Berlin, 1991).

[43] H.-P. Breuer and F. Petruccione, *The theory of open quantum systems* (Oxford University Press on Demand, 2002).

[44] A. Gelzinis, D. Abramavicius and L. Valkunas, *Non-Markovian effects in time-resolved fluorescence spectrum of molecular aggregates: Tracing polaron formation*, Phys. Rev. B **84**, 245430 (2011).

[45] M. A. Schlosshauer, *Decoherence: and the quantum-to-classical transition* (Springer Science & Business Media, 2007).

[46] J. M. Moix, Y. Zhao and J. Cao, *Equilibrium-reduced density matrix formulation: influence of noise, disorder, and temperature on localization in excitonic systems*, Phys. Rev. B **85**, 115412 (2012).

[47] U. Peskin and M. Steinberg, *A temperature-dependent Schrödinger equation based on a time-dependent self consistent field approximation*, J. Chem. Phys. **109**, 704–710 (1998).

[48] D. Suess, A. Eisfeld and W. Strunz, *Hierarchy of stochastic pure states for open quantum system dynamics*, Phys. Rev. Lett. **113**, 150403 (2014).

[49] G. S. Engel, T. R. Calhoun, E. L. Read, T.-K. Ahn, T. Mančal, Y.-C. Cheng, R. E. Blankenship and G. R. Fleming, *Evidence for wavelike energy transfer through quantum coherence in photosynthetic systems*, Nature **446**, 782–786 (2007).

[50] G. Panitchayangkoon, D. Hayes, K. A. Fransted, J. R. Caram, E. Harel, J. Wen, R. E. Blankenship and G. S. Engel, *Long-lived quantum coherence in photosynthetic complexes at physiological temperature*, Proc. Natl. Acad. Sci. U.S.A. **107**, 12766–12770 (2010).

[51] V. I. Novoderezhkin and R. van Grondelle, *Physical origins and models of energy transfer in photosynthetic light-harvesting*, Phys. Chem. Chem. Phys. **12**, 7352–7365 (2010).

[52] A. Ishizaki, T. R. Calhoun, G. S. Schlau-Cohen and G. R. Fleming, *Quantum coherence and its interplay with protein environments in photosynthetic electronic energy transfer*, Phys. Chem. Chem. Phys. **12**, 7319–7337 (2010).

[53] A. Olaya-Castro and G. D. Scholes, *Energy transfer from Förster-Dexter theory to quantum coherent light-harvesting*, Int. Rev. Phys. Chem. **30**, 49–77 (2011).

[54] B. Mennucci and C. Curutchet, *The role of the environment in electronic energy transfer: a molecular modeling perspective*, Phys. Chem. Chem. Phys. **13**, 11538–11550 (2011).

[55] G. S. Schlau-Cohen, A. Ishizaki and G. R. Fleming, *Two-dimensional electronic spectroscopy and photosynthesis: Fundamentals and applications to photosynthetic light-harvesting*, Chem. Phys. **386**, 1–22 (2011).

[56] C. König and J. Neugebauer, *Quantum chemical description of absorption properties and excited-state processes in photosynthetic systems*, ChemPhysChem **13**, 386–425 (2012).

[57] L. A. Pachón and P. Brumer, *Physical basis for long-lived electronic coherence in photosynthetic light-harvesting systems*, J. Phys. Chem. Lett. **2**, 2728–2732 (2011).

[58] Y. Cheng and G. R. Fleming, *Dynamics of light harvesting in photosynthesis*, Annu. Rev. Phys. Chem. **60**, 241 (2009).

[59] T. Mančal, N. Christensson, L. Vladimír, F. Milota, O. Bixner, H. F. Kauffmann and J. Hauer, *System-dependent signatures of electronic and vibrational coherences in electronic two-dimensional spectra*, J. Phys. Chem. Lett. **3**, 1497–1502 (2012).

[60] N. Christensson, H. F. Kauffmann, T. Pullerits and T. Mančal, *Origin of long-lived coherences in light-harvesting complexes*, J. Phys. Chem. B **116**, 7449–7454 (2012).

[61] T. Mančal, A. Nemeth, F. Milota, V. Lukeš, H. F. Kauffmann and J. Sperling, *Vibrational wave packet induced oscillations in two-dimensional electronic spectra. II. Theory*, J. Chem. Phys. **132**, 184515 (2010).

[62] M. Chachisvilis, H. Fidder, T. Pullerits and V. Sundström, *Coherent nuclear motions in light-harvesting pigments and dye molecules, probed by ultrafast spectroscopy*, J. Raman Spectrosc. **26**, 513–522 (1995).

[63] M. T. W. Milder, B. Brüggemann, R. van Grondelle and J. L. Herek, *Revisiting the optical properties of the FMO protein*, Photosynth. Res. **104**, 257–274 (2010).

[64] C. Kreisbeck, T. Kramer and A. Aspuru-Guzik, *Disentangling electronic and vibronic coherences in two-dimensional echo spectra*, J. Phys. Chem. B **117**, 9380–9385 (2013).

[65] V. Butkus, D. Zigmantas, L. Valkunas and D. Abramavicius, *Vibrational vs. electronic coherences in 2D spectrum of molecular systems*, Chem. Phys. Lett. **545**, 40–43 (2012).

[66] V. Butkus, D. Zigmantas, D. Abramavicius and L. Valkunas, *Distinctive character of electronic and vibrational coherences in disordered molecular aggregates*, Chem. Phys. Lett. **587**, 93–98 (2013).

[67] S. Westenhoff, D. Paleček, P. Edlund, P. Smith and D. Zigmantas, *Coherent picosecond exciton dynamics in a photosynthetic reaction center*, J. Am. Chem. Soc. **134**, 16484–16487 (2012).

[68] M. Mohseni, P. Rebentrost, S. Lloyd and A. Aspuru-Guzik, *Environment-assisted quantum walks in photosynthetic energy transfer*, J. Chem. Phys. **129**, 174106 (2008).

[69] V. Abramavicius and D. Abramavicius, *Excitation transfer pathways in excitonic aggregates revealed by the stochastic Schrödinger equation*, J. Chem. Phys. **140**, 065103 (2014).

[70] R. Fenna, L. Eyck and B. Matthews, *Atomic coordinates for the chlorophyll core of a bacteriochlorophyll a-protein from green photosynthetic bacteria*, Biochem. Biophys. Res. Commun. **75**, 751 – 756 (1977).

[71] C. Olbrich, J. Strümpfer, K. Schulten and U. Kleinekathöfer, *Theory and simulation of the environmental effects on FMO electronic transitions*, J. Phys. Chem. Lett. **2**, 1771–1776 (2011).

[72] A. Ishizaki and G. R. Fleming, *Theoretical examination of quantum coherence in a photosynthetic system at physiological temperature*, Proc. Natl. Acad. Sci. U.S.A. **106**, 17255–17260 (2009).

[73] P. Nalbach and M. Thorwart, *Quantum coherence in photosynthetic exciton dynamics*, in *Journal of Physics: Conference Series*, vol. 376, p. 012025 (IOP Publishing, 2012).

[74] H. Lee, Y.-C. Cheng and G. R. Fleming, *Coherence dynamics in photosynthesis: protein protection of excitonic coherence*, Science **316**, 1462–1465 (2007).

[75] G. S. Schlau-Cohen, A. Ishizaki, T. R. Calhoun, N. S. Ginsberg, M. Ballottari, R. Bassi and G. R. Fleming, *Elucidation of the timescales and origins of quantum electronic coherence in LHCII*, Nat. Chem. **4**, 389–395 (2012).

[76] G. Yu, J. Gao, J. C. Hummelen, F. Wudl and A. J. Heeger, *Polymer photovoltiac cells: Enhanced efficiencies via a network of internal donor-acceptor heterojunctions*, Science **270**, 1789 (1995).

[77] J. Halls, C. Walsh, N. Greenham, E. Marseglia, R. H. Friend, S. C. Moratti and A. B. Holmes, *Efficient photodiodes from interpenetrating polymer networks*, Nature **376**, 498 (1995).

[78] C. Deibel, T. Strobel and V. Dyakonov, *Origin of the efficient polaron-pair dissociation in polymer-fullerene blends*, Phys. Rev. Lett. **103**, 036402 (2009).

[79] A. A. Bakulin, A. Rao, V. G. Pavelyev, P. H. M. van Loosdrecht, M. S. Pshenichnikov, D. Niedzialek, J. Cornil, D. Beljonne and R. H. Friend, *The role of driving energy and delocalized states for charge separation in organic semiconductors*, Science **335**, 1340–1344 (2012).

[80] G. Grancini, M. Maiuri, D. Fazzi, A. Petrozza, H. Egelhaaf, D. Brida, G. Cerullo and G. Lanzani, *Hot exciton dissociation in polymer solar cells*, Nat. Mater. **12**, 29–33 (2013).

[81] A. E. Jailaubekov, A. P. Willard, J. R. Tritsch, W.-L. Chan, N. Sai, R. Gearba, L. G. Kaake, K. J. Williams, K. Leung, P. J. Rossky and X.-Y. Zhu, *Hot charge-transfer excitons set the time limit for charge separation at donor/acceptor interfaces in organic photovoltaics*, Nat. Mater. **12**, 66–73 (2013).

[82] S. Gélinas, A. Rao, A. Kumar, S. L. Smith, A. W. Chin, J. Clark, T. S. van der Poll, G. C. Bazan and R. H. Friend, *Ultrafast long-range charge separation in organic semiconductor photovoltaic diodes*, Science **343**, 512–516 (2014).

[83] M. H. Lee, J. Aragó and A. Troisi, *Charge dynamics in organic photovoltaic materials: interplay between quantum diffusion and quantum relaxation*, J. Phys. Chem. C **119**, 14989–14998 (2015).

[84] V. Abramavicius, V. Pranculis, A. Melianas, O. Inganäs, V. Gulbinas and D. Abramavicius, *Role of coherence and delocalization in photo-induced electron transfer at organic interfaces*, Sci. Rep. **6**, 32914 (2016).

[85] V. Pranculis, Y. Infahsaeng, Z. Tang, A. Devižis, D. A. Vithanage, C. S. Ponseca, O. Inganäs, A. P. Yartsev, V. Gulbinas and V. Sundström, *Charge*

carrier generation and transport in different stoichiometry APFO3:$PC_{61}BM$ solar cells, J. Am. Chem. Soc. **136**, 11331–11338 (2014).

[86] A. Melianas, V. Pranculis, A. Devižis, V. Gulbinas, O. Inganäs and M. Kemerink, *Dispersion-dominated photocurrent in polymer: fullerene solar cells*, Adv. Funct. Mater. **24**, 4507–4514 (2014).

[87] T. Baumgratz, M. Cramer and M. B. Plenio, *Quantifying coherence*, Phys. Rev. Lett. **113**, 140401 (2014).

[88] V. Mihailetchi, J. van Duren, P. Blom, J. Hummelen, R. Janssen, J. Kroon, M. Rispens, W. Verhees and M. Wienk, *Electron transport in a methanofullerene*, Adv. Funct. Mater. **13**, 43–46 (2003).

[89] K. Vandewal, S. Albrecht, E. T. Hoke, K. R. Graham, J. Widmer, J. D. Douglas, M. Schubert, W. R. Mateker, J. T. Bloking, G. F. Burkhard *et al.*, *Efficient charge generation by relaxed charge-transfer states at organic interfaces*, Nat. Mater. **13**, 63–68 (2014).

[90] A. Devižis, A. Serbenta, K. Meerholz, D. Hertel and V. Gulbinas, *Ultrafast dynamics of carrier mobility in a conjugated polymer probed at molecular and microscopic length scales*, Phys. Rev. Lett. **103**, 027404 (2009).

[91] K. Vandewal, Z. Ma, J. Bergqvist, Z. Tang, E. Wang, P. Henriksson, K. Tvingstedt, M. R. Andersson, F. Zhang and O. Inganäs, *Quantification of quantum efficiency and energy losses in low bandgap polymer:fullerene solar cells with high open-circuit voltage*, Adv. Funct. Mater. **22**, 3480–3490 (2012).

[92] A. Devižis, D. Hertel, K. Meerholz, V. Gulbinas and J.-E. Moser, *Time-independent, high electron mobility in thin $PC_{61}BM$ films: relevance to organic photovoltaics*, Org. Electron. **15**, 3729–3734 (2014).

[93] D. A. Vithanage, A. Devižis, V. Abramavičius, Y. Infahsaeng, D. Abramavičius, R. MacKenzie, P. Keivanidis, A. Yartsev, D. Hertel, J. Nelson, V. Sundström and V. Gulbinas, *Visualizing charge separation in bulk heterojunction organic solar cells*, Nat. Comm. **4**, 2334 (2013).

[94] A. J. Barker, K. Chen and J. M. Hodgkiss, *Distance distributions of photogenerated charge pairs in organic photovoltaic cells*, J. Am. Chem. Soc. **136**, 12018–12026 (2014).

[95] H. van Eersel, R. A. Janssen and M. Kemerink, *Mechanism for efficient photoinduced charge separation at disordered organic heterointerfaces*, Adv. Funct. Mater. **22**, 2700–2708 (2012).

[96] D. Murthy, A. Melianas, Z. Tang, G. Juška, K. Arlauskas, F. Zhang, L. D. Siebbeles, O. Inganäs and T. J. Savenije, *Origin of reduced bimolecular recombination in blends of conjugated polymers and fullerenes*, Adv. Funct. Mater. **23**, 4262–4268 (2013).

[97] A. Miller and E. Abrahams, *Impurity conduction at low concentrations*, Phys. Rev. **120**, 745 (1960).

[98] V. Abramavicius, D. Amarasinghe Vithanage, A. Devizis, Y. Infahsaeng, A. Bruno, S. Foster, P. E. Keivanidis, D. Abramavicius, J. Nelson, A. Yartsev, V. Sundstrom and V. Gulbinas, *Carrier motion in as-spun and annealed P3HT:PCBM blends revealed by ultrafast optical electric field probing and Monte Carlo simulations*, Phys. Chem. Chem. Phys. **16**, 2686–2692 (2014).

[99] C. Deibel, T. Strobel and V. Dyakonov, *Origin of the efficient polaron-pair dissociation in polymer-fullerene blends*, Phys. Rev. Lett. **103**, 036402 (2009).

[100] J. Kern, S. Schwab, C. Deibel and V. Dyakonov, *Binding energy of singlet excitons and charge transfer complexes in MDMO-PPV:PCBM solar cells*, Phys. Status Solidi Rapid Res. Lett. **5**, 364–366 (2011).

[101] V. D. Mihailetchi, H. X. Xie, B. de Boer, L. J. A. Koster and P. W. M. Blom, *Charge transport and photocurrent generation in poly(3-hexylthiophene): Methanofullerene bulk-heterojunction solar cells*, Adv. Funct. Mater. **16**, 699–708 (2006).

[102] R. A. Marsh, J. M. Hodgkiss, S. Albert-Seifried and R. H. Friend, *Effect of annealing on P3HT:PCBM charge transfer and nanoscale morphology probed by ultrafast spectroscopy*, Nano Lett. **10**, 923–930 (2010).

[103] J. Huang, G. Li and Y. Yang, *Influence of composition and heat-treatment on the charge transport properties of poly(3-hexylthiophene) and [6,6]-phenyl C_{61}-butyric acid methyl ester blends*, Appl. Phys. Lett. **87**, 112105 (2005).

[104] T. Agostinelli, S. Lilliu, J. G. Labram, M. Campoy-Quiles, M. Hampton, E. Pires, J. Rawle, O. Bikondoa, D. D. C. Bradley, T. D. Anthopoulos, J. Nelson and J. E. Macdonald, *Real-time investigation of crystallization and phase-segregation dynamics in P3HT:PCBM solar cells during thermal annealing*, Adv. Funct. Mater. **21**, 1701–1708 (2011).

[105] C.-Y. Nam, D. Su and C. T. Black, *High-performance air-processed polymer-fullerene bulk heterojunction solar cells*, Adv. Funct. Mater. **19**, 3552–3559 (2009).

[106] E. Verploegen, R. Mondal, C. J. Bettinger, S. Sok, M. F. Toney and Z. Bao, *Effects of thermal annealing upon the morphology of polymer-fullerene blends*, Adv. Funct. Mater. **20**, 3519–3529 (2010).

[107] M. Campoy-Quiles, T. Ferenczi, T. Agostinelli, P. G. Etchegoin, Y. Kim, T. D. Anthopoulos, P. N. Stavrinou, D. D. Bradley and J. Nelson, *Morphology evolution via self-organization and lateral and vertical diffusion in polymer:fullerene solar cell blends*, Nat. Mater. **7**, 158–164 (2008).

[108] A. M. Ballantyne, T. A. M. Ferenczi, M. Campoy-Quiles, T. M. Clarke, A. Maurano, K. H. Wong, W. Zhang, N. Stingelin-Stutzmann, J.-S. Kim, D. D. C. Bradley, J. R. Durrant, I. McCulloch, M. Heeney, J. Nelson, S. Tierney, W. Duffy, C. Mueller and P. Smith, *Understanding the influence of morphology on poly(3-hexylselenothiophene):PCBM solar cells*, Macromolecules **43**, 1169–1174 (2010).

[109] C. H. Woo, B. C. Thompson, B. J. Kim, M. F. Toney and J. M. J. Fréchet, *The influence of poly(3-hexylthiophene) regioregularity on fullerene-composite solar cell performance*, J. Am. Chem. Soc. **130**, 16324–16329 (2008).

[110] X. Yang, J. Loos, S. C. Veenstra, W. J. H. Verhees, M. M. Wienk, J. M. Kroon, M. A. J. Michels and R. A. J. Janssen, *Nanoscale morphology of high-performance polymer solar cells*, Nano Lett. **5**, 579–583 (2005).

[111] D. Veldman, Ö. Ipek, S. C. J. Meskers, J. Sweelssen, M. M. Koetse, S. C. Veenstra, J. M. Kroon, S. S. van Bavel, J. Loos and R. A. J. Janssen, *Compositional and electric field dependence of the dissociation of charge transfer excitons in alternating polyfluorene copolymer/fullerene blends*, J. Am. Chem. Soc. **130**, 7721–7735 (2008).

[112] P. E. Keivanidis, T. M. Clarke, S. Lilliu, T. Agostinelli, J. E. Macdonald, J. R. Durrant, D. D. C. Bradley and J. Nelson, *Dependence of charge separation efficiency on film microstructure in poly(3-hexylthiophene-2,5-diyl):[6,6]-phenyl-C_{61} butyric acid methyl ester blend films*, J. Phys. Chem. Lett. **1**, 734–738 (2010).

[113] R. Hamilton, C. G. Shuttle, B. O'Regan, T. C. Hammant, J. Nelson and J. R. Durrant, *Recombination in annealed and nonannealed polythiophene/fullerene solar cells: transient photovoltage studies versus numerical modeling*, J. Phys. Chem. Lett. **1**, 1432–1436 (2010).

[114] T. G. J. van der Hofstad, D. Di Nuzzo, M. van den Berg, R. A. J. Janssen and S. C. J. Meskers, *Influence of photon excess energy on charge carrier dynamics in a polymer-fullerene solar cell*, Adv. Energy Mater. **2**, 1095–1099 (2012).

[115] C. Müller, T. A. M. Ferenczi, M. Campoy-Quiles, J. M. Frost, D. D. C. Bradley, P. Smith, N. Stingelin-Stutzmann and J. Nelson, *Binary organic photovoltaic blends: a simple rationale for optimum compositions*, Adv. Mater. **20**, 3510–3515 (2008).

[116] W. Ma, C. Yang and A. J. Heeger, *Spatial Fourier-transform analysis of the morphology of bulk heterojunction materials used in "plastic" solar cells*, Adv. Mater. **19**, 1387–1390 (2007).

[117] T. J. Savenije, J. E. Kroeze, M. M. Wienk, J. M. Kroon and J. M. Warman, *Mobility and decay kinetics of charge carriers in photoexcited PCBM/PPV blends*, Phys. Rev. B **69**, 155205 (2004).

[118] J. Cabanillas-Gonzalez, T. Virgili, A. Gambetta, G. Lanzani, T. D. Anthopoulos and D. M. de Leeuw, *Photoinduced transient Stark spectroscopy in organic semiconductors: a method for charge mobility determination in the picosecond regime*, Phys. Rev. Lett. **96**, 106601 (2006).

[119] D. Veldman, Ö. Ipek, S. C. J. Meskers, J. Sweelssen, M. M. Koetse, S. C. Veenstra, J. M. Kroon, S. S. van Bavel, J. Loos and R. A. J. Janssen, *Compositional and electric field dependence of the dissociation of charge transfer excitons in alternating polyfluorene copolymer/fullerene blends*, J. Am. Chem. Soc. **130**, 7721–7735 (2008).

[120] I. A. Howard, R. Mauer, M. Meister and F. Laquai, *Effect of morphology on ultrafast free carrier generation in polythiophene:fullerene organic solar cells*, J. Am. Chem. Soc. **132**, 14866–14876 (2010).

Appendix A

Coherent states

The coherent state $\big|\alpha\big\rangle$ is defined as the eigenvector of the annihilation operator $\widehat{a}$:

$$\widehat{a}\big|\alpha\big\rangle = \alpha\big|\alpha\big\rangle. \tag{A.1}$$

The annihilation operator is not Hermitian, thus the quantity α in Eq. (A.1) is a complex number and can acquire any value. The representation of the coherent state $\big|\alpha\big\rangle$ in the occupation number basis of the harmonic oscillator $\big|n\big\rangle$ can be obtained by calculating the scalar product of both sides of Eq. (A.1) with the vector $\big\langle n\big|$ which yields

$$\big|\alpha\big\rangle = K\sum_{n=0}^{\infty}\frac{\alpha^n}{\sqrt{n!}}\big|n\big\rangle. \tag{A.2}$$

Choosing K to be equal to 1, we can calculate using Eq. (A.2) the scalar product of two coherent states $\big\langle\alpha\big|$ and $\big|\beta\big\rangle$:

$$\big\langle\alpha\big|\beta\big\rangle = \mathrm{e}^{\alpha^*\beta}. \tag{A.3}$$

From Eq. (A.3), we can see that the coherent states $\big|\alpha\big\rangle$ are not normalized because $\big\langle\alpha\big|\alpha\big\rangle = \mathrm{e}^{\alpha^*\alpha} \neq 1$. Despite the fact that the coherent states $\big|\alpha\big\rangle$ being the eigenvectors of a non-Hermitian operator $\widehat{a}$ are not orthogonal, they still can be used to construct the identity operator

$$\widehat{I} = \int_{-\infty}^{\infty}\mathrm{d}^2\alpha\mathrm{e}^{-\alpha^*\alpha}\big|\alpha\big\rangle\big\langle\alpha\big|, \tag{A.4}$$

where $\mathrm{d}^2\alpha \equiv \frac{\mathrm{dRe}[\alpha]\mathrm{dIm}[\alpha]}{\pi}$ and the factor $\mathrm{e}^{-\alpha^*\alpha}$ ensures the proper normalization [34].

Another useful property of the coherent states can be obtained by noticing that the vector $\big\langle\alpha\big|\widehat{a}$ can be written as $\frac{\partial}{\partial\alpha^*}\big\langle\alpha\big|$:

$$\langle\alpha|\widehat{a} = \sum_{n=0}^{\infty} \frac{(n+1)\,\alpha^{*n}}{\sqrt{(n+1)!}} \langle n+1| = \sum_{n=0}^{\infty} \frac{\alpha^{*n}}{\sqrt{n!}} \langle n|\widehat{a} = \frac{\partial}{\partial \alpha^*} \langle\alpha|. \tag{A.5}$$

Using this property, we obtained the effective Hamiltonian expression in Eq. (2.46).

Appendix B

Coherent state path integrals

Derivation of general coherent state path integral

Let us consider a bosonic system described by the Hamiltonian $\widehat{H}\left(\widehat{a}^{\dagger},\widehat{a}\right)$ expressed in the second quantization form with normal-ordered creation and annihilation operators. The dynamics of such system is determined by the evolution operator $\widehat{U}\left(t\right)=\exp\left(-\mathrm{i}\widehat{H}\left(\widehat{a}^{\dagger},\widehat{a}\right)t\right)$. The probability to reach some final coherent state $\left|\alpha_f\right\rangle$ at time t starting with an initial state $\left|\alpha_i\right\rangle$ at time 0 is given by the modulus squared of the transition amplitude, also called the propagator, $K\left(\alpha_f^*,\alpha_i;t\right)=\left\langle\alpha_f\right|\widehat{U}\left(t\right)\left|\alpha_i\right\rangle$. This matrix element cannot be evaluated exactly for a finite time interval, however for an infinitesimal time ϵ we can expand the evolution operator $\widehat{U}\left(\epsilon\right)$ leaving only the linear term:

$$\widehat{U}\left(\epsilon\right)\approx\widehat{I}-\mathrm{i}\epsilon\widehat{H}\left(\widehat{a}^{\dagger},\widehat{a}\right). \tag{B.1}$$

Substituting this expression in the definition of the transition amplitude we obtain

$$\begin{aligned}K\left(\alpha_f^*,\alpha_i;\epsilon\right)=\left\langle\alpha_f\right|\left(\widehat{I}-\mathrm{i}\epsilon\widehat{H}\left(\widehat{a}^{\dagger},\widehat{a}\right)\right)\left|\alpha_i\right\rangle&=\mathrm{e}^{\alpha_f^*\alpha_i}\left(1-\mathrm{i}\epsilon H\left(\alpha_f^*,\alpha_i\right)\right)\\&\approx\mathrm{e}^{\alpha_f^*\alpha_i-\mathrm{i}\epsilon H\left(\alpha_f^*,\alpha_i\right)}.\end{aligned} \tag{B.2}$$

Here we used the formula for calculating the matrix element of a normal-ordered operator between coherent states [34]. In order to use the result (B.2) in case of finite t we divide this interval into $M\to\infty$ segments of size $\epsilon=t/M$ and the propagator is given by

$$K\left(\alpha_f^*,\alpha_i;t\right)=\lim_{M\to\infty}\left\langle\alpha_f\right|\prod_{k=1}^{M}\mathrm{e}^{-\mathrm{i}\epsilon\widehat{H}\left(\widehat{a}^{\dagger},\widehat{a}\right)}\left|\alpha_i\right\rangle. \tag{B.3}$$

We now insert the resolution of unity in the coherent state basis (A.4) at every time step k in Eq. (B.3) and obtain

$$K\left(\alpha_f^*,\alpha_i;t\right)=\lim_{M\to\infty}\int_{-\infty}^{\infty}\prod_{k=1}^{M-1}\mathrm{d}^2\alpha_k \mathrm{e}^{-\sum_{k=1}^{M-1}\alpha_k^*\alpha_k}\mathrm{e}^{\sum_{k=1}^{M}\left(\alpha_k^*\alpha_{k-1}-\mathrm{i}\epsilon H(\alpha_k^*,\alpha_{k-1})\right)}, \tag{B.4}$$

where we have for the endpoints $\alpha_M^*=\alpha_f^*$ and $\alpha_0=\alpha_i$.

In the limit when $M\to\infty$ the exponent in expression (B.4) can be cast into

$$\begin{aligned}&\alpha_M^*\alpha_{M-1}-\mathrm{i}\epsilon H\left(\alpha_M^*,\alpha_{M-1}\right)+\mathrm{i}\epsilon\sum_{k=1}^{M-1}\left(\mathrm{i}\alpha_k^*\frac{\alpha_k-\alpha_{k-1}}{\epsilon}-H\left(\alpha_k^*,\alpha_{k-1}\right)\right)\\ &\qquad\to\alpha^*\left(t\right)\alpha\left(t\right)+\mathrm{i}\int_0^t\mathrm{d}\tau\left(\mathrm{i}\alpha^*\left(\tau\right)\frac{\partial\alpha\left(\tau\right)}{\partial\tau}-H\left(\alpha^*\left(\tau\right),\alpha\left(\tau\right)\right)\right).\end{aligned} \tag{B.5}$$

With Eq. (B.5) the propagator $K\left(\alpha_f^*,\alpha_i;t\right)$ obtains its final form:

$$\begin{aligned}K\left(\alpha_f^*,\alpha_i;t\right)&=\int_{\alpha_i}^{\alpha_f^*}\mathcal{D}\left[\alpha^*\left(\tau\right),\alpha\left(\tau\right)\right]\mathrm{e}^{\alpha^*(t)\alpha(t)+\mathrm{i}\int_0^t\mathrm{d}\tau\left(\mathrm{i}\alpha^*(\tau)\frac{\partial\alpha(\tau)}{\partial\tau}-H(\alpha^*(\tau),\alpha(\tau))\right)}\\ &=\int_{\alpha_i}^{\alpha_f^*}\mathcal{D}\left[\alpha^*\left(\tau\right),\alpha\left(\tau\right)\right]\mathrm{e}^{\mathrm{i}S(\alpha^*,\alpha;t)}.\end{aligned} \tag{B.6}$$

Here $\mathcal{D}\left[\alpha^*\left(\tau\right),\alpha\left(\tau\right)\right]=\lim_{M\to\infty}\int_{-\infty}^{\infty}\prod_{k=1}^{M-1}\mathrm{d}^2\alpha_k$ is the measure of the functional integral and $S\left(\alpha^*,\alpha;t\right)$ is the action.

Equivalence of the coherent state path integral to Schrödinger equation

Propagator $K\left(\alpha_f^*,\alpha_i;t\right)$ describes the evolution of the system from the initial to the final state, thus from its path integral representation (B.6) we must be able to recover the Schrödinger equation. For this we first obtain the expression for the difference $K\left(\alpha_f^*,\alpha_i;t+\epsilon\right)-K\left(\alpha_f^*,\alpha_i;t\right)$ where ϵ is an infinitesimal time step:

$$K\left(\alpha_f^*,\alpha_i;t+\epsilon\right)-K\left(\alpha_f^*,\alpha_i;t\right)=\int\limits_{\alpha_i}^{\alpha_f^*}\mathcal{D}\left[\alpha^*\left(\tau\right),\alpha\left(\tau\right)\right]$$
$$\times\,\mathrm{e}^{\alpha^*(t)\alpha(t)+\mathrm{i}\int\limits_0^t\mathrm{d}\tau\left(\mathrm{i}\alpha^*(\tau)\frac{\partial\alpha(\tau)}{\partial\tau}-H(\alpha^*(\tau),\alpha(\tau))\right)}$$
$$\times\left(\mathrm{e}^{\alpha^*(t+\epsilon)\alpha(t+\epsilon)-\alpha^*(t)\alpha(t)+\mathrm{i}\epsilon\left(\mathrm{i}\alpha^*(t)\frac{\partial\alpha(t)}{\partial t}-H(\alpha^*(t),\alpha(t))\right)}-1\right). \qquad \text{(B.7)}$$

The expression in the exponent of the third line can be further simplified turning back to the discrete representation of the action (B.4), hence $\alpha^*\left(t+\epsilon\right)\alpha\left(t+\epsilon\right)\to\alpha_f^*\alpha_M$ and $\alpha^*\left(t\right)\alpha\left(t\right)\to\alpha_f^*\alpha_{M-1}$. With these substitutions we have

$$\mathrm{i}S\left(\alpha^*,\alpha;t+\epsilon\right)-\mathrm{i}S\left(\alpha^*,\alpha;t\right)=\alpha_f^*\left(\alpha_M-\alpha_{M-1}\right)-\alpha_M^*\left(\alpha_M-\alpha_{M-1}\right)$$
$$-\mathrm{i}\epsilon H\left(\alpha_M^*,\alpha_{M-1}\right). \qquad \text{(B.8)}$$

When the number of discretization intervals M goes to infinity α_M^* approaches α_f^* and the two terms on the right-hand side of the first line in Eq. (B.8) cancel each other. Thus, the propagator difference obtains the following form:

$$K\left(\alpha_f^*,\alpha_i;t+\epsilon\right)-K\left(\alpha_f^*,\alpha_i;t\right)=\int\limits_{\alpha_i}^{\alpha_f^*}\mathcal{D}\left[\alpha^*\left(\tau\right),\alpha\left(\tau\right)\right]\left(\mathrm{e}^{\mathrm{i}S(\alpha^*,\alpha;t+\epsilon)}-\mathrm{e}^{\mathrm{i}S(\alpha^*,\alpha;t)}\right)$$
$$=-\mathrm{i}\epsilon\int\limits_{\alpha_i}^{\alpha_f^*}\mathcal{D}\left[\alpha^*\left(\tau\right),\alpha\left(\tau\right)\right]H\left(\alpha^*\left(\tau\right),\alpha\left(\tau\right)\right)\mathrm{e}^{\mathrm{i}S(\alpha^*,\alpha;t)}. \qquad \text{(B.9)}$$

Here we expanded the exponent $\exp\left(-\mathrm{i}\Delta tH\left(\alpha_M^*,\alpha_{M-1}\right)\right)\approx 1-\mathrm{i}\Delta tH\left(\alpha_M^*,\alpha_{M-1}\right)$ and inserted this result into Eq. (B.7) also reverting to continuous notation $H\left(\alpha_M^*,\alpha_{M-1}\right)\to H\left(\alpha^*\left(t\right),\alpha\left(t-\epsilon\right)\right)$. Denoting $\mathrm{e}^{\mathrm{i}S(\alpha^*,\alpha;t)}\equiv\psi\left(\alpha^*,\alpha;t\right)$ and dividing both sides of Eq. (B.9) by $\epsilon\to 0$ we obtain the Schrödinger equation for the function $\psi\left(\alpha^*,\alpha;t\right)$:

$$\frac{\mathrm{d}}{\mathrm{d}t}\psi\left(\alpha^*,\alpha;t\right)=-\mathrm{i}H\left(\alpha^*\left(t\right),\alpha\left(t-\epsilon\right)\right)\psi\left(\alpha^*,\alpha;t\right). \qquad \text{(B.10)}$$

Following Ref. [37] substitutions $\psi\left(\alpha^*,\alpha;t\right)\to\left|\psi\left(t\right)\right\rangle$ and $H\left(\alpha^*\left(t\right),\alpha\left(t-\epsilon\right)\right)\to\widehat{H}$ allow us to recover the usual Schrödinger equation for the system wave vector.

Acknowledgments

First of all, I would to thank my supervisor, prof. Darius Abramavičius, for guiding me through the bumpy terrain of theoretical physics and my informal supervisor, prof. Vidmantas Gulbinas, for showing me how important it is to understand the physical meaning behind all the mathematical equations.

I am also grateful to my colleagues from the Department of Theoretical Physics, especially Andrius Gelžinis, Vladimir Chorošajev, Vytautas Butkus, Jevgenij Chmeliov, Stepas Toliautas, Vytautas Balevičius Jr. and Olga Rancova, for providing invaluable support during doctoral studies in various forms ranging from scientific discussions to basketball and politically incorrect jokes.

Many of the calculations in this thesis would have not been performed without the resources of the High Performance Computing Center "HPC Saulėtekis" at Faculty of Physics, Vilnius University.

I would like to thank Michael Thorwart and Stephan Weiss for enabling me to look at my research from a different perspective.

I also sincerely thank my family for encouragement when it was needed mostly.

Finally, special thanks to Gerda Blantaitytė for being so patient with me and not kicking me from home while I was being irresponsive writing this thesis.